A measurement of the hadronic production of J/Ψ's

A. Simard

Physics Department

McGill University, Montreal

March, 1990

A thesis submitted to the Faculty of Graduate Studies and Research
in partial fulfillment of the degree of
Master of Science

Abstract

The production of charmonium states J/Ψ and Ψ' was measured at 300 GeV/c with $\pi^{\pm}$, p, and $\bar{p}$ beams on a lithium target. The cross sections were determined by analyzing a fraction (10%) of the data recorded by the experiment E705 at Fermilab. The data acquisition took place at the High Intensity Laboratory located on the "Proton West" beam line, and extended over a period of nine month during 1987-1988.

The efficiencies for the different detector components of the E705 spectrometer were measured, and the global acceptance was determined. The measured absolute cross sections for J/Ψ and Ψ' are consistent with the measurements obtained in other experiments. The differential cross section for J/Ψ production was measured for the kinematical variables X_f, P_t, and for the J/Ψ decay angles. The distributions obtained are compared with the distributions measured at other energies by previous experiments.

Sommaire

La production des états charmonium J/Ψ et Ψ' a été mesurée au moyen d'un faisceau de $\pi^{\pm}$, p, et $\bar{p}$ incident à 300 GeV/c sur une cible de lithium. Les sections efficaces ont été déterminées par l'analyse d'une portion (10%) des événements enregistrés par l'expérience E705 au Fermilab. L'acquisition des données a été effectuée au laboratoire à haute intensité desservi par la ligne de faisceau "proton west", et s'est étendue sur une période de neuf mois au cours des années 1987-1988.

Les efficacités pour les diverses composantes du montage expérimental ont été mesurées, et l'acceptance globale a été déterminée. Les sections efficaces absolues pour les états J/Ψ et Ψ' sont en bon accord avec les valeurs obtenues par d'autres expériences. Les sections efficaces différentielles pour la production de l'état J/Ψ ont été mesurées pour les variables cinématiques X_f, P_t, et les angles de la désintegration de l'état J/Ψ. Les distributions obtenues sont comparées avec les distributions mesurées à des énergies différentes dans des expériences antérieures.

Original material

The analysis for the present work was performed using the data from experiment E705, which offered a high statistic event sample to study the charmonium production by $\pi^{\pm}$, p and $\bar{p}$ beam at 300 GeV/c. My principal contributions to the accomplishment of the experiment were:

1) Development, in cooperation with Lon Turnbull, of a di-μ filter program used in the offline analysis;

2) Participation in optimizing the di-μ reconstruction program;

3) Determination of the reconstruction efficiency of the di-μ program in cooperation with Spyros Tzamarias;

4) Determination of the efficiencies of the scintillation counters, proportional chambers and drift chambers.

5) Participation in implementing and running the reconstruction programs on a system of parallel processor (ACP).

6) Determination of the absolute cross section for the J/Ψ and Ψ' states, and determination of the kinematical distributions for the J/Ψ production.

7) Participation in the data acquisition and event monitoring.

Acknowledgments

The realization of a high energy experiment involves the direct or indirect participation of many people. The help given by all the members of the E705 collaboration has been essential for the accomplishment of the present work. I want to thank the professors, scientist and students from McGill University for their precious advices and encouragements, and I especially want to thank my supervisor, Sergio Conetti, for his continuous assistance, and his careful and numerous readings of this thesis.

Essential contributions were provided by the personnel in Fermilab as the crew chiefs, the Computer Department consultants, the librarians, the computer operators, the accelerator operators, and the people involved in the technical support for this experiment. Generous help was also provided by the supporting personnel of McGill University, which facilitated many times the various steps leading to the present work.

Contents

Figures

Tables

CHAPTER 1

Introduction

The study of the bound state comprised of a charm quark and its antiparticle, called charmonium, has been the subject of many experiments since the first signal was observed in 1974. The experiment E705, located in the High Intensity Laboratory at Fermilab, offered a high statistics data sample to study the charmonium production by hadronic interactions. The S (J/Ψ and Ψ') and P (χ) states were produced by inelastic collisions using a 300 GeV/c hadron beam ($\pi^{\pm}$, p and $\overline{p}$) incident on a lithium target. The J/Ψ and Ψ' states were observed through their decay into a pair of muons, while the χ states may be reconstructed by looking at the electromagnetic decay $\chi \rightarrow J/\Psi + \gamma$. In parallel to the charmonium measurement, the experiment E705 will also be able to study direct photon production.

1.1 The quark model

What are the smallest constituents of matter, and how those constituents interact with each other, is a fundamental question in physics. In 1932, the discovery of the neutron by Chadwick(1)(2) brought the number of elementary particles to three: the proton, the neutron and the electron. However, the development of experimental physics, by means of more and more energetic accelerators, permitted the discovery of a large number of new particles. As the number of known particles increased (more than a hundred had been observed by 1960), the model describing those particles as being the ultimate constituents of matter lacked the elegance of a simple model made of a few particles.

At that time, the particles were classified into two categories, the leptons and the hadrons, the first category differing from the second by the small number of particles belonging to it, their relatively low masses, and their tendency to interact at a lower rate. In 1964, Gell-Mann(3) and Zweig(4) proposed a model consisting of three quarks (u, d and s) that could explain the existence of all known hadrons. The four known leptons (e^-, μ^-, ν_e and ν_μ) with their four corresponding antiparticles (e^+, μ^+, $\bar{\nu}_e$, $\bar{\nu}_\mu$), being apparently structureless and in a reasonably small number, were still considered as elementary particles. A decade later, the Gell-Mann and Zweig model was enriched by the discovery of heavier quarks (c and b), and by the observation of a new lepton, the τ.

Today's theories describing the interactions between the elementary particles (the quarks and the leptons) are the Quantum Chromo-Dynamics(QCD) and the Electroweak Theory, the two theories forming together what is known as the Standard Model. In both theories, the interaction between the particles is described by the exchange of force mediators called gauge bosons. The Electroweak theory describes the interactions between the particles as the result of an exchange of photons, $W^{\pm}$, or Z^0. The QCD interactions are mediated by the strong field carriers, the gluons. Contrary to the case of the photon in the electro-magnetic interactions, the gluons are carriers of the strong charge, the color, which allows them to interact with each other. The list of elementary particles described in the Standard Model, along with the gauge bosons, is shown in table 1.

Table 1.1: Today's elementary particles and gauge bosons

Quarks			
	u (up)	c (charm)	t (top)*
	d (down)	s (strange)	b (beauty)
Leptons			
	e (electron)	μ (muon)	τ (tau)
	ν_e (e neutrino)	ν_μ (μ-neutrino)	ν_τ (τ-neutrino)*
Gauge bosons			
	γ (photon)	$W^{\pm}$, Z (weak bosons)	g_i (i=1,...,8 gluons)

*Though predicted by the Standard Model, the top quark and the τ-neutrino are not yet observed experimentally.

1.2 Observation of charmonium states

The first signal for the existence of a charmed quark came from two experiments almost simultaneously in November 1974. The first experiment, using a 30 GeV/c proton beam extracted from the Alternating-Gradient Synchrotron at the Brookhaven National Laboratory(5), observed a sharp resonance at 3.1 GeV/c^2 in the di-electron invariant mass spectrum for the reaction $p + Be \rightarrow e^+ + e^- + x$. The other experiment, using the $e^+ e^-$ storage ring SPEAR at Stanford Linear Accelerator Center (SLAC)(6), also observed a resonance at 3.1 GeV/c^2 for the reactions:

$$\begin{aligned} e^+ e^- &\rightarrow \mu^+ \mu^- \\ &\rightarrow e^+ e^- \\ &\rightarrow \text{hadrons.} \end{aligned}$$

The results of the two experiments are shown in figure 1.1 . The new resonance, called J by the Brookhaven experiment and Ψ by the SLAC group, is now usually referred to as J/Ψ.

Figure 1.1: First J/Ψ signals. a) Di-μ spectrum obtained at the Brookhaven National Laboratory. b) Di-hadron, di-μ and di-electron spectra obtained at the Stanford Linear Accelerator Center (SLAC).

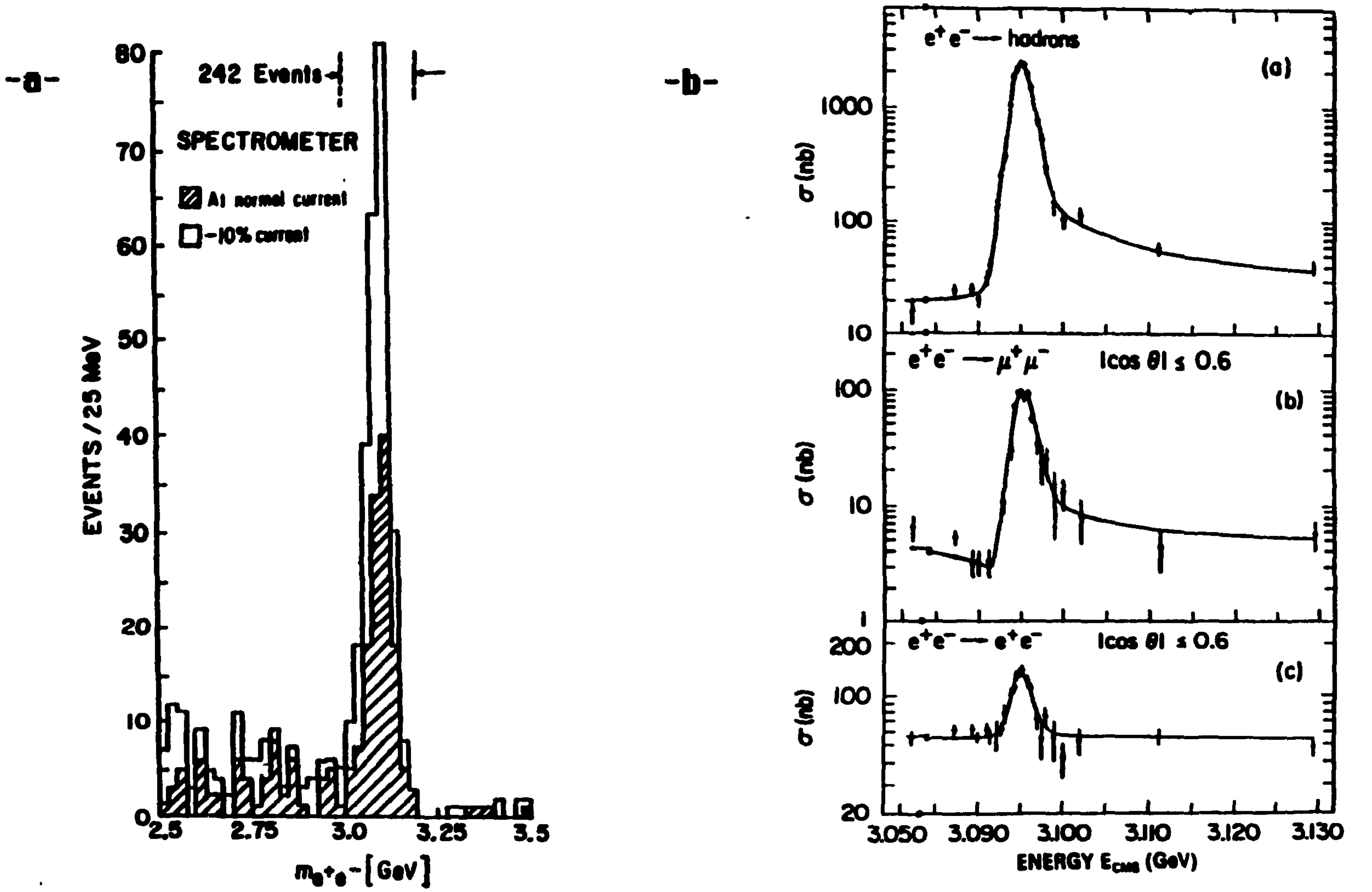

No model of a bound state involving the three quarks of the Gell-Mann and Zweig theory (u, d and s) seemed suitable to explain the presence of the new resonance. The Drell-Yan process, by which two leptons are created from the annihilation of a pair of quark-antiquark into a virtual photon, was insufficient to explain the large production rate of the J/Ψ. Soon, it seemed that the likeliest solution to describe the new resonance was by a bound state between a new quark and its antiparticle. The hypothesis of the existence of a fourth quark characterized by a new quantum number (the charm) had been already proposed in the GIM mechanism(7) in 1970, in order to explain the absence of strangeness changing in weak neutral currents. The name of charmonium was given to the charm-anticharm quark system. On the basis of experimental results, the quantum numbers assigned to the J/Ψ were $N^{2s+1}L_J = 1^3S_1$ and $J^{PC} = 1^{--}$.

The natural consequence of interpreting the J/Ψ as a charmonium state was the prediction of the existence of other members of the charmonium family. Even before the charmonium interpretation took hold, the first radially excited state (N=2), the Ψ', was observed at SPEAR at 3.67 GeV/c^2 a few days after the discovery of the J/Ψ. The charmonium interpretation was finally confirmed by the observation of the states $^3P_0$, $^3P_1$, $^3P_2$ (also called χ_0, χ_1 and χ_2) at DASP (DESY)(8) and MARK 1 (SPEAR)(9) and, later on, by the observation of the $N^{2s+1}L_{J=1}$ $^1S_0$ (η_c) and 2^1S_0 (η_c') states at the SPEAR Crystal-Ball experiment (10) in 1979. The spectrum of today's observed charmonium states is shown in figure 1.2; also shown on this figure are the J^{PC} quantum numbers associated with every state, and the electro-magnetic transitions between different states.

Some of the low order graphs for the J/Ψ decay are shown on figure 1.3. 1.3-a is forbidden by conservation of energy since the charm quark is heavier than the

Figure 1.2: Mass spectrum of the observed charmonium states with the corresponding quantum numbers The horizontal dashed line is the threshold over which a charmonium states can decay into two charmed states ($\bar{D} = \bar{c}q$ and $D = c\bar{q}$). The electromagnetic transitions between different states are indicated by smooth lines (dipolar electric) or dashed lines (dipolar magnetic). Each state is aligned with its corresponding quantum numbers in the bottom of the figure.

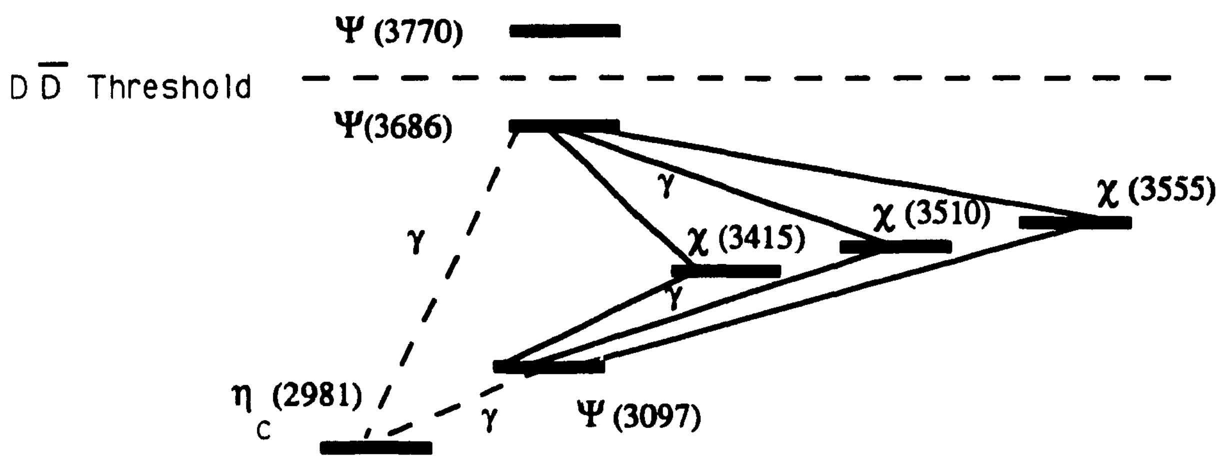

J^{PC}	0^{-+}	1^{--}	0^{++}	1^{++}	2^{++}
$^{2S+1}L_J$	$^1S_0$	$^3S_1$	$^3P_0$	$^3P_1$	$^3P_2$

Figure 1.3: Low order graph for J/Ψ decay The process shown in a) is forbidden by energy conservation, the process b) is the electromagnetic decay, and the process c) is the decay into a pair of mesons involving three gluons in the intermediate state.

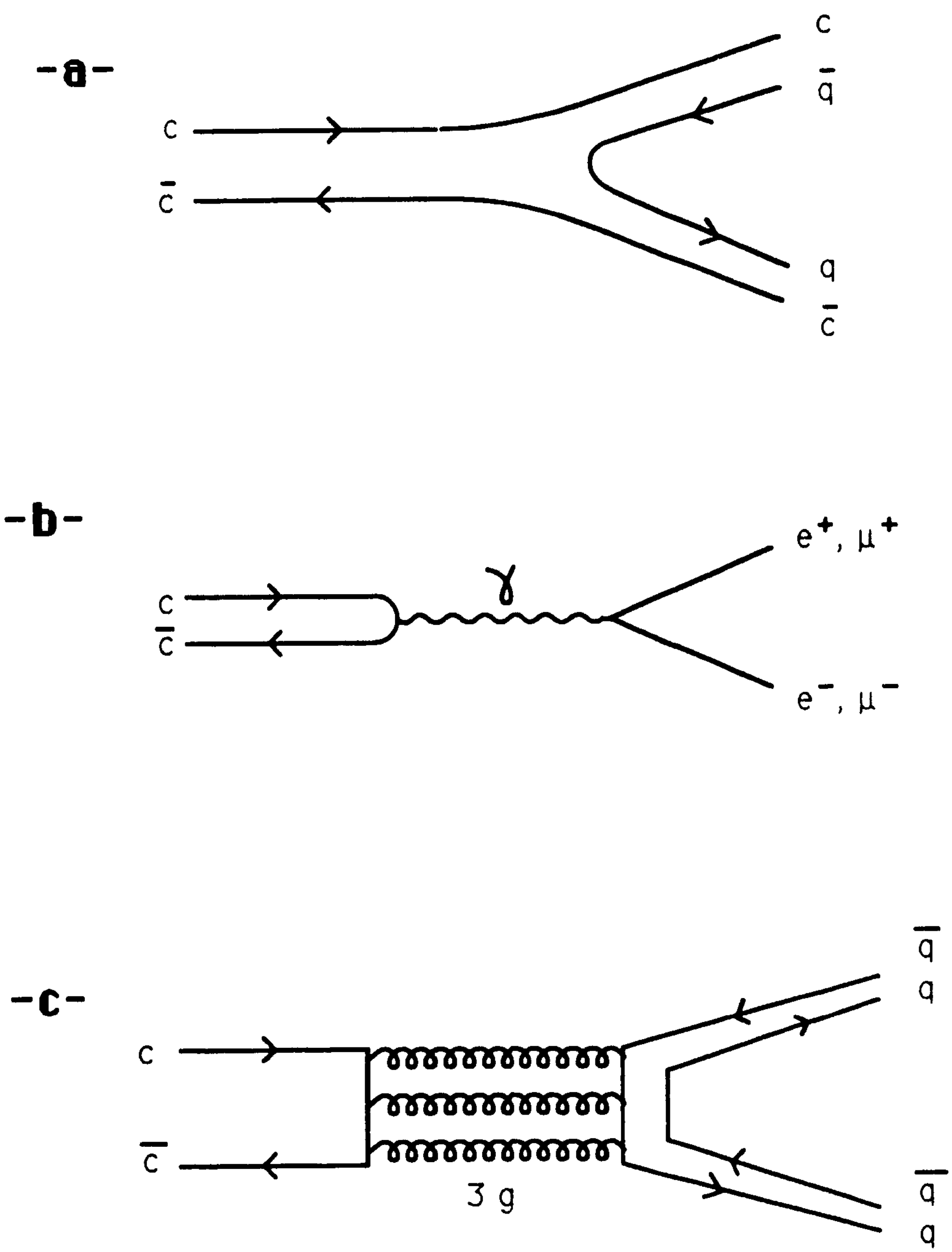

half of the mass of the J/Ψ. 1.3-b is the electromagnetic decay, where the final state is made of a $\mu^+\mu^-$ or e^+e^- pair. The graph on figure 1.3-c shows the hadronic decay. The minimum number of gluons involved in this last process must be at least three because of color conservation, and the conservation of the charge conjugation number C which is -1 for the J/Ψ as well as for the gluon.

1.3 J/Ψ, Ψ' hadronic production

The subject of the present work is a measurement of the cross section of the charmonium S states (J/Ψ, Ψ') in hadronic production. The results were obtained by analyzing a fraction (10%) of the E705 data. The following section reviews the previous experiment in charmonium hadronic production, to which the results of the present work will be compared.

• The Ω experiment

The experiment Ω(11) was a high mass di-μ pair experiment made at CERN between 1977 and 1981. The cross sections for J/Ψ and Ψ' production were measured at 39.5 GeV/c using an unseparated $\pi^{\pm}$, $K^{\pm}$, and $p^{\pm}$ beam incident on a liquid hydrogen target followed by a tungsten target (see apparatus and mass spectrum on figure 1.4-a).

• The CP and CIP experiments

An experiment made by a collaboration between the University of Chicago and Princeton University (19) (referred to as the CP experiment) was realized at the Chicago cyclotron magnet spectrometer in the muon laboratory at Fermilab (see figure 1.4-b). This experiment measured J/Ψ and Ψ' production by $\pi^{\pm}$, and p beams at 225

Figure 1.4-a: Experimental setup and di-μ mass spectrum from different beams from the experiment Ω.

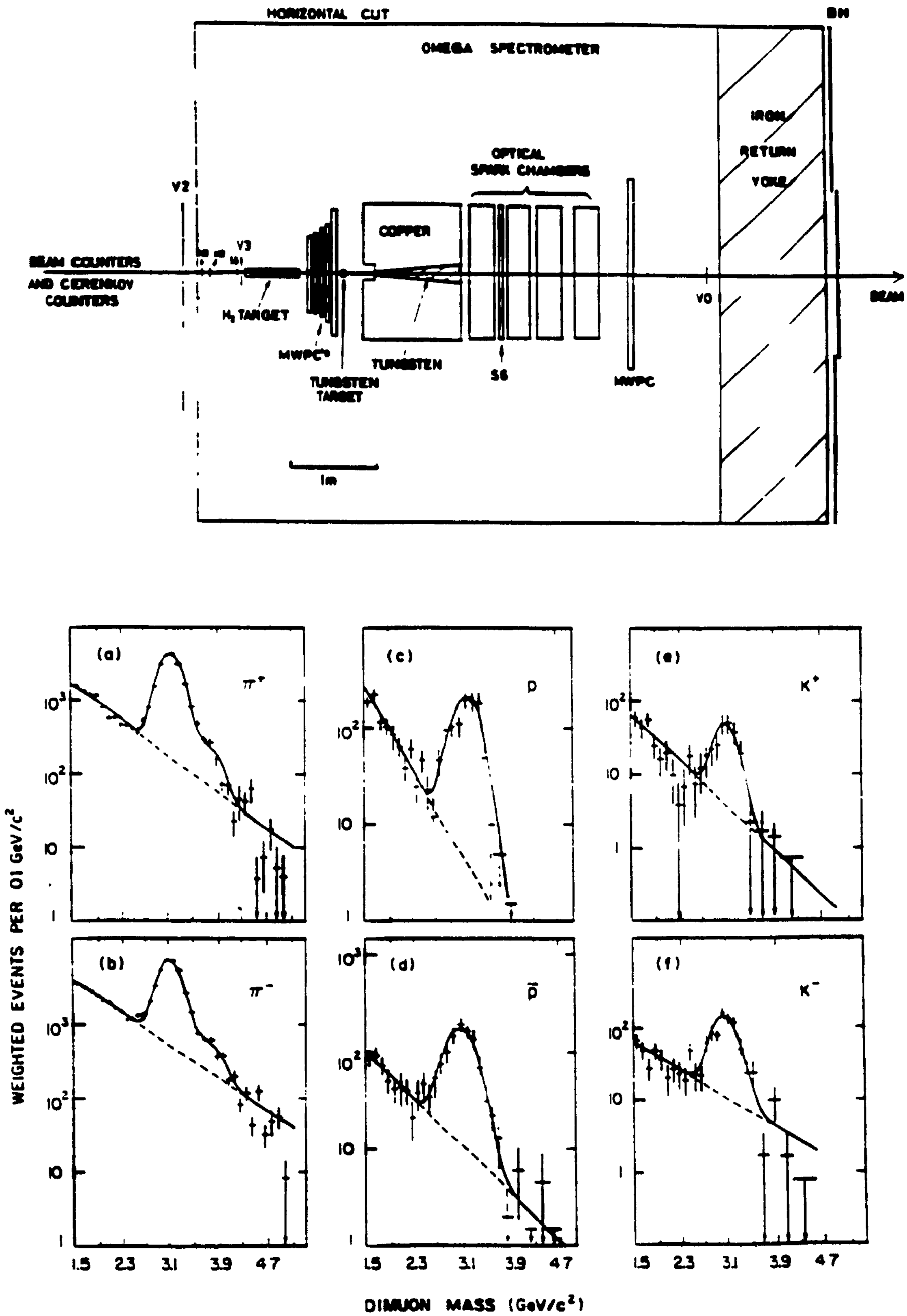

Figure 1.4-b: Experimental setup and di-μ mass spectrum from different beams from the CIP experiment.

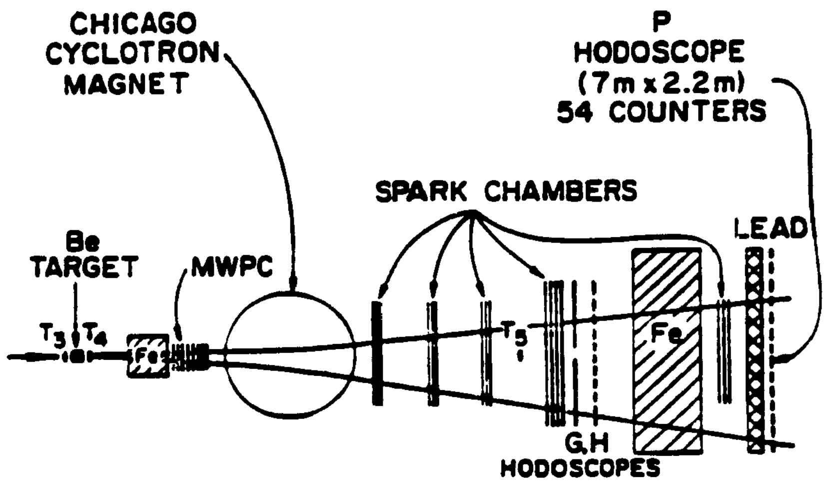

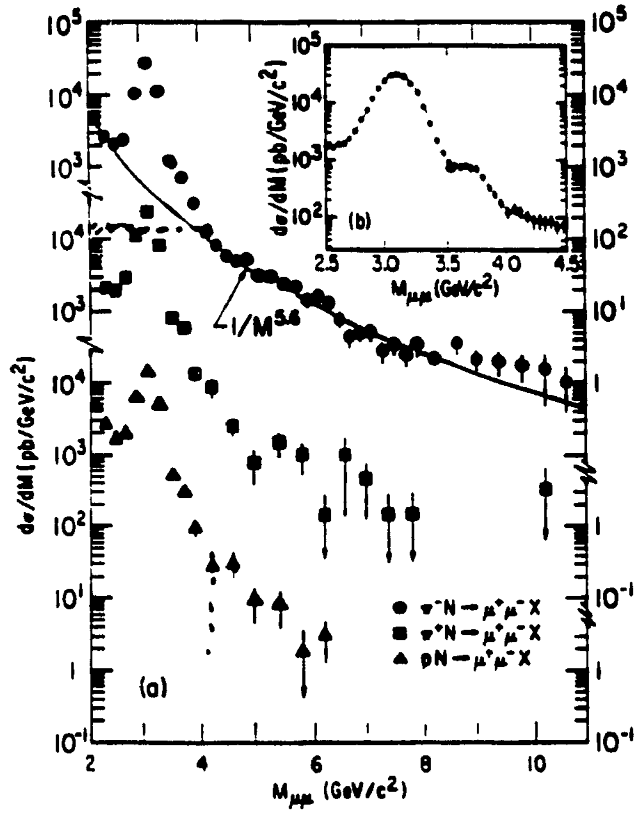

GeV/c on C, Cu and W targets. The experimental setup for those experiments is shown in figure 1.4-b, together with the di-μ invariant mass spectrum obtained by the CIP group.

• Experiment E537

The experiment E537 (13) (figure 1.4-c) was made in the High Intensity Laboratory at Fermilab. The J/Ψ and Ψ' production was measured using π^- and $\bar{p}$ incident at 125 GeV/c on Be, Cu and W targets.

• Experiment NA3

The experiment NA3 (14) (figure 1.4-d) was a high statistics experiment measuring the J/Ψ production by $\pi^{\pm}$, $K^{\pm}$, and $p^{\pm}$ on different targets (H_2 and Pt) at different energies (150,200 and 280 GeV/c). Among the most interesting results obtained by this experiment were the determination of the nuclear mass dependance of the J/Ψ cross section for different kinematical regions, and a measurement of the angular distribution of the muons in the decay $J/\Psi \rightarrow \mu^+\mu^-$.

• Experiment WA11

The CERN experiment WA11 (20), using a 150 GeV/c π^- beam on Be target, measured the cross section of the J/Ψ and Ψ' states decaying into $\mu^+\mu^-$.

• Experiment CFS

An experiment performed by a collaboration between Columbia University, Fermilab and State University of New York at Stony Brook (23) (referred to as CFS) measured the cross sections for J/Ψ and Ψ' decaying into e^+e^- using a 400 GeV/c p beam on Be target.

Figure 1.4-c: Experimental setup and di-μ mass spectrum from different beams from the experiment E537.

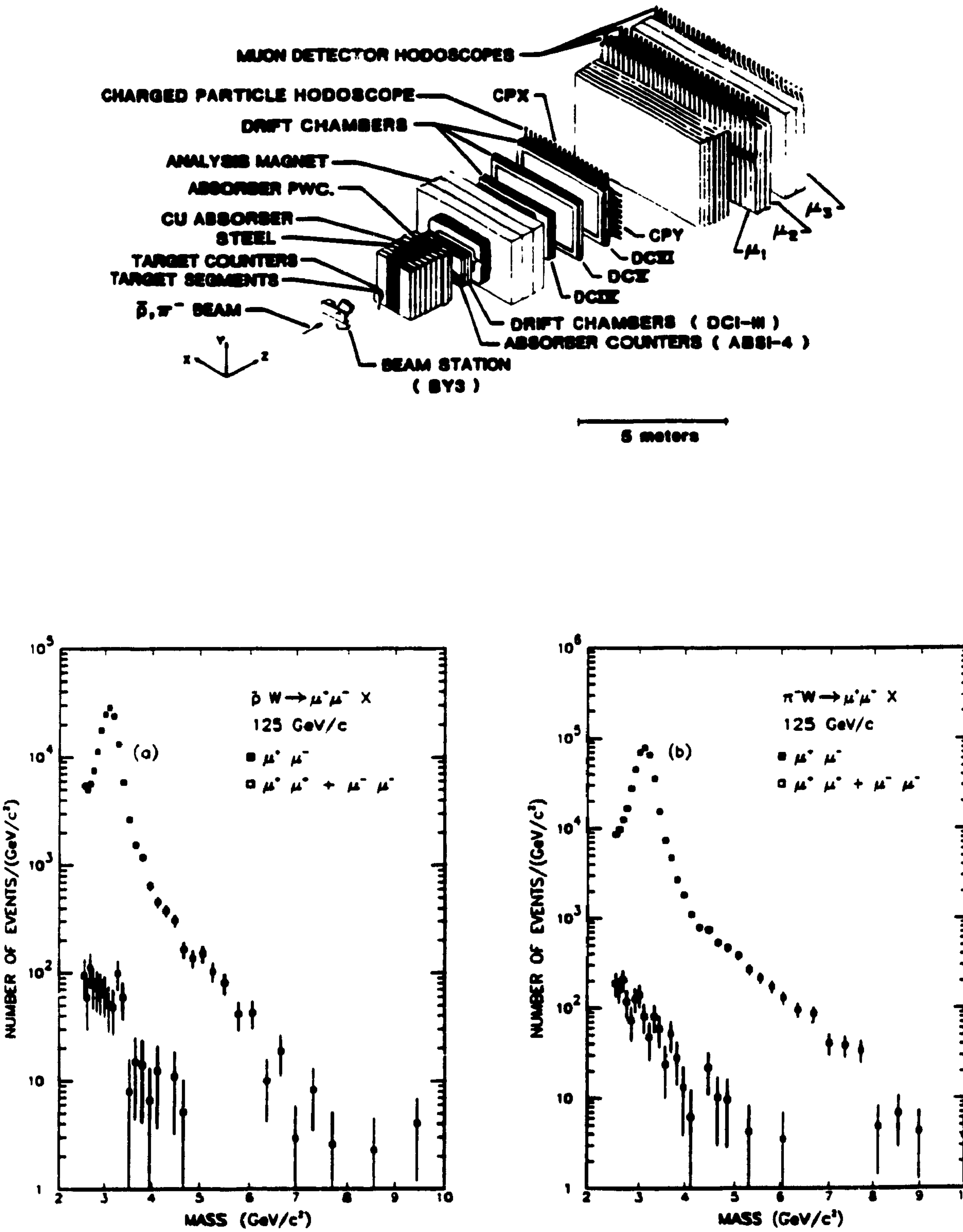

Figure 1.4-d: Experimental setup and di-μ mass spectrum from the experiment NA3 for 200 GeV/c π^+ on different targets .

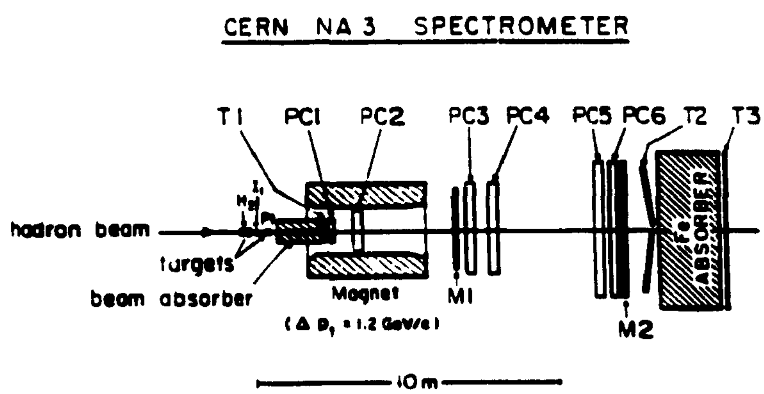

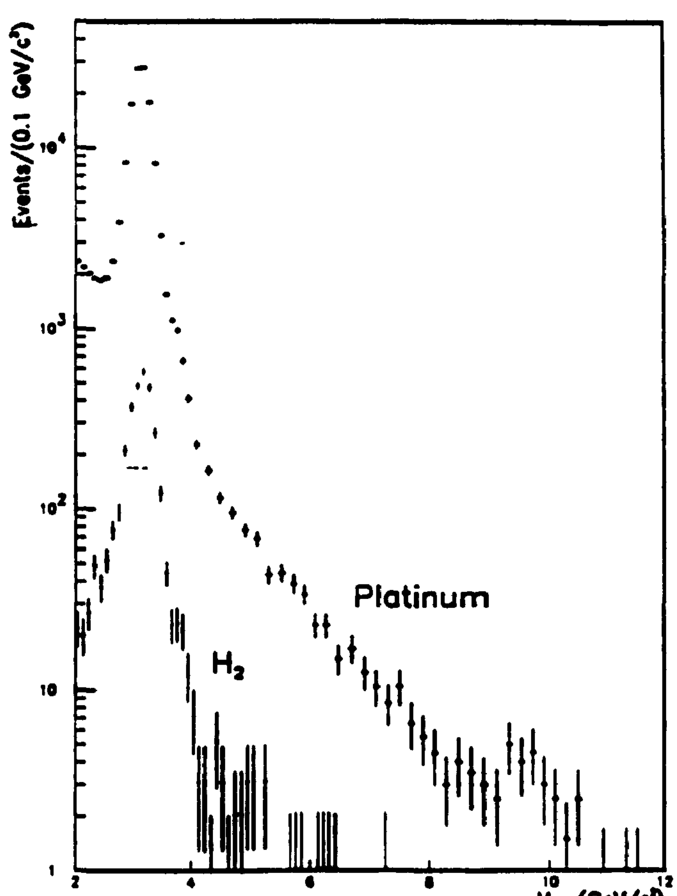

FIG. 1

• Experiment CS

An experiment made by a collaboration between the California Institute of Technology and Stanford University (21) (referred to as CS), using a 400 GeV/c p beam incident on an iron target, measured the cross section for J/Ψ decaying into a μ pair.

• ISR experiment

An experiment realized at the CERN ISR (24) (Intersecting Storage Ring) measured the cross sections of the J/Ψ and Ψ' states decaying into e^+e^- using colliding p $\bar{p}$ beams at two center of mass energies, 52 and 63 GeV.

• Experiment M-D at VEPP4

The experiment M-D (15) made at the VEPP4 e^+e^- colliding ring is cited here because of its accurate measurement of the J/Ψ and Ψ' masses. The J/Ψ mass was found to be 3096.93 ± 0.09 MeV/c^2, and the Ψ', 3686.0 ± 0.1 MeV/c^2.

1.4 χ hadronic production

The major motivation for doing experiment E705 was to study χ production by hadronic interactions. The basic processes for χ hadronic production are shown on figure 1.5. Because of Yang's rule(16) (spin 1 + spin 1 $\nrightarrow$ spin 1), the χ_1 state (in analogy with the J/Ψ) cannot be produced by the simple fusion of two gluons (figure 1.5-a). However, figure 1.5-c shows a possible gluon fusion process, called color evaporation, that could produce a χ_1 state. The two interacting gluons produce an intermediate colored state. The color symmetry is then re-established by the emission of a soft gluon.

Figure 1.5: Basic processes contributing to χ production a) gluon fusion, b) quark fusion, and c) color evaporation

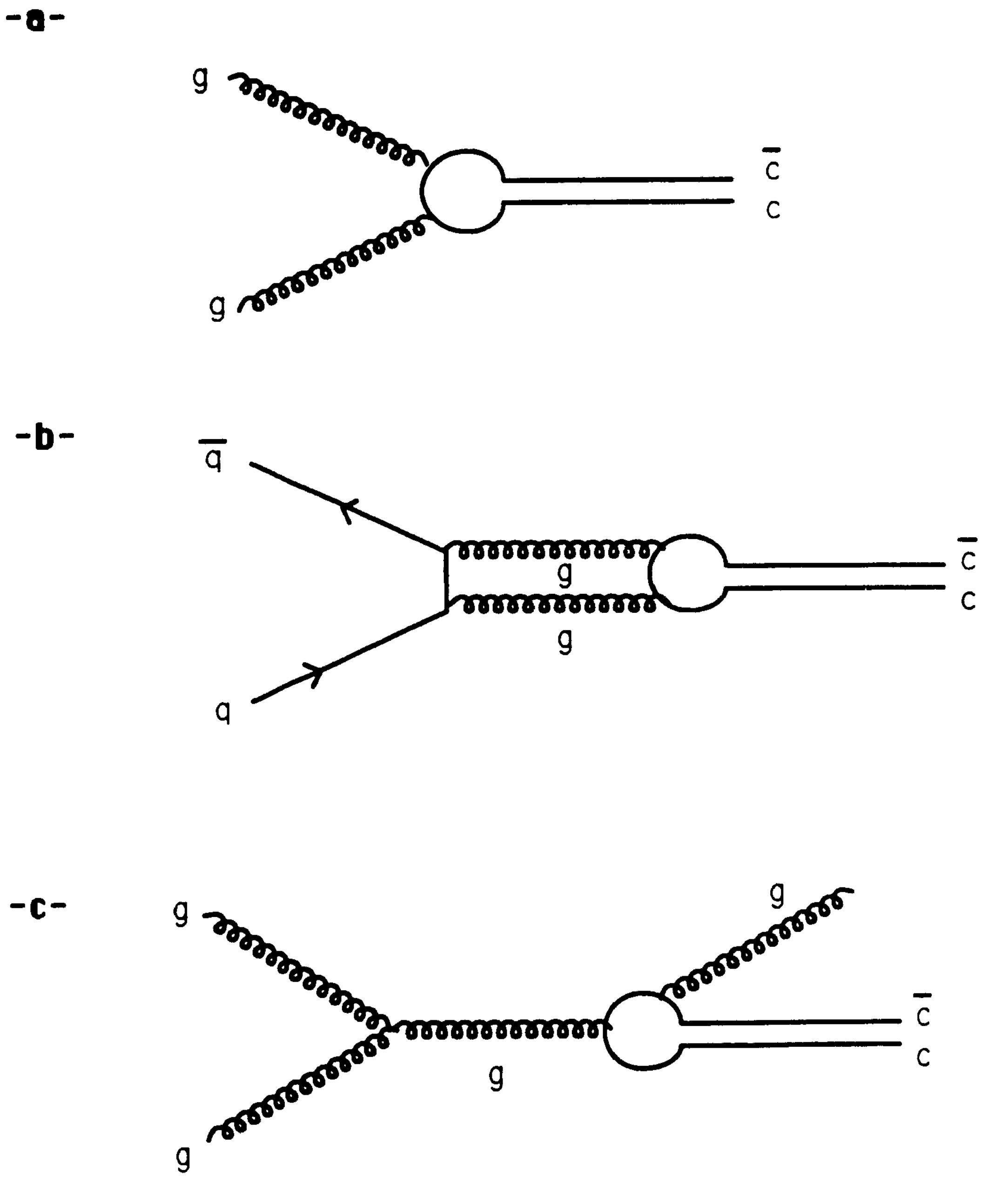

It is possible to find the contribution of each process to the χ production by looking at the decay $\chi \rightarrow J/\Psi + \gamma$, and measuring the emission angle of the photon in the rest frame of the χ. Using a simple model where the transverse momentum of the parton inside the hadron is neglected, B.L. Ioffe(17) predicted that the angular distributions of the photon should be very different depending on whether the χ's are produced by gluon or quark fusion. The predicted distributions are (17):

Gluon fusion $1 - 1/3 \cos^2\theta$

Quark fusion $1 + \cos^2\theta$.

Using an electromagnetic detector made of lead glass and scintillation glass to detect the photons, and a charged track detector to identify the J/Ψ states decaying into a μ pair, experiment E705 aims to evaluate the contribution of each of those processes involved in the χ production. The χ_0 state was not expected to be observed because of its small branching ratio for the electromagnetic channel (only 0.7% of the χ_0 states decay electromagnetically, compared to 18% for the χ_1 and 13% for the χ_2).

CHAPTER 2

Apparatus

Experiment E705 was located at Fermilab in the high intensity experimental area served by the "proton west" beam line. The beam for the experiment was a 300 GeV/c beam produced by the interaction of the 800 GeV/c primary proton beam extracted from the Fermilab Tevatron. In the positive mode, the beam was composed of 45% π^+, 55% protons, with a small contamination of K^+ which was neglected. In the negative mode, a 98% π^-, 2% anti-proton tertiary beam was produced from the decay of the neutral secondary particles (Λ^0, $\bar{\Lambda}^0$ and K^0). The beam was made to hit a lithium target and the product of the interactions were detected using a large aperture spectrometer.

The main purpose of the spectrometer was to detect the muons from the J/Ψ decay, the γ from the decay $\chi \rightarrow J/\Psi + \gamma$ and the γ produced directly in the interactions. The muons were detected using charged track detectors consisting of multi-wire proportional chambers, drift chambers and plastic scintillators, positioned in front and behind an analysis magnet. The di-μ events, quickly identified by means of three scintillator hodoscopes located behind a hadron absorber, were then analyzed by means of a trigger processor which rejected the events with a di-μ invariant mass lower than 2.4 GeV/c^2. The photons were detected using a lead glass/scintillation glass electromagnetic calorimeter. The trigger for the direct photon part of the experiment was provided by an analogue processor that looked for energy cluster in the glass calorimeter. A general view of the E705 spectrometer is shown on figure 2.1.

Figure 2.1: E705 spectrometer.

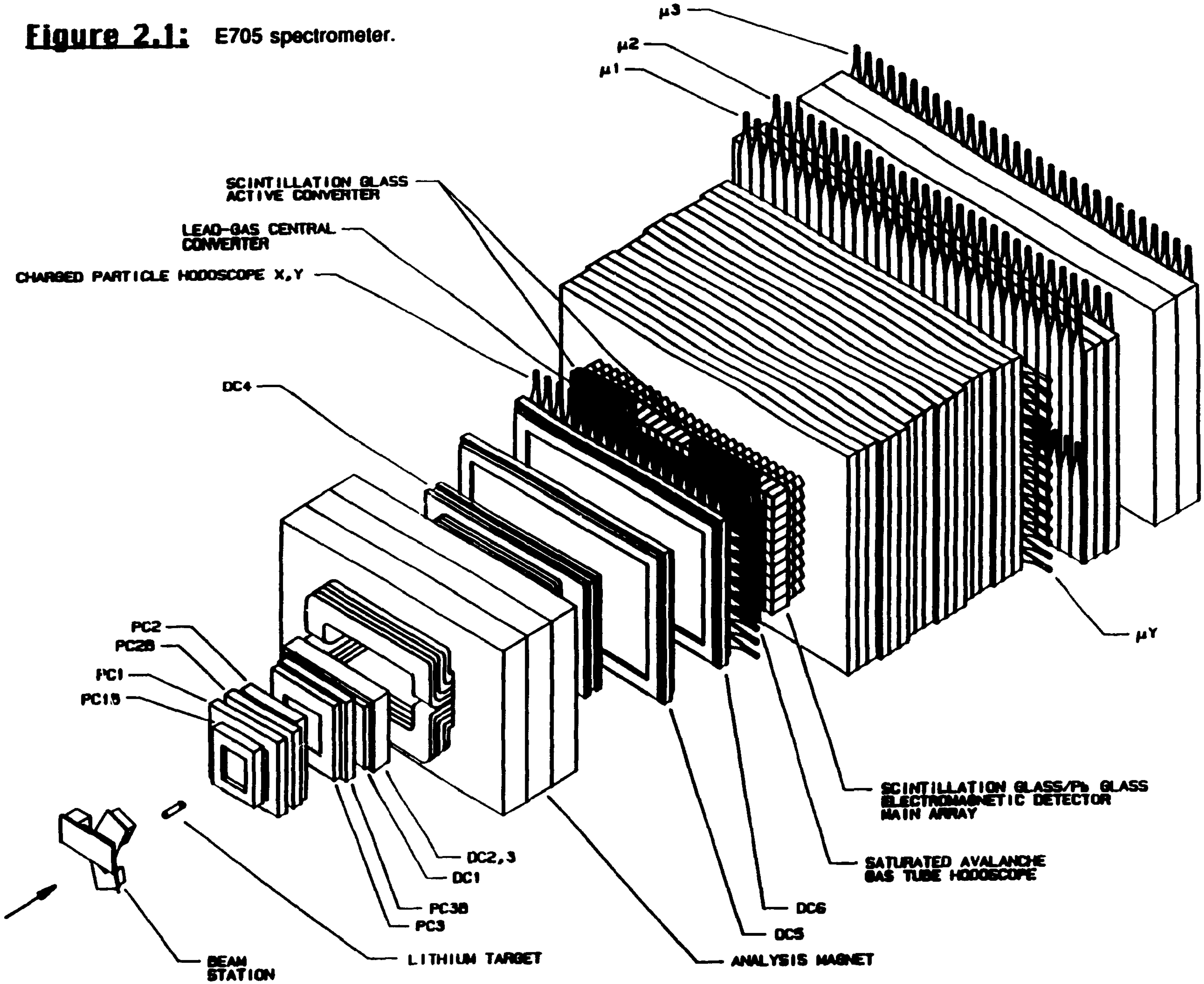

2.1 Accelerator

The accelerator at Fermilab was an 800 GeV/c proton synchrotron. The protons were extracted from a hydrogen gas source and accelerated to 750 KeV/c using a Cockroft-Walton electrostatic accelerator. The protons were then accelerated further to 200 MeV/c by a linac from where they were injected into an 8 GeV/c booster synchrotron. From the booster, the protons were transferred into a 1 km radius synchrotron, the main ring, until the momentum reached 150 GeV/c. An other synchrotron, the Tevatron, superimposed to the main ring but using superconducting magnets, received the 150 GeV/c protons and increased their momentum to 800 GeV/c.

Rather than operating in a continuous mode, the beam from the Tevatron was extracted in the form of 20 seconds spills, each spill being separated by a 40 seconds period. The Tevatron cycle began with a magnet ramp where the Tevatron magnet current was increased for a period of 10 seconds until it reached its nominal value. The beam was then delivered to the experimental areas for a period of 20 seconds. The magnet current was decreased over a period of 10 seconds, and was maintained off for a period of 20 seconds, completing the Tevatron cycle. The particles within a spill were clustered into buckets 19 ns apart from each other. The interbucket spacing reflected the radio frequency voltage used in the main accelerator.

2.2 Beam

2.2-a Secondary beam production

The beam for the experiment was a mixture of pions and protons. It was obtained from the interaction of the primary proton beam in a beryllium target located upstream of the E705 experimental area. Negative and positive beams were used alternatively during the data acquisition period. The negative beam was obtained by using the π^- and $\bar{p}$ coming from Λ^0, $\bar{\Lambda}^0$ and K^0 decay, which were produced from the interaction of the primary beam. The positive beam was produced by collecting the π^+ and protons directly from the interaction of the primary beam. Once the secondary particles were produced, a momentum slit selected the particles with a momentum of 300 GeV/c. The pions and protons were then transported and focused on the experimental target. The beam shape at the target entrance was nearly circular, with a radius of approximatively 2 cm.

2.2-b Beam chambers

In order to reconstruct the beam particle trajectories, three multi-wire proportional chambers (or MWPC), BC-1, BC-2 and BC-3, were installed before the experimental target at distances of respectively 62, 37 and 5 meters from the target. Each chamber consisted of one Y plane with the wires oriented along the x direction, and two others (U, V) with the wires rotated by -60 ° degrees and +60 ° respectively from the x direction. Each signal plane was made of 128 tungsten wires of 12.5 μ diameters, two adjacent wires being spaced by 1 mm. The chambers were run with a gas mixture of 77% argon, 16.7% isobutane, 6% methylal and 0.3% freon.

2.2-c Beam counters

Each beam chamber had a scintillator hodoscope associated to it. The beam hodoscopes, called BY-1, BY-2 and BY-3, were used to define the beam in the trigger logic. The hodoscopes were made of .32 cm thick, 13 cm long, plastic scintillators, with a width ranging from 2.3 cm for the counters far from the beam, to .8 cm for the central counters. Each hodoscope covered a 13 cm X 13 cm active region.

2.2-d Cerenkovs

The beam particles were identified as proton or pions using two gas Cerenkov counters, C1 and C2. The gas in the counters was a mixture of 80% helium and 20%

nitrogen. The light in the Cerenkov was reflected by a 33 cm diameter mirror, made of aluminized lucite, whose radius of curvature was 4.6 m . The light was focused on a RCA 31000M photomultiplier through a 7.6 cm diameter quartz window. The pressure inside the counters was set to detect pions, that is 1.6 PSIA. The pions were defined if a signal was present in any of the two Cerenkovs counters, while the protons (or antiprotons) were defined if no signal was present. The Cerenkov counter efficiencies were determined by looking at the proportion of pions where only one Cerenkov gave a signal. The efficiencies were determined this way to be 92% in average for both counters.

2.3 T1 counter

Located after the last beam chamber, a 1 cm thick, 20 X 10 cm^2 plastic scintillator, referred to as T1, was a timing reference for the spectrometer. The T1 counter was required in the beam trigger logic along with the beam counters. It was located before the veto wall and the target.

2.4 Veto wall

The veto counter wall was installed before the target to eliminate halo muons. The veto counters were in anti-coincidence with the beam definition, so that events with halo muons were not triggered. This veto wall was made of two hodoscopes, VX and VY, the VX hodoscopes having the counters oriented in a vertical position, while the VY counters were oriented along the horizontal position. The wall dimensions were 408 X 147 cm^2 for VX with a central hole of 25.4 X 8.8 cm^2, and 306 X 153 cm^2 for VY with a hole of 8.8 X 25.4 cm^2. A sketch of the veto wall is shown in figure 2.2.

Figure 2.2: Schematic view of the veto wall.

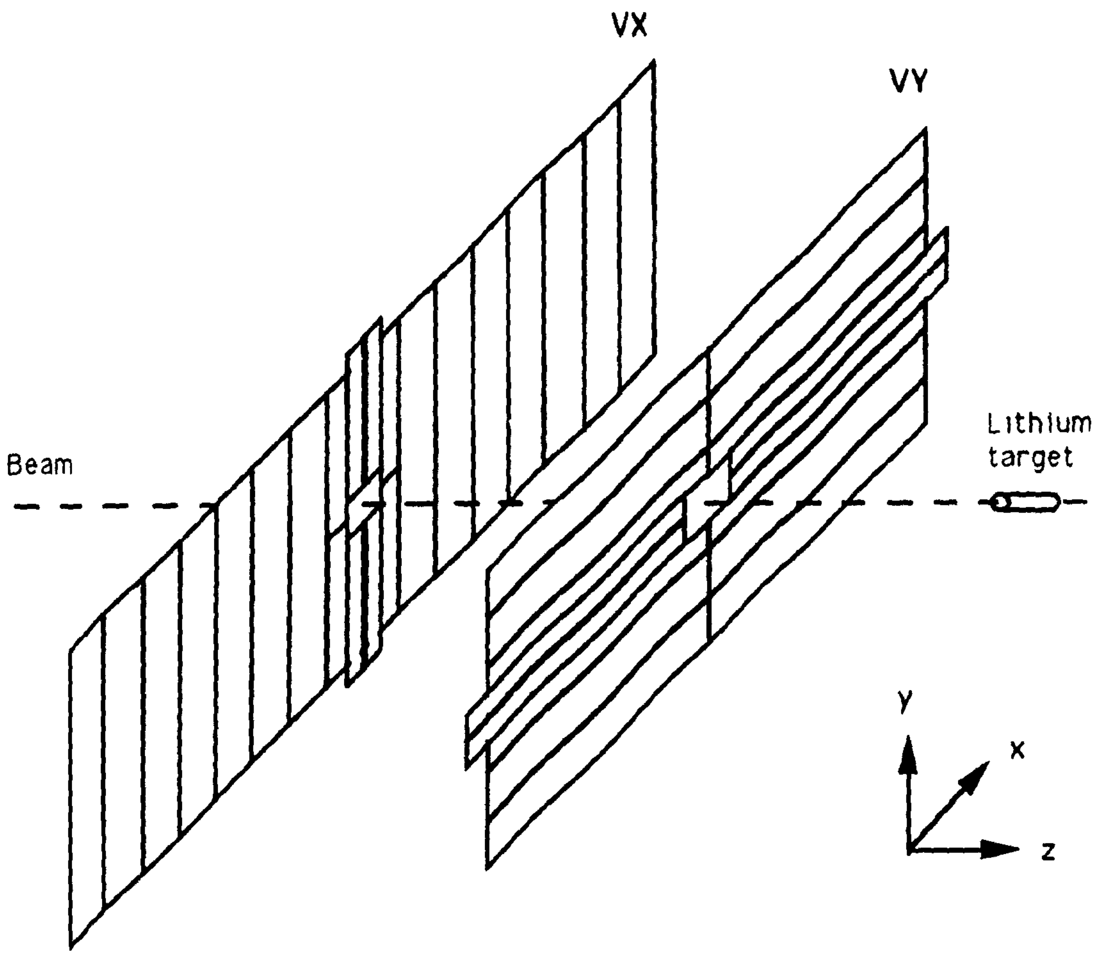

2.5 Target

The target was a 5.0 cm radius, 32.9 cm long, lithium cylinder. Its position along the z axis was -5.33 m with respect to the center of the analysis magnet. The effective lengths of the target relative to the incident beam are listed in table 2.1.

Table 2.1: *effective length of the target relative to the beam constituent*

	π^+	π^-	p	$\bar{p}$
absorption length (cm)	187.6 ± 6.5	189.3 ± 5.0	138.3 ± 4.4	130.0 ± 4.7
target length (in absorption lengths)	(17.5 ± 6)%	(17.4 ± .5)%	(23.8 ± .8)%	(25.3 ± .9)%
effective length (cm)	30.19 ± .09	30 22 ± .07	29.30 ± .11	29.08 ± .13

2.6 Small angle tracks MPWC

The first set of chambers in the di-μ detector were the small angle track chambers, or PCB's. The tracks near the beam were not detected by the other front chambers because their center were desensitizeu. The PCB chambers were implemented to detect those small angle tracks as well as helping the overall track reconstruction. The signal planes were made of gold-plated tungsten-rhenium wires. The gas mixture used was the same as for the beam chambers. The dimensions for the PCB's are listed in Table 2.2 .

Table 2.2: *wire spacing, aperture, and signal plane diameters for the PCB chambers*

	wire spacing (mm)	aperture (cm^2)	diameter of the signal wires (μ)
PCB-1	0.75	60 x 30	12.5
PCB-2	0.75	75 x 40	12.5
PCB-3	1.00	90 x 50	12.5

2.7 Large angle tracks MPWC

In conjunction with the PCB's, a second set of chambers, the large angle tracks MPWC or PC's, were installed in the detector. There were three PC's positioned along the beam axis in alternance with the PCB's, as can be seen on figure 2.1. PC-1 had four planes, two X planes, and two other planes, U and V , rotated from the vertical axis by 16.7 °. PC-2 and PC-3 had each three planes, X U and V, the U and V plane having the same angle of + and - 16.7 ° with the Y axis. The signal planes were made of tungsten wires. A circular region at the center of each plane was desensitized. The same gas mixture was used for the PC's as for the beam chambers. The dimensions for the PC chambers are listed in Table 2.3 .

Table 2.3: *Apertures , dead region,wire spacing and signal wire diameters, for PC chambers*

	wire spacing (mm)	aperture (cm^2)	diameter of the signal wires (μ)	radius of the dead region (cm)
PC-1	1.5	54 x 29	15	5.08
PC-2	2.1	76 x 40	15	5.08
PC-3	2.1	106 x 50	15	6.35

2.8 Drift chambers

The next element employed for track reconstruction was a set of six drift chambers, called DC-1 to DC-6. The first three drift chambers, DC-1, 2 and 3 were located between the PC chambers and the analysis magnet. Each of the front chambers had three planes, X U and V, the U and V planes making an angle of + and - 16.7 ° with the Y axis. The other three chambers, DC-4, 5, and 6, were located in the back of the magnet. Each back drift chamber had four signal planes: two planes with the wires oriented along the vertical axis, denoted X and X', and two other planes, V and U, rotated by +16.7 ° and -16.7 ° respectively from the vertical axis. All the drift chamber planes had their center desensitized near the beam region. The shape of the dead region was circular for the front chambers and rectangular for the back chambers. The gas used in the drift chambers was a 50% argon, 50% ethane mixture. The apertures, sizes of the dead regions, wire spacing and signal wire diameters are listed in Table 2.2.

Table 2.2: *Drift chamber apertures , dead region,wire spacing and signal wire diameters*

	wire spacing (cm)	aperture (cm^2)	diameter of the signal wires (μ)	dimension of the dead region
DC-1	0.60	50 x 50	20	6.35 cm radius
DC-2	1.27	50 x 50	25	6.35 cm radius
DC-3	1.27	50 x 50	25	6.35 cm radius
DC-4	1.95	200 x 100	25	30.48 x15.24cm^2
DC-5	1.95	335 x 167	25	30.48 x15.24 cm^2
DC-6	1.95	335 x 167	25	30.48 x15.24 cm^2

The drift time information was coded by time to digital converters (TDC) coupled to the signal wires. The TDC code full range was 512 counts, 1 count corresponding approximately to 1 ns. The signal from the wire started the count of the TDC, which was then stopped by the event trigger.

2.9 Analysis magnet

The magnet was made of 240 turns saddle shape coils. Running at a current of 3100 amperes, it produced a field of 1300 gauss in the Y direction, and induced a horizontal momentum kick of 766 MeV/c. The current in the coils was monitored by a current shunt, while the field was monitored using a Hall probe located at the bottom center inside the magnet. The dimensions of the magnet were 185.5 cm in x, 108.1 cm in y and 58.4 cm in z.

2.10 Charged particle hodoscopes

Two scintillator hodoscopes were mounted downstream of the rear drift chambers. The first one, called CPX, consisted of 184 vertical counters arranged in two rows of 92 counters. The second one, CPY was formed by 48 horizontal counters arranged in two columns of 24 counters.

The CPX counters were made of 1 cm thick, 4 cm wide and 100 cm long NE110 plastic scintillator. The wall covered an overall surface of 384 X 200 cm^2, with a hole of 33 X 33 cm^2 around the beam axis. The CPY counters were 1 cm thick, 8 cm wide and 200 cm long, and the wall dimensions were 400 X 188 cm^2, with a 32 X 32 cm^2 hole around the beam axis. A sketch of the CPX and CPY hodoscopes is shown on figure 2.3.

Figure 2.3: Front view of the a) CPX, b) CPY hodoscopes.

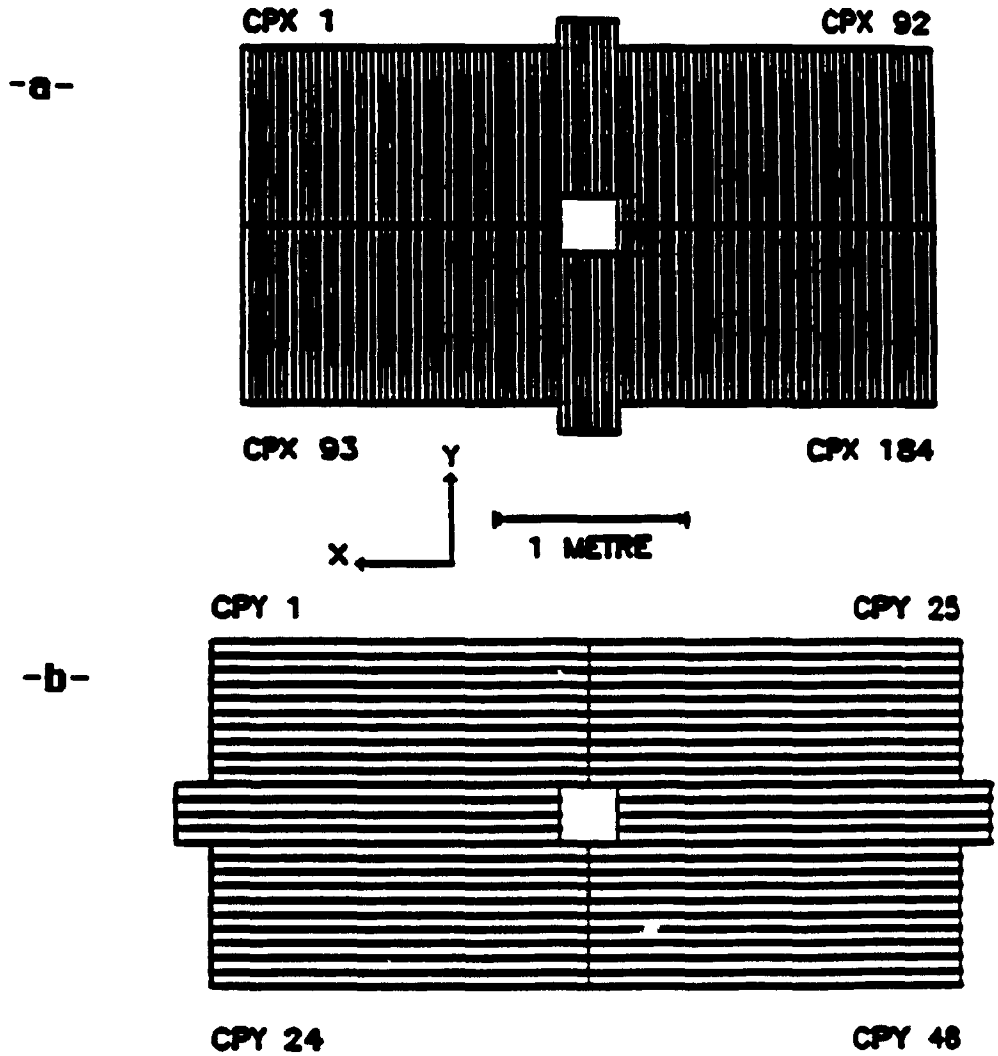

2.11 Electromagnetic calorimeter

The electromagnetic calorimeter was used to measure the energy and position of the photons produced in the interactions. It was located immediately downstream of the CPX and CPY hodoscopes. The main component of the electromagnetic calorimeter was a 1.95 x 3.75 m^2 glass array divided in three regions as shown on figure 2.4. The inner region was made of 92 scintillation glass (SCG1-C) blocks with dimensions of 7.5 x 7.5 cm^2. The second region was made of 86 scintillation glass (SCG1-C) blocks each 15 x 15 cm^2. The outer region consisted of 228 lead glass blocks(SF5) with dimensions of 15x15 cm^2. A precision measurement of the position of the photons was achieved by mean of a lead and proportional tubes (1 cm pitch) sandwich (LGC), and a 0.9 cm pitch gas tube hodoscope (GTH) located in front of the main array. The gaz tube hodoscope was preceded by two rows of 1.75 radiation length scintillation glass blocks used as active converters.

2.12 Muon detector

The muon detector included four hodoscope walls, μ-Y, μ-1, μ-2 and μ-3, embedded in thick layers of concrete, steel and copper absorbers. The μ-Y hodoscope was located behind a copper absorber 40.6 cm thick and a steel absorber 309.9 cm thick. This hodoscope was made of four vertical columns of plastic scintillators (see figure 2.5-b). The steel absorber covered the entire surface of the μ-Y wall. The copper absorber however, while covering the entire Y dimension of the μ-Y wall, covered only a 182.8 cm wide X central region. The μ-1 hodoscope, located behind the μ-Y hodoscope, was made of plastic scintillators arranged in two rows of 30 counters each. Proceeding downstream, the μ-2 hodoscope was located behind a 61.0 cm thick steel absorber, and was made of 62 plastic scintillators arranged in two rows of 31 counters each. The adjacent μ-2 counters had a 1 cm overlap with each other. The μ-3 hodoscope was located behind a further 9 cm

Figure 2.4: Electromagnetic calorimeter.

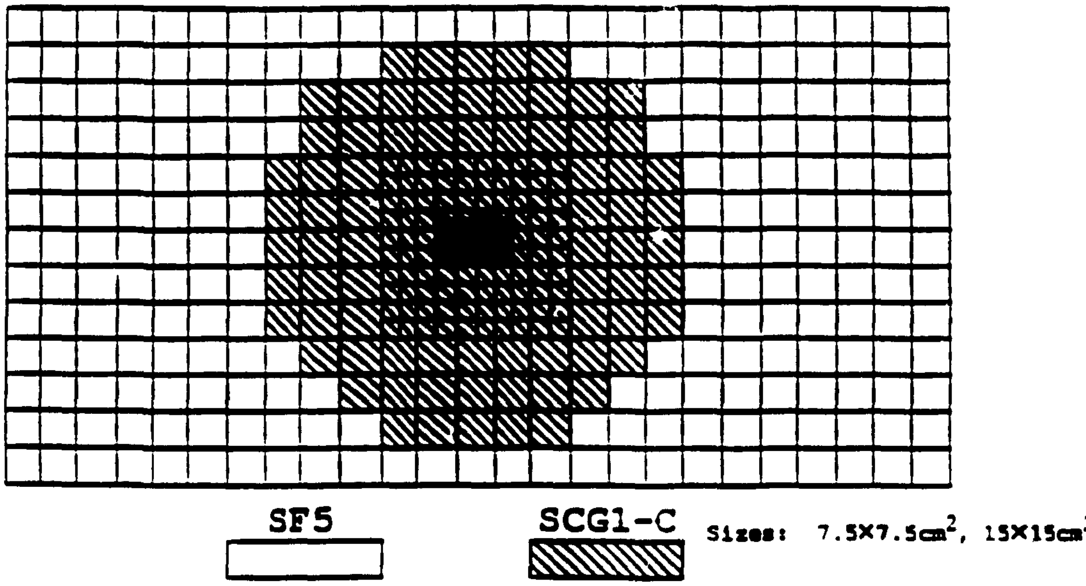

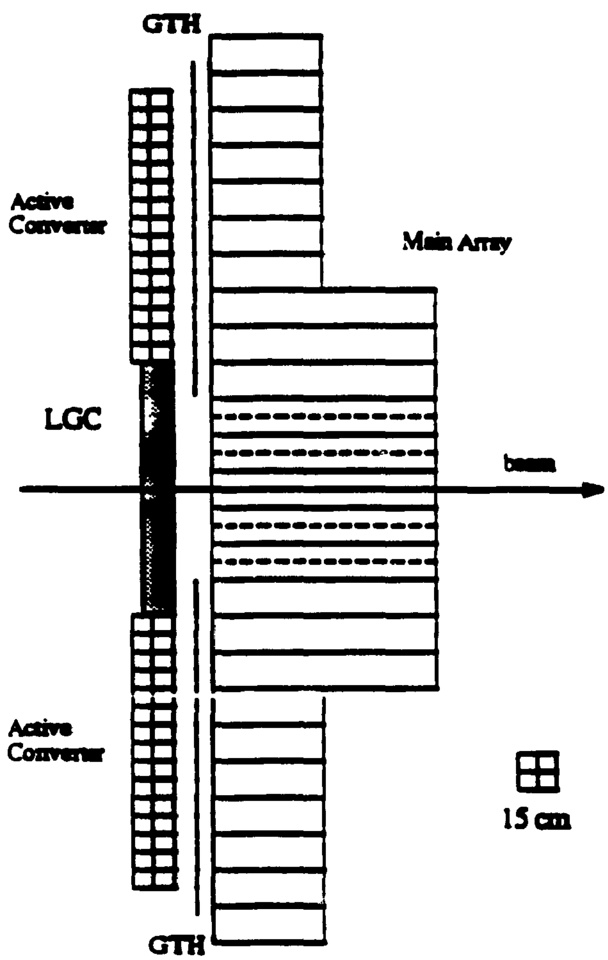

concrete absorber, and consisted also of 62 plastic scintillators. The μ-3 counters had a 3 cm overlap among adjacent counters.

All hodoscopes of the muon detector had an empty rectangular hole around the beam axis. The dimensions of the muon hodoscopes are listed in table 2.3. Sketches of the μ-Y and μ-1 hodoscopes are shown on figure 2.5. The muon detector was designed to detect muons with at least 6 GeV/c momentum, which was the minimum momentum required for a muon to cross the absorbers and reach the last hodoscope wall.

Table 2.4: *Counter, hole and overall wall dimensions for the muon detector hodoscopes.*

	Scintillator material	Counter dimensions $(\Delta X \times \Delta Y \times \Delta Z)(cm^3)$	Wall dimensions $(\Delta X \times \Delta Y)(cm^2)$	Hole dimensions $(\Delta X \times \Delta Y)(cm^2)$
μ-Y	NE114	129x13x1(inner rows) 187x13x1(outer rows)	620 x 285	40.6 x 40.6
μ-1	NE114	20.3 x 145 x 1	618 x 290	40.6 x 40.6
μ-2	NE114	22.9 x 157 x 1	671 x 315	40.6 x 40.6
μ-3	NE114	26.7 x 176 x 1	723 x 352	87.[illegible] x 40.6

2.13 Triggers

2.13-a Interaction trigger

The first step in the selection of the di-μ and the direct photon events was achieved through the definition of the interaction trigger. The interaction condition was satisfied

Figure 2.5: a) Front view of the µI hodoscope,
b) µY hodoscope.

-a-

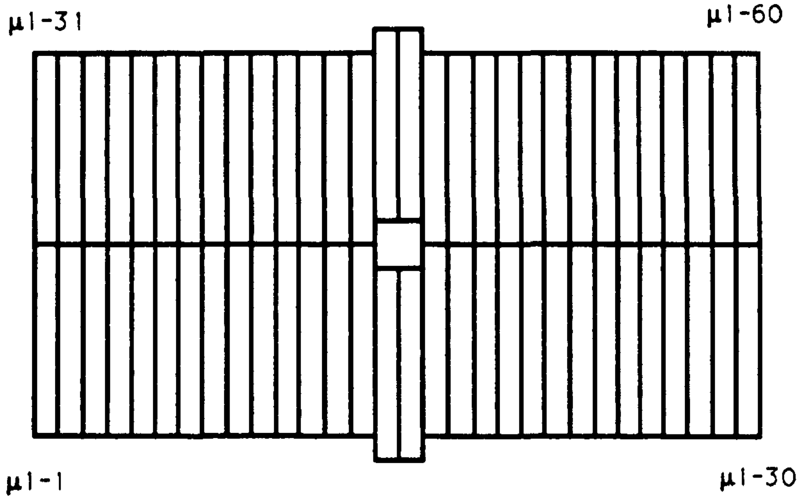

-b-

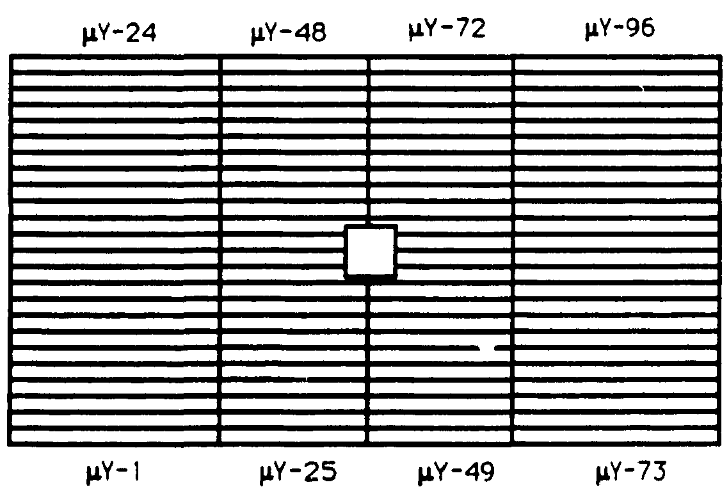

when two or more particles hit the CPX and CPY counters while a proton or a pion was present in the beam detector. More specifically:

$$\text{INTERACTION} = (\pi + p) \cdot (\Sigma\text{CPX} \geq 2) \cdot (\Sigma\text{CPY} \geq 2)$$

where π and p were defined using the Cerenkov counters and the beam signal

$$\pi = (\text{C1} + \text{C2}) \cdot \text{beam}$$

and

$$p = \overline{(\text{C1} + \text{C2})} \cdot \text{beam}.$$

The beam definition required a signal from T1, at least one counter hit in each of the beam counter planes, and no counter hit in VX and VY planes

$$\text{beam} = \text{T1} \cdot (\Sigma\text{BY1} \geq 1) \cdot (\Sigma\text{BY2} \geq 1) \cdot (\Sigma\text{BY3} \geq 1) \cdot (\overline{\text{HALO}})$$

with

$$\text{HALO} = (\Sigma\text{VX} > 0) + (\Sigma\text{VY} > 0).$$

2.13-b Di-μ trigger

The di-μ trigger was satisfied if at least two muons were detected in the muon detector, in coincidence with the interaction trigger. The logic applied in this trigger was the following. A single muon was defined as the triple coincidence of a μ-1, a μ-2, and a μ-3 counter aligned together. The logical definition of the triple coincidences (or TC) is illustrated in figure 2.6. The coincidences were grouped in four quadrants in the following way:

quadrant 1 = TC -1 to 15

quadrant 2 = TC -16 to 30

quadrant 3 = TC -31 to 45

quadrant 4 = TC -46 to 60

Figure 2.6: Triple coincidence logic.

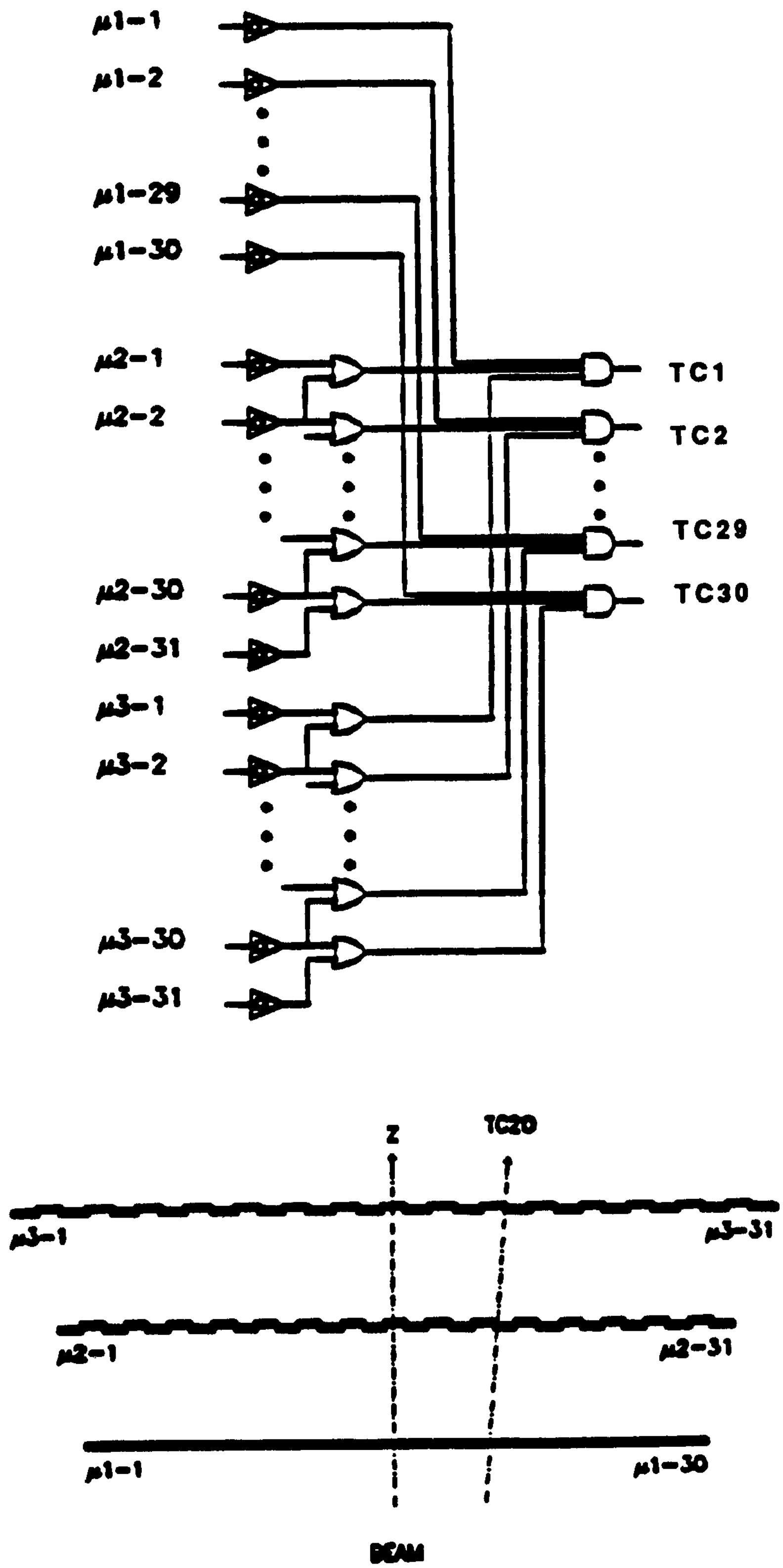

The di-μ trigger condition was satisfied if at least two triple coincidences from different quadrant were present in a given interaction.

The interaction rate during the data acquisition was 620 kilo-hertz in average, and the number of di-μ trigger per interaction was approximatively 10^{-3}. The major contribution to the di-μ triggers was due to muons coming from decays of pions and kaons produced in the interactions.

2.14 Trigger processor

The trigger processor algorithm and performance are briefly described below. For a more complete description, the reader can refer to a previous publication (18). The trigger processor selected the high mass di-μ's by performing a fast track reconstruction, and calculating a mass for every track pair combination. The events that had at least one combination with a mass greater than 2.4 GeV/c^2 were accepted and written on tape. The tracks were found using the x and x' planes of the rear drift chambers. The drift time was not used, so that only the wire position was known in the trigger processor tracking. The tracks found were required to point to a CPX counter and to a triple coincidence. Since only the x-z coordinates of the tracks downstream of the magnet were used, the tracks were assumed to come from the target center. Since the bending in the analysis magnet was applied in x only, the information from the μ-Y counters was sufficient to give the y trajectory of the track. If more than one μ-Y counter was consistent with a track, the trigger processor attributed to the track the counter that generated the widest angle between the two muons. Since the mass is proportional the the angle between the muons, this way of finding the y position of the track did not underestimate the mass.

In order to speed up the time of analysis of the trigger processor, only a subset of the drift chamber hits was utilized for the tracking. To select the hits, the trigger processor, for each triple coincidence, defined a region of the drift chamber planes from geometric criterion. An estimated 10 ± 5% of the J/Ψ decay events had some hits outside those regions and were rejected by doing the hit selection .

Once all the tracks were found and the mass had been calculated for all the combinations of opposite sign tracks, the event with mass lower than 2.4 GeV/c^2 were rejected. This value for the mass cut rejected 75% of the di-μ triggers while accepting 90 ± 5% of the J/Ψ 's, so that the overall acceptance of the trigger processor was evaluated to be 81 ± 7%. Some events (~2% of the initial di-μ triggers) were accepted without a final answer because of a time limit imposed for the trigger processor analysis.

Chapter 3

Data acquisition and calibration

3.1 Data acquisition

The E705 data acquisition extended over a nine month period, from June 1, 1987 to February 15, 1988. The nominal event acquisition rate was 130 events/second, including the di-m triggers (~75%) and the photon triggers (~25%). The E705 data acquisition system(26) was designed to handle a rate up to 200 events/second, with a dead time less than 20%. During the data acquisition, the performance of the apparatus was monitored regularly by running analysis programs on the accepted events as they were triggered. This permitted a constant knowledge of the behavior of the different components of the spectrometer (drift chambers, MPWC's, scintillators, electromagnetic calorimeter, etc).

3.2 Calibration

Special runs were made periodically to calibrate the spectrometer. The precise position of the chambers and of the scintillation counters was found by analyzing interaction events written on tape while the analysis magnet was turned off. The tracks of the particles coming from interactions in the target were used as straight line references to evaluate the relative position of the chambers. Special runs using an electron beam were also written on tape for different energies between 2 and 100 GeV, to calibrate the electromagnetic calorimeter. The electron runs, with the beam properly deflected to cross the active region of the chambers, were also used to evaluate the chamber efficiencies.

3.2-a Chamber resolution

The chamber resolution was found using the following technique. The charged particle tracks from interaction events were found in the front and rear of the magnet using the same tracking and fitting technique as the one described in the next chapter (see sections 4.4-a and 4.4-c). However, the plane for which the resolution was measured was not used to find the tracks. The plane resolution was extracted from the residual distribution of the chamber hits with respect to the fitted track. The resolution for each chamber plane is shown on table 3.1. The error on the chamber resolution was less than 20 mm for all planes.

Table 3.1: *Proportional and drift chambers resolution*

	Resolution (mm)			
	X	X'	U	V
PC-1	691	579	714	666
PC-2	721		662	616
PC-3	794		704	727
DC-1	374		404	476
DC-2	376		407	383
DC-3	377		384	333
DC-4	675	718	669	598
DC-5	373	554	513	483
DC-6	665	737	698	524

3.2-b Drift Chamber TDC

The TDC value corresponding to a zero drift time (or a hit next to the wire), denoted T0, varied from wire to wire depending upon the delay cables employed to transport the hit signals, and the response of the electronics used to record the TDC information. The T0's were calibrated periodically for each wire.

Using the TDC information, the value of the drift distance was given by:

$$D_{drift} = (T0_{wire} - TDC) \times V_{drift}$$

where T0 = TDC count for a hit next to the wire,

TDC = value recorded by the Time to Digital converter,

V_{drift} = drift speed

$$= \frac{L_{cell}}{(T_{high})_{plane}} \; ,$$

L_{cell} = distance bewteen the wire and the edge of the drift chamber cell,

$(T_{high})_{plane}$ = Maximum drift time for a given plane, which corresponds to the time taken by a hit on the edge of the cell to drift to the wire.

The drift chamber TDC were corrected in the data analysis program for non-uniform drift speed within the drift chamber cells. The non-flat shape of the drift distance distribution inside a drift chamber cell, as shown in figure 3.1, is characteristic of the position dependance of the drift speed. The shape of the distribution was fitted to a polynomial function and the data was corrected using this fit to obtain a flat distribution for the drift time.

Figure 3.1: Drift distance distribution for the plane DC6-X a) uncorrected, b) corrected for non-uniform speed inside a drift chamber cell.

-a-

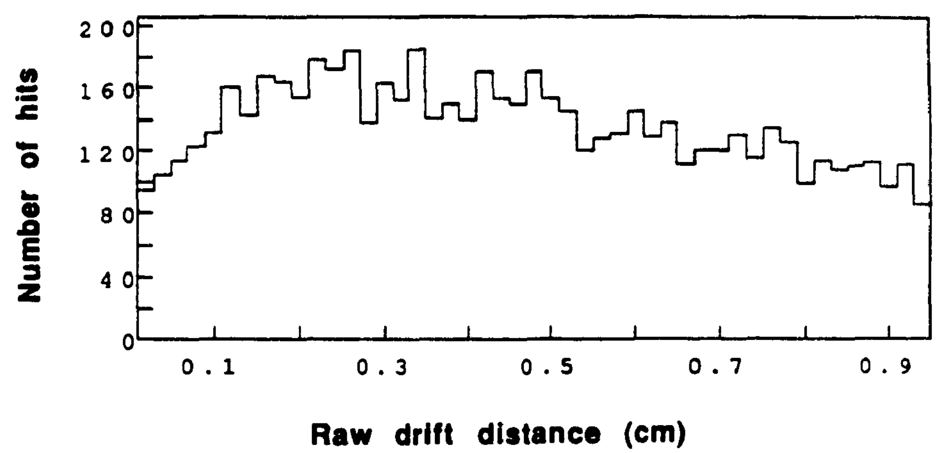

-b-

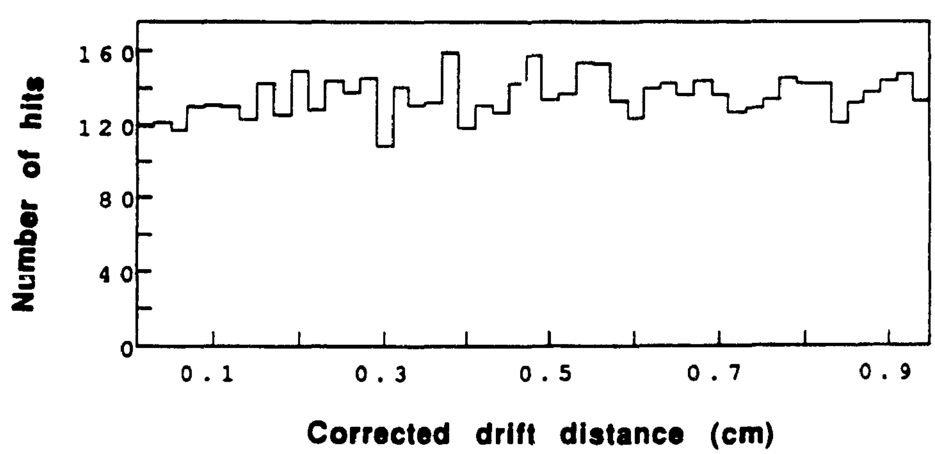

CHAPTER 4

Reconstruction

4.1 Data analysis scheme

The analysis for the di-μ triggers consisted of the several steps. First, the events were decoded, then the beam particle trajectories were reconstructed by the beam tracking (section 4.2). Next, the events were selected as high mass di-μ candidates by a fast filter algorithm (section 4.3), then fully analyzed by the di-μ reconstruction program. The muon tracks reconstructed by the di-μ program were employed to calculate the di-μ invariant mass, and the events with a mass < 2.0 GeV/c^2 were rejected. The remaining events were subsequently analyzed by a second pass program, whose purpose was to reduce the background under the J/Ψ peak by applying further cuts on the J/Ψ candidates (section 4.4).

The event analysis was performed using the Fermilab Advanced Computer Program (ACP) system (27). An ACP system consisted of a certain number (typically 100) of parallel processors called nodes, each processor analyzing an event independently of the others. On a 100 nodes system, the di-μ reconstruction was fast enough (50 ms/event) to compete with the time taken to read the events from the tape.

4.2 Beam tracking

The beam tracks were reconstructed using the three proportional beam chambers. The algorithm first defined (X,Y,Z) points in the chambers by making triplet combinations between Y, U and V hit wires. Then, the tracks were found by combining the triplet points of the three chambers. To avoid the loss due to chamber inefficiencies, the algorithm also defined doublets points using Y-U, Y-V or U-V wire combinations. After all the tracks using the triplet points were found, a further iteration was performed using the doublet points, and triplet points that had not been used to form tracks in the previous stage of the tracking. The largest part of the events (~65%) had only one beam track reconstructed. Few events (~5%) had no beam track, and the rest of the events (~30%) had more than one beam track.

4.3 Filter program

The purpose of the filter program was to pre-analyze the di-μ triggers in order to make a fast selection based on a rough estimate of the di-μ invariant mass. The algorithm of the filter program was very similar to the one of the trigger processor. However, the filter used the information from the drift chamber TDC's and from the beam tracking, which was not available to the online trigger processor. The drift time information, by giving a better accuracy on the position of the hits, allowed the filter to reject fake tracks coming from spurious hit combinations. Also, the better accuracy on the track position and the beam information increased the mass resolution of the filter, when compared to the trigger processor.

The events accepted by the filter were sent to the main di-μ program for complete analysis. No tracking information was passed by the filter program on the accepted events.

4.3-a Vertex position

The Z position of the di-μ vertex was not determined in the filter program, so the value used was the target center. The X and Y position of the vertex was approximated by projecting the reconstrcuted beam track to the Z position of the target center. If no beam track or more than one beam track was present in the beam telescope, the filter used the X and Y position of the target center as vertex position.

4.3-b Hit selection

Before reconstructing tracks, the filter applied a cut on the drift chamber hits based on the position of the muons in the muon detector. To every triple coincidence corresponded regions in the x and x' planes of the rear drift chambers where the muons from J/Ψ's were expected to be. The dimension of the regions was adjusted using a Monte Carlo simulation in order to accept more than 99.5% of the J/ψ events. For each event, the hits that were not inside the regions defined by the triple coincidences were deleted. This region cut rejected typically 25% to 30% of the hits of the drift chambers.

The filter rejected also the hits that were out of time. The information from the TDC's was first converted to drift time (see section 3.2-b: Drift chamber TDC). A hit was then rejected if the drift time was negative, or larger than the drift time corresponding to a hit on the edge of the drift chamber cells. Typically, this time cut rejected 15% of the drift chamber hits.

4.3-c Track reconstruction

In order to achieve a very fast algorithm, a starting set of tracks in the filter program was found without using the drift time information, so that the hit position was given by the position of the hit wire. In DC4 and DC6, the hits were defined by a wire from the x plane combined with its neighbor in the x' plane. If one of the planes was absent in the pair, the hit position was defined by the single wire. Next, a line was defined using a hit from DC4 and a hit from DC6. The line was accepted if a hit was found in DC5 within a certain search window. The left and right side of the window were the projections of the lines defined by the left and right edges of the cells in DC4 and DC6. At this stage, the typical number of tracks found in each event was 75. To eliminate fake tracks coming from spurious hit combinations, the filter rejected the tracks that didn't point to a CPX counter. The maximum distance between a track and the edge of a CPX counter was set to 2 cm to take into account the error on the track projection at the CPX plane. The CPX cut rejected between 30% and 35% of the tracks. Also, the program rejected tracks that didn't pass inside the analysis magnet (0.8% of the tracks). The tracks that made an angle with the z axis larger than 0.3 radian, the maximum angle for a track to intercept the muon wall, were also rejected. This angle cut rejected 16% of the tracks. Next, the filter applied a cut on the tracks that didn't point to the μ-1 counters, in order to reject non-muon tracks. A track was identified as a muon if its projection to the μ-1 wall intercepted a hit counter, or if the distance between the track and the edge of the nearest hit counter was less than 39 cm, which distance has been determined using the error on the track projection and the multiple scattering in the absorber in front of the μ-1 wall. The track projection error at the μ-1 plane for a track without the drift time information was 3.8 cm. Since the momentum of the muons was not known at this stage of the tracking, the filter used the multiple scattering for 6 GeV/c muons, which was the minimum momentum required for the muon to reach the μ-3 wall. This muon cut rejected 55 to 60% of the tracks. The mean track multiplicity at this stage of the tracking was 25 per event.

The drift time information was used at this point to increase the accuracy on the position of the tracks. Since, in the drift chambers, a given hit could have occurred either at the left or at the right of the wire, the filter defined two hits for each wire corresponding to the two possibilities. To solve this left-right ambiguity, the filter made all possible hit combinations among the left and the right possibilities, and selected the best one, with the following technique. A line was first defined using two hits from

DC4 and DC6. A window of ± 6 mm around the line was projected to the remaining planes. The combination that had more hits on its line was selected. If many combinations had the same number of points, the combination with the best χ^2 from a linear fit was then chosen. For a track to be accepted, the χ^2 per degree of freedom of the fit had to be less than 10. The number of tracks remaining after the χ^2 cut was 18 per event on average.

4.3-d Momentum and mass calculation

The projection of the momentum on the **x-z** plane is given by:

$$P_{x\text{-}z} = \frac{Pt_{kick}}{\sin(\theta_{front}) - \sin(\theta_{rear})}$$

where Pt_{kick} = .766 $(\mathrm{GeV/c})^{-1}$ was evaluated from a measurement of the magnetic field, θ_{front} and θ_{rear} were the angles between the track projection on the **x-z** plane and the **z** axis, in the front and the rear of the analysis magnet. The angle θ_{front} was calculated using the intercept of the rear track at the center of the magnet and the vertex position. The **y** component of the momentum was neglected, so that the approximation made was $P \simeq P_{x\text{-}z}$. The maximum error made by neglecting the **y** component of the momentum was given by:

$$\left(\frac{P - P_{x\text{-}z}}{P} \right)_{max} = 1 - \cos(\theta_{y\ max}).$$

Given the aperture of the spectrometer, the maximum y angle $\theta_{y\ max}$ was 6.2 °; hence, the maximum error on the momentum was 0.6%. Using the average **y** front angle for the J/ψ muons $\theta_{y\ av}$ = 1.9 °, the error on the momentum made by neglecting the **y** component was 0.05%.

The momentum resolution was given by the accuracy on the track position:

$$\frac{\Delta P}{P} = \frac{P}{Pt_{kick}} \Delta\vartheta$$

where $\Delta\vartheta$ is the error on the value $\sin(\theta_{front})$-$\sin(\theta_{rear})$. This error was given with a good approximation by:

$$\Delta\vartheta = \sqrt{\Delta\theta_{front}^2 + \Delta\theta_{rear}^2}\ .$$

The error on the rear angle was given by the coefficients of the covariant matrix from the minimum χ^2 fit of the hits in the rear chambers. This error was in average $\Delta\theta_{rear}$ = 0.5 mrad. The error on the front angle depended on the projection error of the rear track at the magnet center, and the error on the vertex position. The front angle being defined as:

$$\theta_{front} = tg^{-1}\left(\frac{X_{rear} - X_{vertex}}{Z_{mag} - Z_{vertex}}\right),$$

the error was:

$$\Delta\theta_{front} = \left(\frac{1}{Z_{vertex}}\right)\sqrt{(\Delta X_{rear})^2 + (\Delta X_{vertex})^2 + \left(\theta_{front} \times \Delta Z_{vertex}\right)^2}\ .$$

The error on the projection of the rear track at the center of the magnet was given by the covariant matrix coefficients from the minimum χ^2 fit and was in average ΔX_{rear} = 0.09 cm. The error on the X position of the vertex differed whether this position was determined by the beam track or if the vertex was assumed to take place at the target center (see section 4.3-a: Vertex position). The value of this error was then:

ΔX_{vertex} = 0.05 cm if the position of the vertex was given by the beam track

or $= \frac{\text{Target diameter}}{\sqrt{12}}$ =2.9 cm if the beam track information was not used.

The average error on the Z position of the vertex was given by the dimension of the target $\Delta Z_{vertex} = \frac{\text{Target length}}{\sqrt{12}}$ = 9 5 cm. The overall error on the momentum was then given by:

$$\frac{\Delta P}{P} = 1.1 \times 10^{-3}\ (\mathrm{GeV/c})^{-1} \times P \quad \text{using the beam track information,}$$

$$= 6.6 \times 10^{-3}\ (\mathrm{GeV/c})^{-1} \times P \quad \text{without using the beam track information,}$$

where P is in GeV/c.

The minimum momentum for a muon to cross the muon absorber and generate a triple coincidence was 6 GeV/c. The tracks with a calculated momentum lower than 5.5 GeV/c were rejected.

A momentum dependent muon cut was then applied to the track in order to reject the non-muon particles. The error on the position of the track at the μ-1 wall was largely dominated by the multiple scattering. The maximum allowed distance between the track projection and the edge of a hit muon counter was given by $3 \times (\sigma_{mult.scat.})$ where $\sigma_{mult.scat.}$ is the fitted variance of the multiple scattering distribution produced via Monte Carlo.

65% of the events analyzed by the filter program had at least one pair of opposite sign muons. The average track multiplicity for those events was 10. The filter calculated the mass for every combination of opposite sign tracks. The Y information of the track was given by the position of the center of the hit μ-Y counter. If more than one μ-Y counter could be attributed to the track, the program selected the counter that generated the widest angle between the two muons. The μ pair invariant mass was computed with the standard formula:

$$M_{\mu^+\mu^-} = \sqrt{(E_+ + E_-)^2 - (\mathbf{p}_+ + \mathbf{p}_-)^2}$$

$$= \left[m_+^2 + m_-^2 + 2\sqrt{(p_+^2 + m_-^2)(p_+^2 + m_+^2)} - 2p_+p_-\cos(\theta_{open}) \right]^{1/2}$$

where E_+, E_- = energy of the positive and negative μ,

$\mathbf{p}_+$, $\mathbf{p}$ = momentum vector of the muons,

p_+, p_- = amplitude of the momentum of the muons,

$m_+ = m_-$ = mass of the muon

θ_{open} = angle between the two muons.

The mass resolution of the filter was found by processing J/ψ events generated by Monte Carlo . The corresponding mass distribution is shown on figure 4.1.

A typical mass distribution for the real di-μ triggers is shown on figure 4.2. The filter rejected the events that didn't have any pair combination giving a mass higher than 2.5 GeV/c^2. The events accepted by the filter were 30% of the events having an opposite sign pair of μ's, which corresponded to 18% of the initial di-μ triggers. The time per event for the filter analysis was 250 ms on a VAX 780 computer (20 times faster than the main di-μ reconstruction program). If the chamber inefficiencies were neglected, the filter accepted 98.2% of the J/Ψ's (see Section 5.3-a: Filter efficiency).

4.4 Di-μ reconstruction

The events accepted by the filter were then analyzed by the di-μ reconstruction program. Contrary to the filter program which found only tracks in the X-Z projection (2-D tracks) in the back of the analysis magnet, the di-μ reconstruction program made a full reconstruction of the space tracks (3-D tracks) both in the front and in the back of the analysis magnet.

4.4-a Front tracking

The tracks in the front of the magnet were found using the 10 planes of the large angle tracks MWPC, or PC's, and the 9 planes of the front drift chambers. The number of planes was 7 for the X view, 6 for the V view, and 6 for the U view, the U and V wires

Figure 4.1:

Di-μ invariant mass calculated by the filter program on Monte Carlo J/Ψ's

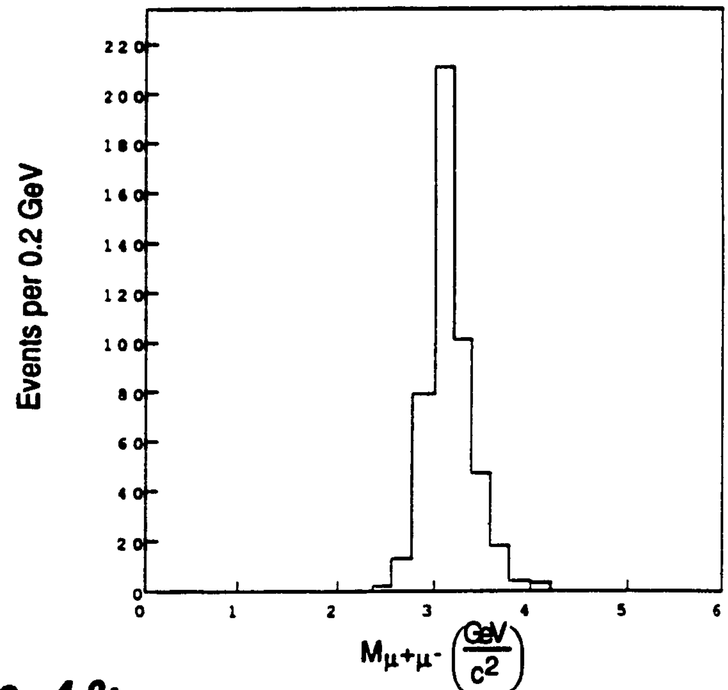

Figure 4.2:

Di-μ invariant mass calculated by the filter program on di-μ triggers

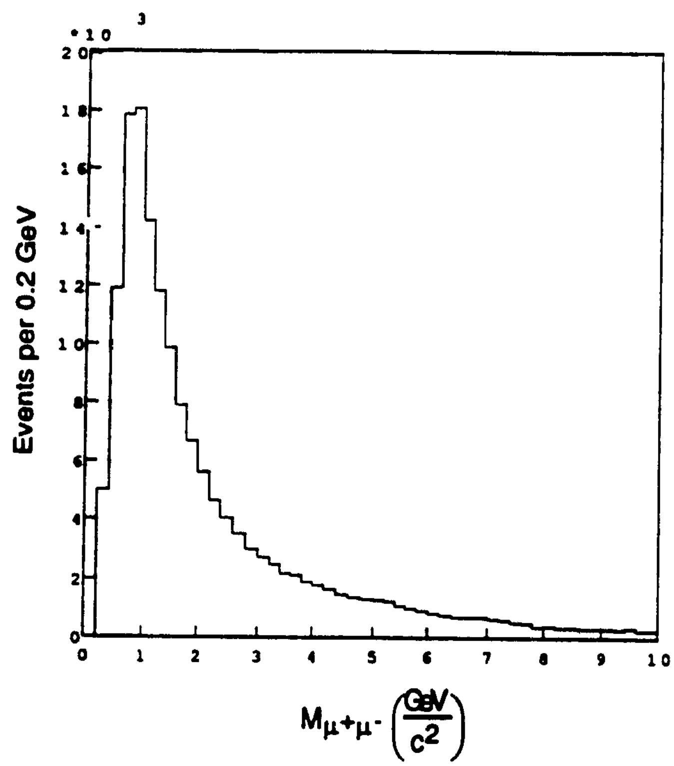

being rotated +16.7 and -16.7°, respectively, with respect to the vertical axis. In the analysis leading to the present work, the PCB information was not used for the front tracking due the limited efficiency of those chambers during the period in which the data was recorded. The technique used for finding the front tracks was first to find the 2-D tracks in each view independently. The views were subsequently combined together to form the 3-D tracks.

For a given view, a line was defined by combining two hits from different chambers. The lines outside the aperture of the magnet were rejected. The lines were also required to point to the target. A line passing outside the target was rejected if its distance of minimum approach to the target edges was larger than 3 cm. A search was made in the remaining chamber planes in order to find hits. The window for the hit search was ±3 mm along the line in order to take into account the chamber resolution. If at least 4 hits were found on the line, a linear fit using the method of least χ^2 was applied to the set of hits found, and the track was accepted if the χ^2 per degree of freedom was smaller than 5. If the χ^2 per degree of freedom was between 5 and 10, the worst hit on the track was rejected and the track was refitted. This process of eliminating the bad hits was repeated until the χ^2 per degree of freedom was lower than 5, or until less than 4 hits remained in which case the track was rejected. If the χ^2 was larger than 10 in the first trial fit, the set of hits was immediately rejected. If two tracks had more than 2 wires in common, the one with the least number of points was rejected; if the two tracks had the same number of points, the one with the worst χ^2 was rejected. The typical number of front tracks found in each view was 20 per event.

The tracks from different views were then combined to form 3-D tracks. The algorithm defined a 3-D line by making the combination between a U track and a V track. A given line was required to be within the aperture of the magnet and to point to the target. The algorithm then looked for a matching segment among the X tracks. To be accepted as a 3-D track, the distance between the projections at the center of the magnet of the U-V line and the X track had to be less than 5 mm, and the difference between the x slopes had to be less than 10 milli-radians. A second pass front tracking was made for the 2-dimensional tracks that were not used in any 3-D track. An "orphan" track from one view was combined with another from a different view to form a 3-D line. A hit search was made in the third view along the 3-D line within a window of ±3 mm. The line was accepted as a 3-D track if at least 2 hits were found in the third view.

The hits of the found 3-D tracks were fitted using the least χ^2 method, and the tracks with a χ^2 per degree of freedom larger than 4 were rejected. If two 3-D tracks had more than 3 wires in common, the one with the least number of points was rejected. If two tracks having more than 3 wires in common had the same number of points, the one with the worst χ^2 was rejected. The average number of front 3-D tracks reconstructed was 12 per event.

4.4-b Vertex

The vertex was found using the front tracks and the beam tracks. The technique used was the method of least χ^2 applied to the whole set of front tracks and one beam track. If no beam track was present, the fitting was performed using the front tracks only. If more than one beam track was present, a vertex was found for each beam track. The vertex that gave the least χ^2 was selected, the χ^2 being defined as:

$$\chi^2 = \sum_{i=1}^{n} \sum_{j=1}^{m} \left(\frac{X^{ij} - X^{i}_{vertex}}{\sigma^{ij}} \right)^2$$

where n = number of views = 2 (X and Y),

m = number of tracks (including the beam track),

σ^{ij} = error on the projection of the track j in the view i,

X^{ij} = projection of the track j in the view i,

and X^{i}_{vertex} = position of the vertex found by the fit in the view i.

The minimisation of the χ^2 was done at first with all the front tracks. Then, to avoid secondary vertex effect, the tracks far from the vertex were removed by applying the following condition:

$$A_j = \sum_{i=1}^{n} \left(\frac{X^{ij} - X^{i}_{vertex}}{\sigma^{ij}} \right)^2 < 30 .$$

where the variables and indices have the same meaning as in the previous formula. The fitting was then repeated using the remaining tracks.

4.4-c Rear tracking

The muon tracks after the analysis magnet were found using the twelve drift chamber planes: 6 planes for the X view, 3 planes for the U view and 3 planes for the V view. The tracking was done in a first step in the X view. The same technique was used here as for the 2-D front tracking. The χ^2 cut was however set to 10 rather than 5. The minimum number of points for the X tracks was 3, with a minimum requirement of 1 hit in each chamber. The average number of rear 2-D tracks found was 10 per event.

The space tracks were found by first defining 3-D lines using X view 2-D tracks for the X information, with the Y information given by two hits taken from the U and V planes. A hit search was made to find hits along the defined 3-D line in the remaining U and V planes with a window of ±3 mm. The 3-D track was accepted if the number of hits, including the hits on the X track, was at least 6. A 3-D fit was applied to the hits found and the track was accepted if the χ^2 per degree of freedom of the fit was lower than 8. The non-muon tracks were rejected by asking the track to point to the μ-1, μ-2, μ-3 and μ-Y counters. The CPX and CPY hodoscopes were also used to reject out of time tracks and to avoid combinatorial background in the drift chambers. If a track projection was outsite a hit counter, it was rejected if its distance to the edge of the nearest counter was larger than:

μ-Y:	12.5 cm
μ-1:	8.8 cm
μ-2:	10.6 cm
μ-3:	13.6 cm
CPX:	0.9 cm
CPY:	2.2 cm

The difference between the CPX and the CPY cut, and between the μ-Y and the μ-1 cut, was due the track projection error, which, because of the geometrical orientation of the rear drift chamber planes, was larger in Y than in X. Finally, since the magnet induced a negligible bending in the Y direction, the rear tracks were required to point to the target in Y. The average number of 3-D rear tracks found was 5.5 per event.

4.4-d Front-rear matching and mass calculation

Matched tracks were defined by the combination of a rear and a front track if the distance between the front and the rear track at the center of the magnet was less than 3 cm in X and 6 cm in Y; since the analysis magnet induced practically no bending in the Y direction, the difference between the front and rear slopes in the Y-Z projection was required to be less than 30 milli-radians. Only 20% of the rear tracks had a match with a front track. The presence of unmatched rear tracks can be explained by one of the following effects:

1)Spurious hit combinations in the rear chambers,

2)Hadrons ($\pi^{\pm}$ and $K^{\pm}$) decaying in flight into $\mu^{\pm}$ and a neutrino,

3)Halo muons, or muons from the interactions (Drell-Yan, J/Ψ), that crossed the central dead region of the front chambers,

4)Tracks for which the front segment was lost due to tracking inefficiencies.

Though the matching criterion was a good requirement to reject tracks belonging to category 1 or 2, some of such tracks still remained among the front-rear matched tracks. It will be seen in the next section (Second pass analysis) that it was possible to apply stronger requirement on the matching or on the track quality (number of hits, χ^2, hodoscope counter residuals), in order to reject spurious tracks or hadronic decays, and still conserve most of the J/Ψ muons.

The front-rear matched tracks constituted the μ track candidates that were used to calculate the di-μ invariant mass; their number was in average 1.1 per event. Their momentum was calculated using the X slope difference between the front tracks and the rear tracks. The invariant mass was calculated using the muon momenta and the opening angle between the two muons in front of the magnet. A mass was calculated for every opposite sign pairs.

4.5 Second pass analysis

The di-μ trigger events accepted by the di-μ reconstruction program were then re-analyzed by a second pass program, whose purpose was to reduce the number of events present in the continuum under the J/Ψ peak by applying the following set of cuts on the muon track candidates:

1) Difference between the front and rear y slopes <15 mrad

2) Distance between front and rear track at the center of the magnet

$\Delta x <$ 0.7 cm

$\Delta y <$ 6.0 cm

3) If the track didn't point to a hit counter, maximum distance between the track and the edge of the nearest hit counter:

μ-Y : 9.5 cm

μ-1 : 5.8 cm

μ-2 : 8.6 cm

μ-3 : 9.7 cm

CPX : 0.90 cm

CPY : 1.25 cm

4) Number of hits on the rear track ≥ 7

5) χ^2 from the fit of the rear track < 8

6) Momentum of the muon < 320 GeV/c.

Those cuts, while rejecting 80% of the background under the J/ψ peak, conserved 90% of the J/Ψ,s (see section 5.6-c: Di-μ reconstruction efficiency). The mass spectrum for the di-μ events that passed those cuts is shown on figure 4.3.

Figure 4.3:

Di-μ invariant mass distribution from the second pass analysis

The curve is a fit to the data described in the next chapter (section 5.6).

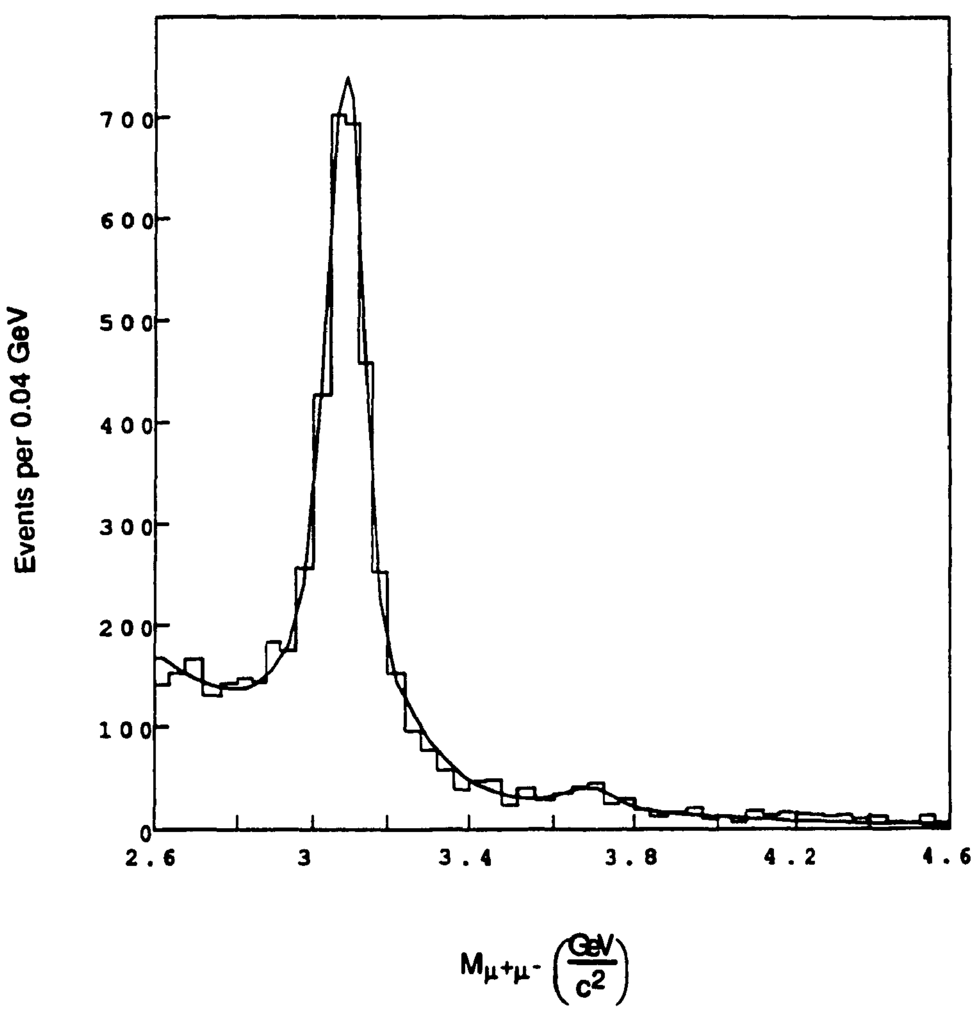

CHAPTER 5

Cross section determination

5.1 Cross section definition

In a subatomic process, the cross section characterizes the transition probability between the initial an the final state of a system of particles. For an initial state consisting of a beam particle hitting a target nucleus, the cross section is given by:

$$\sigma_{i\to f} = \frac{N_f}{N_{beam} \times N_n}$$

where i and f are the initial and the final states,

N_{beam} = number of beam particle hitting the target,

N_n = number of nuclei per target unit surface,

N_f = number of events in the final state f.

In terms of density of the target, the formula becomes:

$$\sigma_{i\to f} = \frac{N_f}{N_{beam}} \times \frac{A}{\delta \times L_{eff} \times N_0} \qquad (5.1)$$

where A = mass number of the target nucleus,

δ = Target density,

L_{eff} = Effective length of the target

$= L_{abs}\left(1 - e^{-(L/L_{abs})}\right)$

where L_{abs} = is the absorption length of the target,

and L is the actual length.

N_0 = Avogadro's number.

The definition 5.1 holds for an ideal case where all the final states are properly reconstructed. It is necessary for a real experiment to include in the calculation the global acceptance ε_{acc}, which include the various factors leading to event loss. The formula then becomes:

$$\sigma_{i\to f} = \frac{N_{observed}}{N_{beam} \times \varepsilon_{acc}} \times \frac{A}{\delta \times L_{eff} \times N_o}.$$

The next part of this chapter is devoted to the counter and the chamber efficiencies. It is followed by a discussion of the global acceptance of the spectrometer. Finally, the cross sections are presented for each beam type used in this experiment, and those results are compared with the measurements from other experiments.

5.2 Counter efficiencies

5.2-a CPX and CPY efficiencies

The CPX and CPY efficiency was found by analyzing photon trigger events. The di-μ trigger events could not be used since the trigger processor required the CPX counters in its algorithm. The efficiency was evaluated by reconstructing the tracks in the photon events using the same algorithm used to find the muons in the di-μ reconstruction program; however the cuts on the scintillation counters were different. The μ-1, 2, 3 and μ-Y cuts were not applied so that all particles were reconstructed. The tracks used for the CPX efficiency were required to point to a lit CPY counter, and reversely, the CPX cut was applied for the CPY efficiency measurement. The tracks used for the efficiency were front-rear matched tracks, to which the following requirement were applied to eliminate fake tracks:

1) Number of hits on the rear segment ≥ 9,

2) χ^2 of the fit of the rear track < 3,

3) Matching distance between front and rear tracks at the magnet center:

$$\Delta x < 1.5 \text{ cm}, \qquad \Delta y < 4.0 \text{ cm},$$

4) Difference between the front and rear y slopes: $\Delta\, slope_y < 0.020$

5) Momentum > 6 GeV/c,

6) Distance between the track projection at the counter wall and the edge of the hole or the edge of the wall:

$$\Delta x < 1 \text{ cm}, \quad \Delta y < 2 \text{ cm}.$$

The tracks were projected to the scintillator plane, which was said to be efficient if the projection intercepted a hit counter, or was at most 1 cm in **x** and 2 cm in **y** distant from the edge of the nearest hit counter. The efficiency was found to be:

CPX: 91.6 ± 0.2 %

CPY: 97.2 ± 0.6 %

where the error is the statistical error. Those efficiencies include track losses due to a ~2mm spacing between adjacent counters. The proportion of hodoscope surface represented by those cracks is ~4% for the CPX, and ~2% for the CPY.

5.2-b μ-Y efficiency

The μ-Y efficiency was evaluated also by analyzing the photon events. First, the triple coincidence, as defined in the di-μ trigger (see Section 2.13-b: Di-μ trigger), were found in the μ-X hodoscopes. Then, the front-rear matched tracks were found in the spectrometer requiring their projection to be far from the central hole, and from the outer limits of the μ-Y wall. To reject the non-muon particles, the tracks were required to point to a triple coincidence. The following supplementary criteria were applied to the tracks to eliminate fake tracks:

1) Number of hits on the rear segment ≥ 9,

2) χ^2 from the fit of the rear track < 3,

3) Matching distance between front and rear tracks at the magnet center:

$$\Delta x < 1.5 \text{ cm}, \qquad \Delta y < 4.0 \text{ cm},$$

4) Difference between the front and rear y slopes: $\Delta\, slope_y < 0.020$

5) Momentum > 10 GeV/c (to avoid tracks with large multiple scattering).

The triple coincidences with more than one track pointing to them were eliminated from the efficiency calculation because of the impossibility to determine which track was the real muon. The μ-Y hodoscope was considered to be efficient if a track trajectory intercepted a hit μ-Y counter within a distance less than the error from multiple scattering. A triple coincidence having a track pointing to it, but without any lit μ-Y counter in its neighborhood was attributed to an inefficiency of a μ-Y counter. Finally, the case where a lit μ-Y counter could be assigned to the triple coincidence, but where the track did not point to the μ-Y counter, was considered as ambiguous; since the track found could be a non-muon charged particle or a spurious track (the muon that generated the triple coincidence having been lost because of finite acceptance or inefficiency in the track reconstruction), this case was not considered in the efficiency calculation. Using this method, the efficiency of the μ-Y counters was found to be .895 ± .006 in average.

5.2-c μ-1, 2, 3 efficiencies

The μ-X (μ-1, μ-2 and μ-3) counter efficiency was also found by analyzing the photon trigger events. The technique used was to first define double coincidences between lit counters in different planes of the muon detector the same way the triple coincidences were defined in the di-μ trigger, but asking only for two rather than three counters aligned together. To avoid as much as possible the ambiguous cases, the counters participating in the double coincidence were required to have their left and right neighbor counter off.

The second step was to reconstruct front-rear matched tracks in the chambers using the same algorithm as in the di-μ reconstruction program; the cuts on the CPX, CPY were the same as for the di-μ reconstruction. The tracks were required to point to a lit μ-Y counter, and to the two counters of a double coincidence in the MUX planes. The cut on the μ-Y, and the two μ-X counters was a momentum dependent cut based on the multiple scattering in the muon detector. The double coincidences with more than one track pointing to them were taken out of the efficiency calculation. The efficiency was defined as the percentage of tracks that, within the multiple scattering, had a lit counter on their path in the third μ-X plane. The tracks intercepting the muon walls near the hole or the outer limits of the wall were eliminated. The following criteria were also applied to the tracks:

1) Momentum > 12 GeV/c (to avoid track with large multiple scattering),
3) Number of hits on the rear segment > 9,
4) The χ^2 per degree of freedom of the fit of the rear track < 4.

The overall plane efficiency was found to be .938 ± .004 for μ-1, .973 ± .003 for μ-2, and .959 ± .004 for μ-3 . Contrary to the μ-2 and μ-3 plane that had overlap between adjacent counters, part of the μ-1 inefficiency was due to a spacing, in average 3.2 mm (1.6% of the width of a μ-1 counter), between adjacent counters. Using the μ-X efficiencies, the di-μ trigger efficiency was evaluated at .766 ± .015.

5.3 Chamber efficiencies

The efficiency of the chambers was evaluated by analyzing the interaction triggers from the alignment tapes (see section 3.3: Calibration). The front-rear matched segments were found in the chambers requiring that the tracks intercepted the live region of all chamber planes. The tracks were also required to have CPX and CPY hits on their trajectories. The following criteria were applied to eliminate fake tracks:

1) x distance between front and rear segment < 1.5 cm,

2) y distance between front and rear segment < 4.0 cm,

3) x slope front-rear matching < 10 mrad,

4) y slope front-rear matching < 20 mrad.

In both proportional and drift chambers, a plane was said to be efficient if the track projection intercepted the cell of a hit wire, or if the projection was less than 2mm distant from the edge of the cell of the nearest hit wire, which distance correspond to 3 x sigma of the track projection error added to the error from the space resolution of the chamber plane under study. The efficiencies found for every chamber plane are listed in table 5.1.

Table 5.1: *Efficiencies for the PC and DC chambers*

Chamber	Plane	Efficiency (%)
PC1	P	66.2
	V	69.8
	X	81.1
	U	74.8
PC2	U	90.9
	X	82.7
	V	93.2
PC3	U	79.7
	X	92.9
	V	86.5
DC1	U	85.9
	X	86.6
	V	88.5
DC2	V	93.0
	X	92.3
	U	89.0
DC3	U	91.3
	X	92.9
	V	91.3
DC4	V	81.9
	X	86.8
	U	82.7
	P	84.2
DC5	P	89.5
	V	89.8
	X	92.8
	U	86.8
DC6	P	82.9
	V	83.1
	X	87.2
	U	82.6

The error on the efficiency values were in average 2.1%, and were mainly due to fluctuations of the chamber efficiencies during the period of data acquisition.

5.4 Acceptance

The total acceptance of the spectrometer (ratio between the number of reconstructed events and the events actually produced) depends upon the kinematical distributions of the process being studied. The first step to determine the acceptance is to produce Monte Carlo events which covers the entire kinematical range of the data. Then, by processing the Monte Carlo events through a simulation of the experiment, a differential acceptance is found for every kinematical region of the data. Knowing the measured kinematical distributions of the real reconstructed events, it is then possible to reconstruct the kinematical distributions of the data as it was physically produced. However, since each kinematical variable represent one dimension in the kinematical space, the number of regions can increase rapidly and require a large statistics.

An alternative technique to find the total acceptance is to produce the Monte Carlo events according to the real kinematical distributions. But since those distributions are not known before the acceptance is found, an initial set of Monte Carlo events is produced using an approximation of the kinematical distributions. The data is then corrected for acceptance, and the Monte Carlo events are reweighted, one dimension at a time, using the found distributions. Since this technique does not account for possible correlations between different variables, the resulting distributions are used to reweight the Monte Carlo events, and the process is repeated until a convergence is reached between two successive iterations.

This last technique was used to evaluate the acceptance of the spectrometer. An exception was made here for the anti-proton data, for which the low statistics of the events recorded (~30 J/Ψ's) did not allow to find the kinematical distributions. To find the acceptance, the kinematical distributions were approximated by using the measured distributions from the E537 and NA3 experiments. The difference in beam energy (125 GeV and 200 GeV) between those two experiments were used to extrapolate to our energy (300 GeV).

The parameters which defined the kinematics of the J/Ψ production were X_f, P_t, θ and φ, where:

$$X_f \text{ (or Feynman X) } \equiv \frac{2 P_{\parallel cm}}{\sqrt{s}} ,$$

where $P_{\parallel cm}$ is the component of the momentum of the J/ψ parallel to the beam (which is assumed parallel to the z axis) and $\sqrt{s}$ is the total energy, both $P_{\parallel cm}$ and $\sqrt{s}$ being defined in the center of mass of the beam-nucleon system;

P_t = Momentum of the J/ψ perpendicular to the z axis;

θ = Decay angle of the J/ψ in the center of mass of the J/Ψ;

φ = Angle between the x axis and the projection of the μ^+ trajectory on the x-y plane.

In the experiment described here, the distributions measured by the experiment NA3 (1) were used to generate the initial set of Monte Carlo events. Once the J/Ψ's (or Ψ') were generated and forced to decay into a μ-pair, the μ's were propagated through the spectrometer. The chamber and counter efficiencies were accounted for by using the results previously derived in this chapter. The background accompanying the J/Ψ decay was simulated by overlapping the Monte Carlo events on real di-μ trigger events. In the muon detector, the two muon triple coincidences that generated the trigger in the real event were replaced by the Monte Carlo μ's. The events were then analyzed by the same algorithm that was used in the di-μ reconstruction program.

As it is the case for most fixed target experiments, the E705 spectrometer acceptance was rather small for negative X_f (~15% of the reconstructed J/Ψ's had $X_f<0$). Since the statistics was limited for this kinematical range, and since most of the published results concerning J/Ψ and Ψ' cross sections are for positive X_f, the acceptances presented in this chapter (and later on the cross sections) cover the positive X_f range only.

The di-μ trigger acceptance was defined as the proportion of events having the two μ tracks crossing the three μ-X (μ-1, 2, 3) walls and generate two triple coincidences in different quadrants as defined in the di-μ trigger (see Section 2.13-b: Di-μ trigger). This acceptance was found to be 45% for the pions, and 46% for the protons and anti-protons. These number do not include the 24% event loss caused by the μ-X counter inefficiencies.

The trigger processor efficiency was determined using Monte Carlo J/Ψ events generated using the kinematical distributions measured by the experiment NA3. Using 100% efficiency for the hodoscope counters and the drift chambers, the efficiency was evaluated to be 0.8 ± 0.1. Approximately half of the event loss in the trigger processor was due to the 2.4 GeV/c^2 mass cut, and the rest to the drift chamber hit selection according to the position of the triple coincidences (see section 2.14: Trigger processor).

The overlap technique was used to evaluate the filter program efficiency. The event loss in the filter was found to be 10%, most of it being due to chamber inefficiency. Using 100% efficiency for the chambers, the filter efficiency was found to be .98 ± .01.

The same technique was employed to evaluate the efficiency of the di-μ reconstruction program. For the events entirely in the live regions of the chambers, the overall reconstruction efficiency was found to be 72%. Considering also the events in the dead region of the chambers, the efficiency decreased to 45%. An additional contribution to the reconstruction efficiency was represented by the set of cuts applied by the second pass program which rejected 9.3% of the J/ψ's reconstructed in the first pass. By including the effect of those cuts, the reconstruction efficiency was found to be 40.8%.

The mass resolution of the experiment was measured by fitting the invariant mass distribution obtained by the di-μ reconstruction program for Monte Carlo di-μ events. The distributions are shown in figure 5.1 for J/Ψ and Ψ' di-μ decays. Each distribution was fitted to a function made of two gaussians:

$$f(M) = e^{-\left(\frac{(M-M_{\Psi})^2}{2\sigma_1^2}\right)} + \frac{1}{C}e^{-\left(\frac{(M-(M_{\Psi}+\delta))^2}{2\sigma_2^2}\right)} \tag{5.2}$$

where M is the di-μ invariant mass, M_{Ψ} is the mass of the decaying J/Ψ or Ψ', σ_1 and σ_2 are the widths of the two gaussians, δ is a term that accounts for a slight asymmetry in the mass peak with respect to M_{Ψ}, and C is a scaling factor between the two gaussians. The shape of the mass distribution was the result of the combined effect of many factors such as the chamber resolution, extra hits (hits attributed to a track that actually belong to an other track), chamber efficiency and the dead regions in the center of the chambers. Contrarily to a single gaussian which fitted poorly the distributions, the double gaussian function represented well the effect of the factors degrading the mass resolution. The parameter obtained by the double gaussian fits are shown in table 5.2.

Figure 5.1: *Di-μ invariant mass for Monte Carlo event*

a) Di-μ mass from J/Ψ decay, b) from Ψ' decay. The curve for each distribution is a fit to a sum of two gaussians, as described in the text.

a)

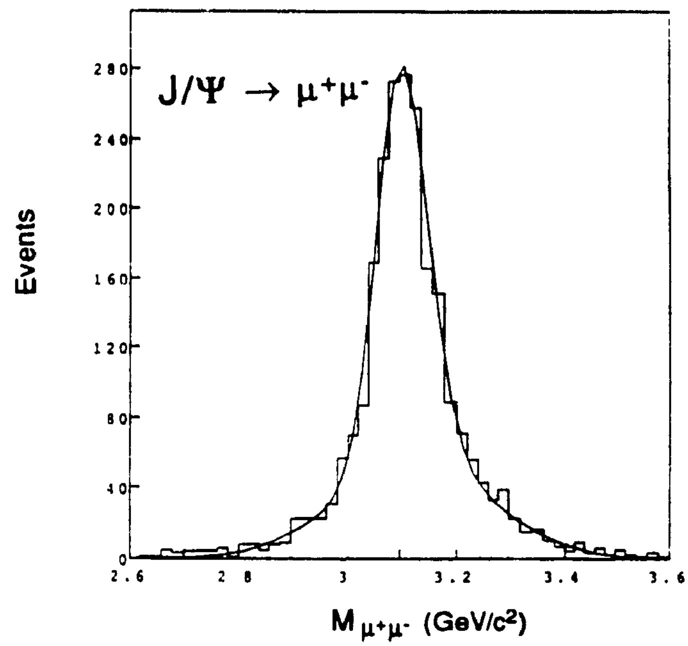

b)

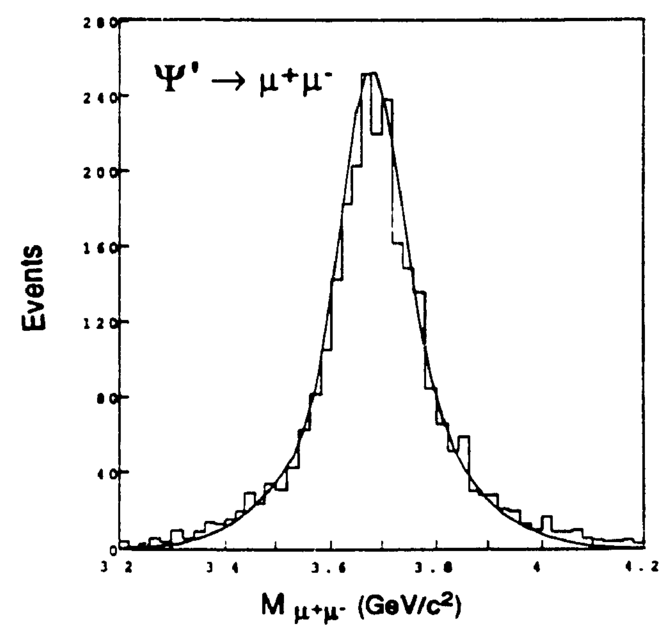

Table 5.2: *Parameters from the fit of the Monte Carlo di-μ mass distributions*

	σ_1(MeV/c)	σ_2(MeV/c)	δ(MeV/c)	C	χ^2/D.O.F
J/Ψ	40 ± 2	138 ± 3	9 ± 4	2.73 ± .04	65/43
Ψ'	60 ± 4	149 ± 5	6 ± 7	2.56 ± .05	90/43

The combined J/Ψ acceptance and efficiency has been found for each beam type as a function of the kinematical parameters X_f, Pt, θ and ϕ, for the positive X_f region. Those distribution are shown on figure 5.2 for the π^- data. The results for each beam type are listed in table 5.3. The ratio between the Ψ' and the J/Ψ total acceptances is for all beams:

$$\frac{Acc_{\Psi'}}{Acc_{J/\Psi}} = 1.15 \pm .03 \ .$$

Those acceptances include the di-μ trigger acceptance, and the various detector and reconstruction efficiencies.

Table 5.3: *J/Ψ acceptances (including efficiencies) for $X_f \geq 0$*

Beam	π^+	π^-	p	$\bar{p}$
Acceptance + efficiencies	.060 ± .012	.060 ± .012	.071 ± .014	.072 ± .014

Figure 5.2: Differential acceptances for the $J/\Psi \rightarrow \mu^+\mu^-$ events from π^-

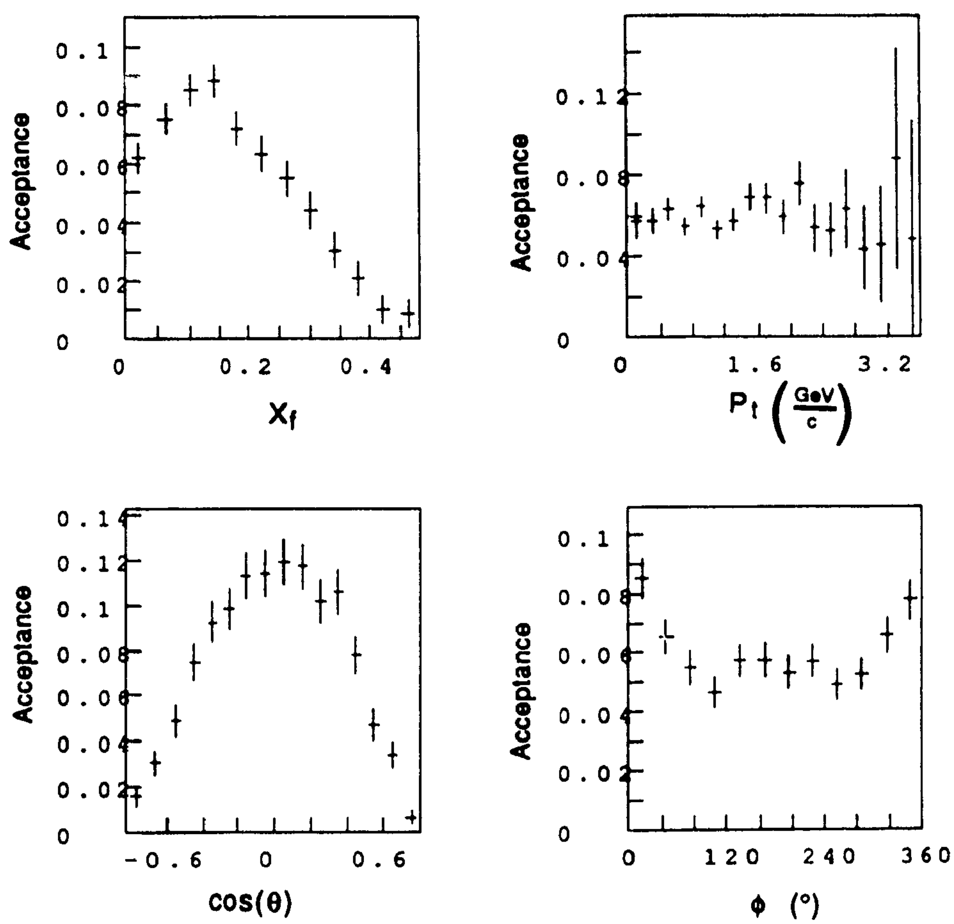

5.5 Beam flux

The beam flux corresponding to the data analyzed (10% of the E705 di-μ data) is listed for the different beam types in table 5.4. Miscountings of the beam scalers at high intensity, due to more than one beam particle being simultaneously present in the beam detector, was corrected for by requiring that the beam rate be linear with the interactions, for which the lower rate allowed to neglect this high intensity effect. This correction was in average 5% for all beam types. The beam flux was also corrected for inefficiencies in the Cerenkov counters (see section 2.2: Cerenkov counters), which caused 0.6% of the π^+ (or π^-) being labeled as protons (or anti-protons).

Table 5.4: *Beam flux*

	π^+	π^-	p	$\bar{p}$
Beam flux	1.79×10^{11}	2.79×10^{11}	2.08×10^{11}	7.30×10^{10}

The error on the fluxes was 2.5% for all beam types, and was mainly due to the uncertainty on the beam miscounting correction.

5.6 Results

The di-μ invariant mass spectrum for each beam type is shown in figures 5.3-a to 5.3-d. The smooth curve is a fit to the data using the double gaussian function 5.2 for the J/Ψ and the Ψ' peaks, added to an exponential background. The exponential shape for the background was found to fit well the mass spectrum outside the J/Ψ and Ψ' peaks. The double gaussian parameters (σ_1, σ_2, δ and C) were fixed to the values obtained in the Monte Carlo simulation described above. The number of J/Ψ and Ψ' events obtained by this fit are listed in table 5.5

Figure 5.3-a: Di-μ invariant mass spectrum

The di-μ mass spectrum is shown for the four beam types used in this experiment. A fit to the data described in the text is shown as a smooth curve The data sample analysed represent 10% of the total E705 data.

$$\pi^+ + N \to J/\Psi + X, \quad J/\Psi \to \mu^+\mu^-$$

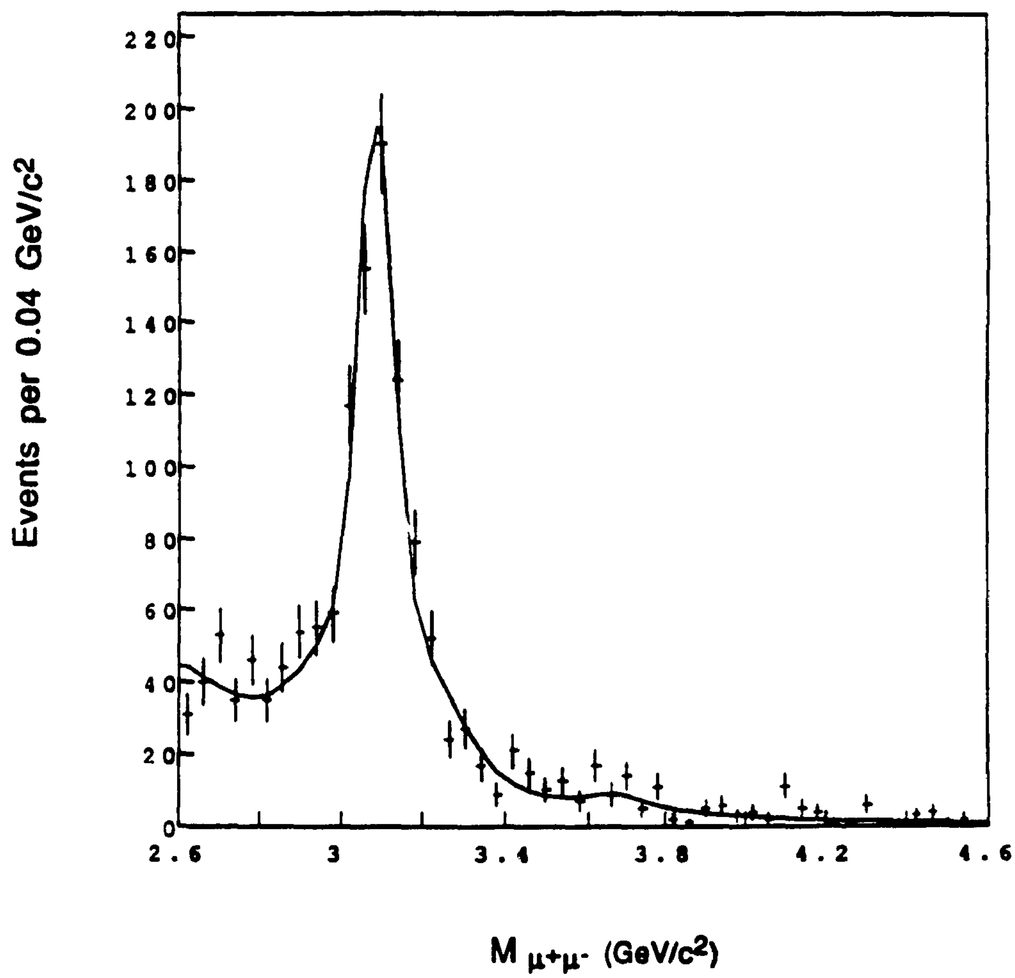

Figure 5.3-b: Di-μ invariant mass spectrum (continued)

$$\pi^- + N \rightarrow J/\Psi + X$$
$$J/\Psi \hookrightarrow \mu^+\mu^-$$

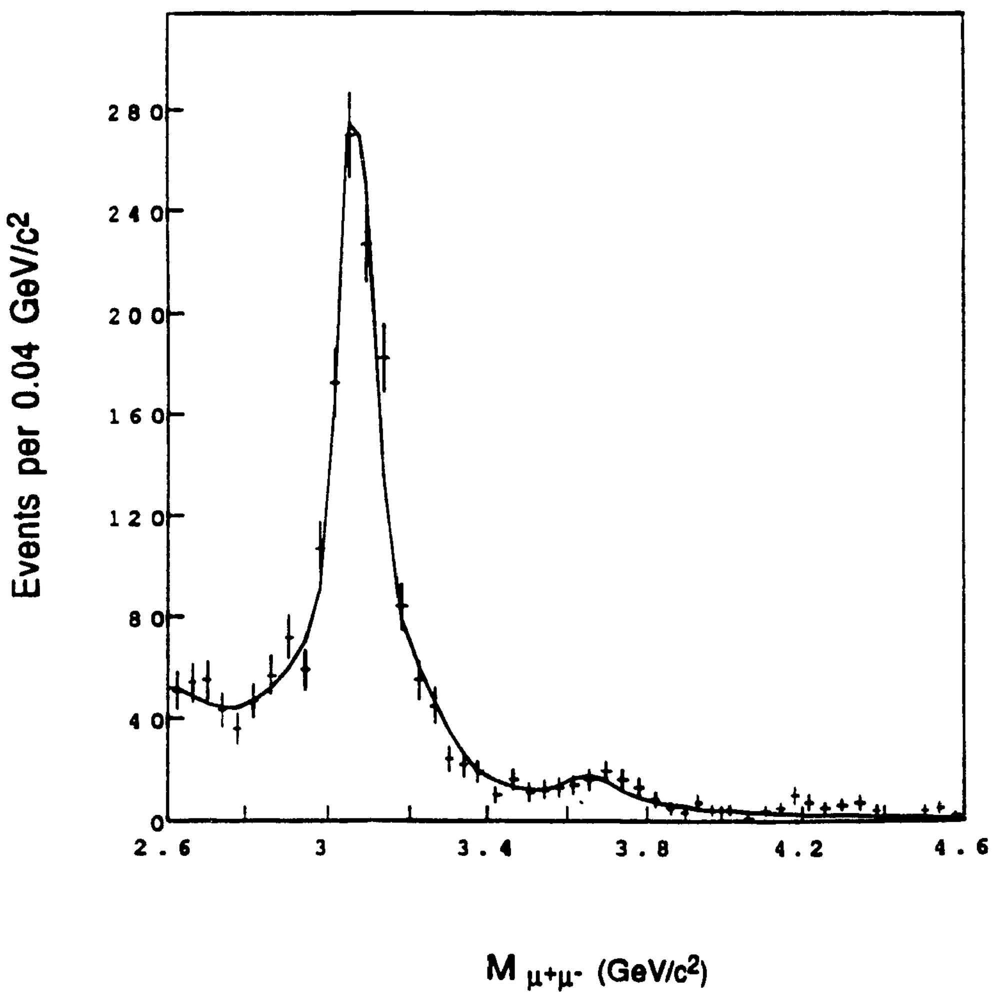

Figure 5.3-c: *Di-μ invariant mass spectrum (continued)*

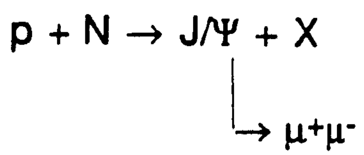

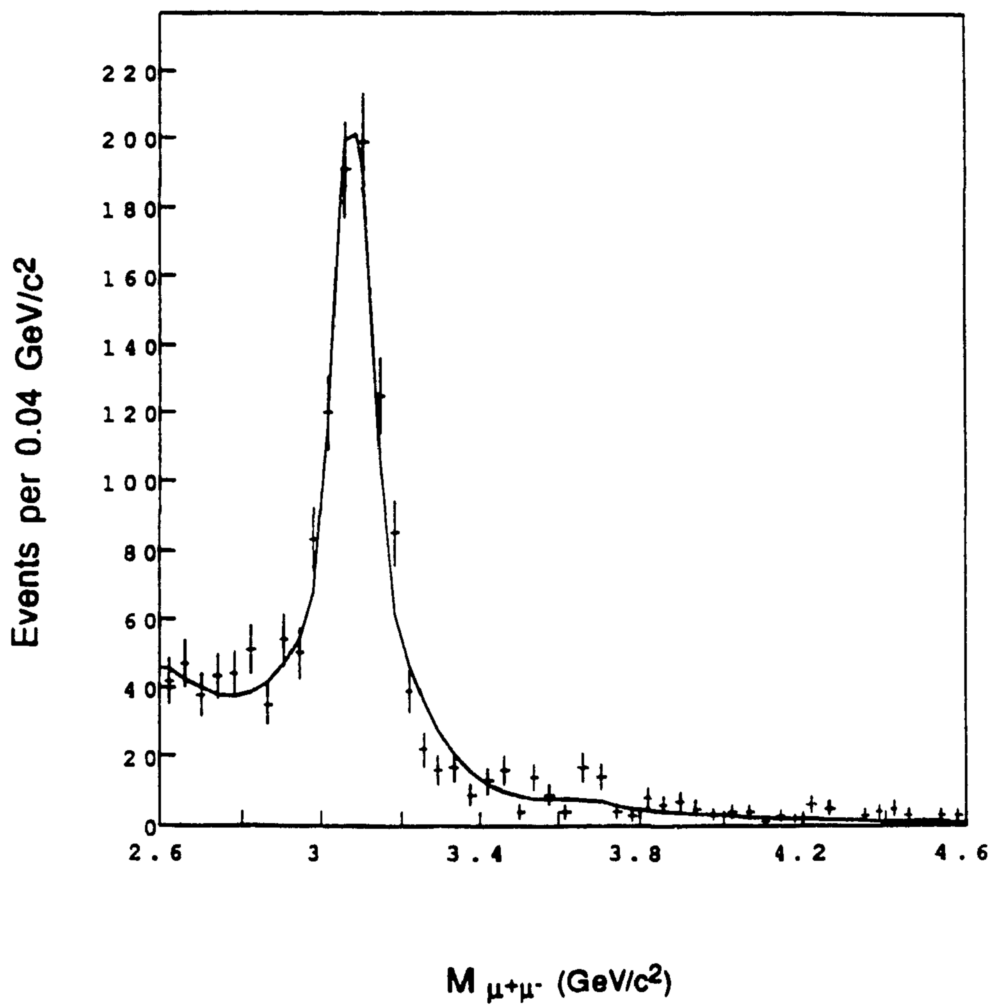

Figure 5.3-d: *Di-μ invariant mass spectrum (continued)*

$$\bar{p} + N \rightarrow J/\Psi + X$$
$$\hookrightarrow \mu^+\mu^-$$

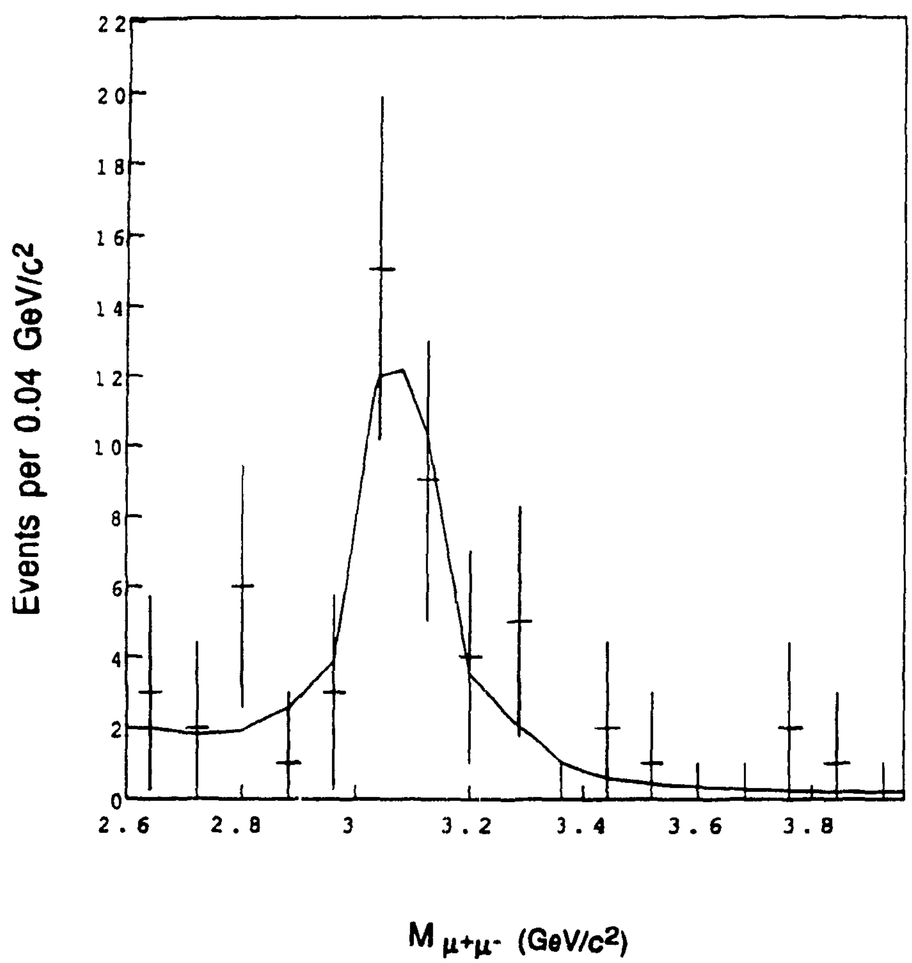

Table 5.5: *Number of J/Ψ and Ψ' events reconstructed*

Beam	J/Ψ	Ψ'
π^+	766 ± 34	22 ± 11
π^-	1103 ± 41	57 ± 13
p	805 ± 35	9 ± 10
$\bar{p}$	27 ± 13	————

The J/Ψ and Ψ' cross sections are listed in table 5.6 for the different beam types used for this experiment. The Ψ' cross section is given in the form of its ratio to the J/Ψ cross section. This way of presenting the Ψ' cross section allows to neglect most of the systematic errors which are the same for Ψ' and J/Ψ.

Table 5.6: *J/Ψ and Ψ' cross sections*

All numbers include the branching ratios for the decay into a pair $\mu^+\mu^-$ (B = 069 ± 0.009 for $J/\Psi \rightarrow \mu^+\mu^-$, and B = 0 0090 ± 0015 for $\Psi' \rightarrow \mu^+\mu^-$). The errors on the J/Ψ cross sections include statistical errors (50% for the anti-proton data and 4% for the other beam types), and the systematic errors (20% for all beam types) The cross section for Ψ' was evaluated for $\pi^\pm$ and protons only because of the lower statistic in the anti-proton data

Beam	B σ (nb/nucleus)	$\frac{B\,\sigma_{\Psi'}}{B\cdot\sigma_{J/\Psi}}$
π^+	51 ± 11	.025 ± 0.013
π^-	46 ± 10	.045 ± .011
p	40 ± 8	.01 ± .01
$\bar{p}$	35 ± 19	————

The values for the J/Ψ cross section are compared with the measurements made by other experiments in figure 5.4. Those measurements are listed in table 5.7, for the different beam types, beam momenta and target materials (the reader can refer to section 1.3 for a description of each experiment). The values listed in table 5.7 are the cross sections per nucleus, which are converted to cross section per nucleon in figure 5.4 for purpose of comparison. The A dependance used for this conversion is:

$$\sigma/\text{nucleon} = \frac{\sigma/\text{nucleus}}{A^{\alpha}} ,$$

where α = .93 ± .01, from a collection of world data compiled by L.Lyons (22). All measurements used to compare with our data were made for $X_f > 0$, exception made for the CS experiment, for which the measurement was made for the entire X_f range.

Table 5.7: *J/Ψ cross sections from $\pi^{\pm}$,p and $\bar{p}$ in other experiments*

All measurements include the branching ratio B $(J/\Psi \rightarrow \mu^+\mu^-)$ = 069 ± 009
Unless otherwise specified, the measurement were made for $X_f > 0$ only

Experiment	$P_{inc}(\frac{GeV}{c})$	Target	Beam	$B\,\sigma(\frac{nb}{nucleus})$, $X_f > 0$
E537[13]	125	Be	π^-	41 ± 4
			$\bar{p}$	34.2 ± 3.4
		Cu	π^-	267 ± 24
			$\bar{p}$	209 ± 21
		W	π^-	585 ± 40
			$\bar{p}$	510 ± 37
NA3[14]	150	H	π^+	6.2 ± 1 0
			π^-	6.5 ± 0.9
			$\bar{p}$	6.6 ± 1.0
		Pt	π^+	969 ± 160
			π^-	884 ± 130
			p	371 ± 90
			$\bar{p}$	800 ± 130
	200	H	π^+	5.8 ± 0.8
			π^-	6.3 ± 0.8
			p	3.6 ± 0.9
		Pt	π^+	976 ± 150
			π^-	960 ± 150
			p	509 ± 130
			$\bar{p}$	730 ± 150
	280	H	π^-	8.7 ± 0.8
		Pt	π^-	1270 ± 120
CIP [12]	225	C	π^+	82 ± 12
			π^-	88 ± 12
			p	53 ± 7
			$\bar{p}$	85 ± 40
CP [19]	225	C	π^+	122 ± 26
			π^-	141 ± 24
			p	82 ± 12
CS [21]	400	Fe	p	20 ± 4 , all X_f

Figure 5.4: E705 J/Ψ cross section compared with existing data

The cross sections plotted refer to the value listed in table 5.5 and 5.6. All cross sections are given per nucleon, using the parametrisation σ/nucleon = $\frac{\sigma/\text{nucleus}}{A^{\alpha}}$, where α = 93 ± 0! The value on the horizontal axis is $\sqrt{\tau} = \frac{M_{J/\Psi}}{\sqrt{s}}$, where $\sqrt{s}$ is the center of mass energy in the beam-nucleon system. The cross sections include the branching ratios for the decay into a pair $\mu^+\mu^-$ (B = .069 ± 0.009).

a) $\pi+\ N \rightarrow J/\Psi + X$

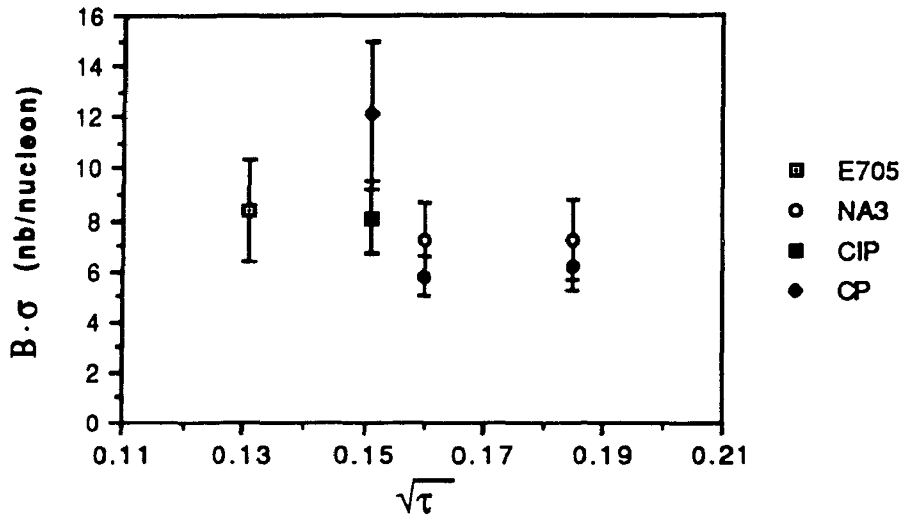

b) $\pi-\ + N \rightarrow J/\Psi + X$

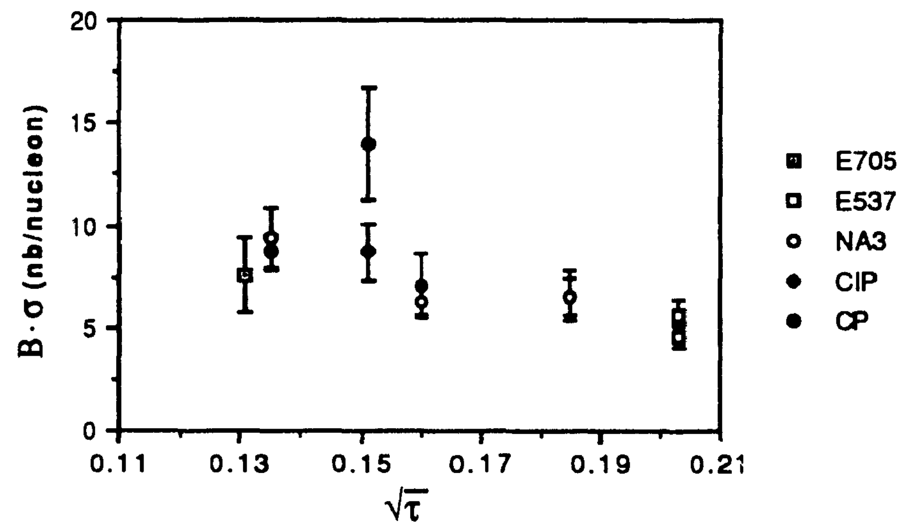

Figure 5.4: *E705 J/Ψ cross section compared with existing data (continued)*

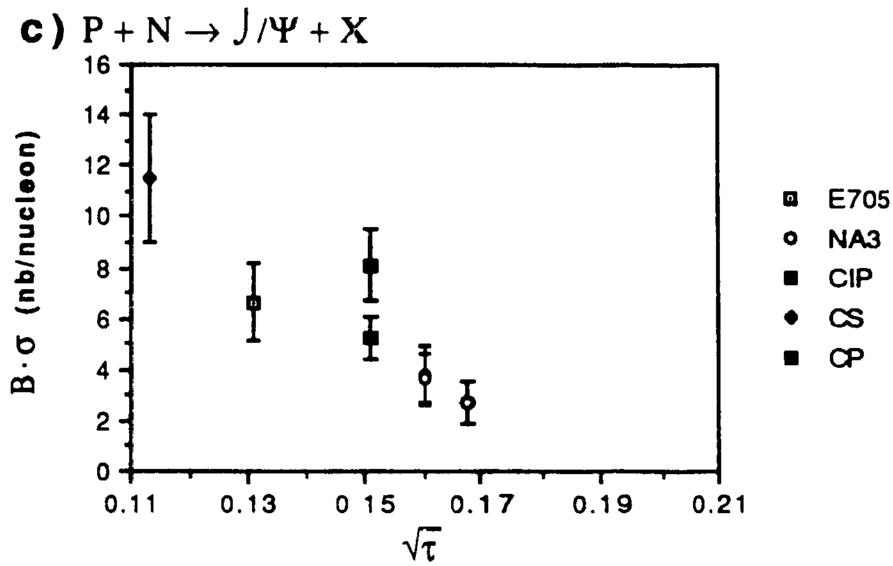

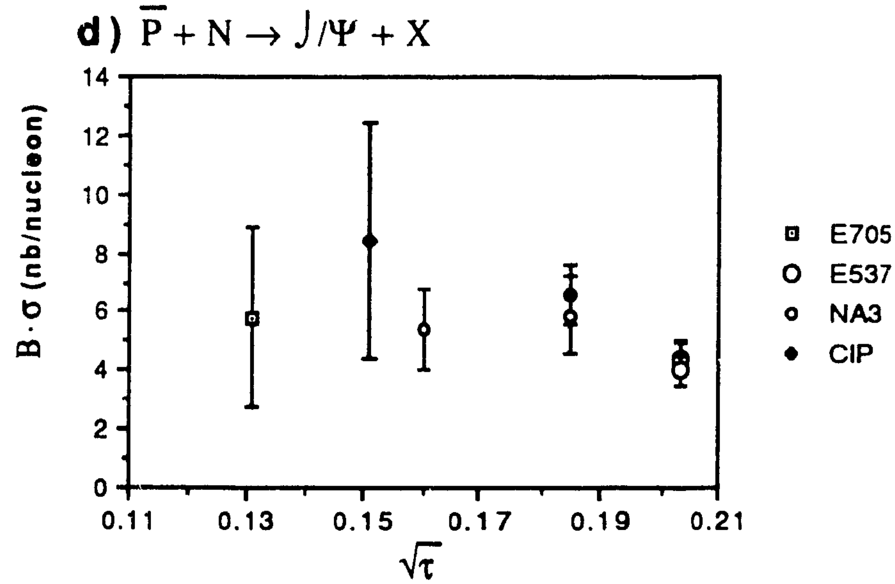

The measurement was converted to $X_f > 0$ by assuming a symmetrical distribution centered on $X_f = 0$ (see (21)).

The Ψ' to J/Ψ cross section ratios are compared with the ratios measured by other experiments in figure 5 5 The measurements used to compare with our data are listed in table 5 8. The Ω E537, CP and CIP measurements were made for $X_f > 0$ only while the WA11 and CFS cross sections were measured for all X_f The CFS and the ISR experiments detected J/Ψ and Ψ' through their decay into e^+e^-, while all other experiments detected the μ pairs The ISR experiment, by analyzing indistinctly events coming from samples at two different energies (52 and 63 GeV), measured the quantity $\left(\frac{d\sigma}{dy}\right)_{y=0}$ for both J/Ψ and Ψ', where y is the rapidity[1].

Table 5.8 *Ψ' to J/Ψ cross section ratios measured by other experiments*

The cross sections include the branching ratios for leptonic decay B = 069 ± 0 009 for $J/\Psi \to \mu^+\mu^-$ and $J/\Psi \to e^+e^-$, and B = 0 0090 ± .0015 for $\Psi' \to \mu^+\mu^-$ and $\Psi' \to e^+e^-$

			$B\,\sigma(\Psi')/B\,\sigma(J/\Psi)$		
Experiment	$\sqrt{s}$ (GeV)	target	π^+	π^-	p
Ω (11)	8.6	W	.031 ± .006	037± .013	
WA11 (20)	16.8	Be	.020 ± .004		
E537 (13)	15.3	W	.029 ± 004		
CP (19)	20.6	C		.018 ± .007	.007 ± .004
CIP (12)	20.6	C	.021 ± .006	.017 ± .009	.016 ± .009
CFS (23)	27.4	Be			.017 ± .005
ISR (24)	52 & 63	p			.019 ± .006

1 $y = \tanh^{-1}(p_z/E)$, p_z and E are measured in the center of mass of the interaction

Figure 5.5: *E705 Ψ' to J/Ψ ratio compared with existing data*

The cross sections plotted refer to the value listed in table 5.5 and 5 7. The value on the horizontal axis is $\sqrt{\tau} = \frac{M_{J/\Psi}}{\sqrt{s}}$, where $\sqrt{s}$ is the center of mass energy in the beam-nucleon system. The cross sections include the branching ratios for the decay into a lepton pair (B = .069 ± 0.009 for $J/\Psi \to l^+l^-$, and B = 0.0090 ± .0015 for $\Psi' \to l^+l^-$).

a) π+

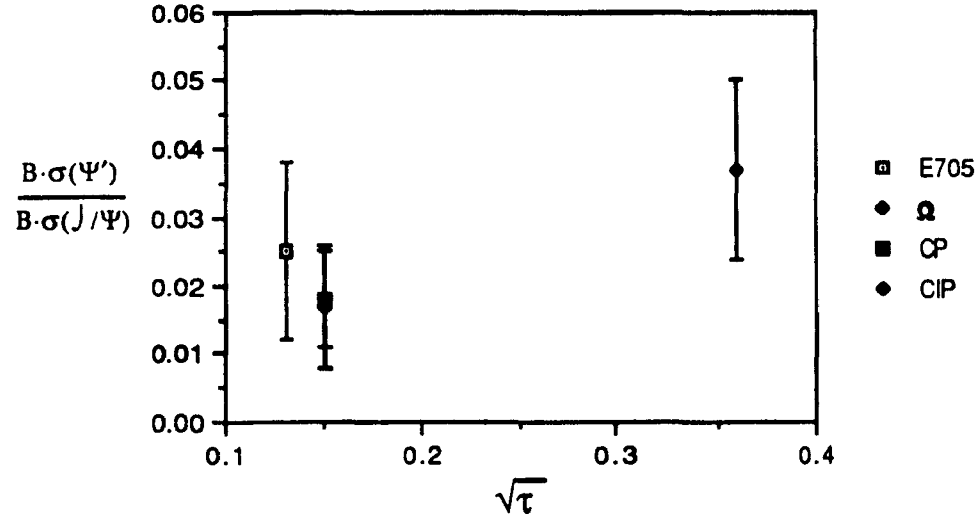

b) π−

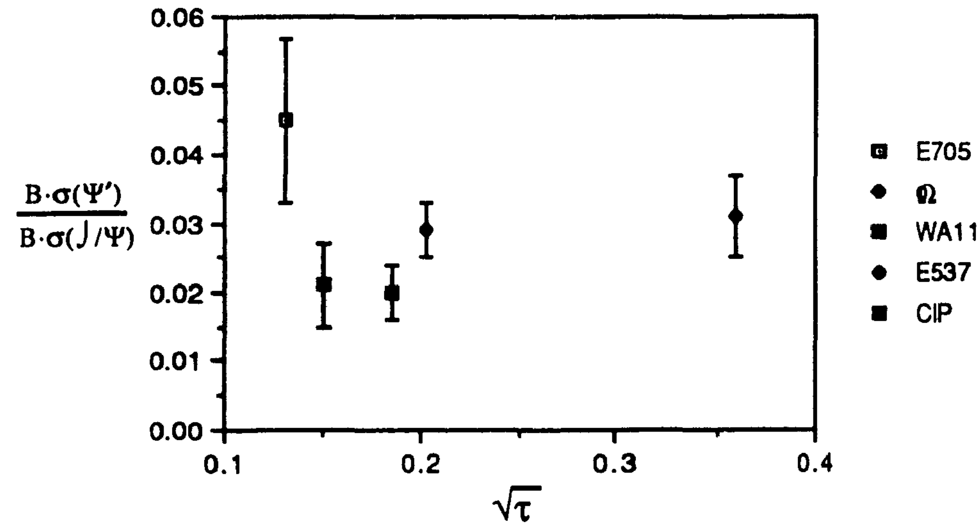

Figure 5.5: E705 Ψ' to J/Ψ ratio compared with existing data (continued)

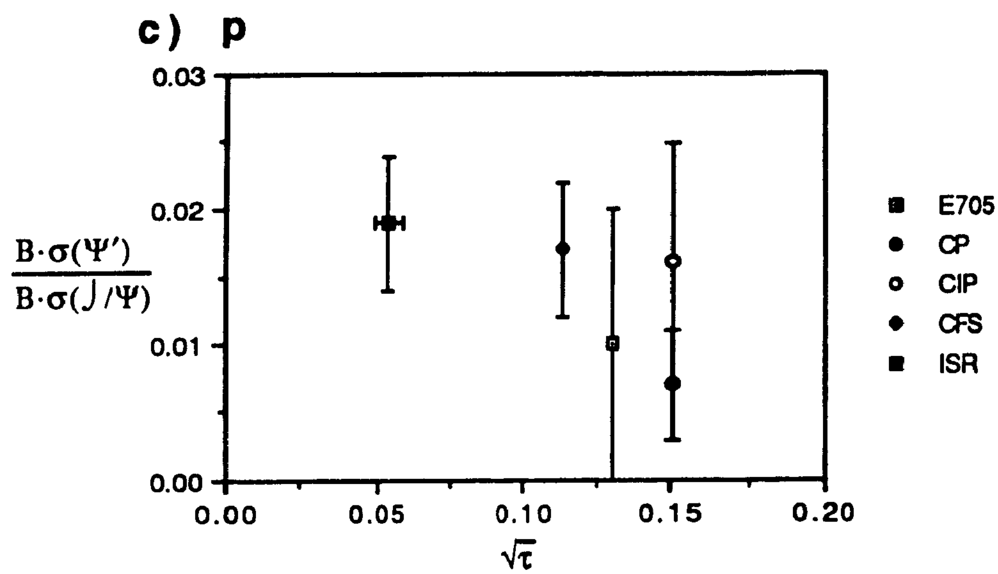

The differential cross sections $d\sigma/dX_f$ are shown for $\pi^\pm$ and p beams in figure 5.6-a to 5.6 c. The solid line in this figure is the result of a fit of the distribution using a function in the form $(1-X_f)^\beta$. The parameters of the fits are listed in table 5.9.

Table 5.9: *Parameters from the fit of the X_f distributions*

	β	χ^2/D.O.F
π^+	3.4 ± .4	14/10
π^-	2.6 ± .3	28/10
p	5.5 ± .4	21/9

A parametrisation of the form:

$$\sigma(X_f) = A^\alpha\left(\frac{Z}{A}\sigma_h(X_f) + \frac{A-Z}{A}\sigma_{h'}(X_f)\right) + A^\beta\,\sigma_d(X_f)$$

where A = Number of nucleons in the target nucleus,
Z = Number of protons in the target nucleus,
α, β = Exponent of the nuclear effect for the hard and diffractive processes,
σ_h, $\sigma_{h'}$ = Hard cross section distribution for a proton and a neutron target,
σ_d = Diffractive cross section distribution,

was made by Badier et al.(NA3)(14) in order to estimate the A dependance of the J/Ψ cross section in function of X_f. The quantities α, β, σ_h, $\sigma_{h'}$ and σ_d were measured by the experiment NA3 at 200 GeV/c for π^+ and p beams, and at 150 and 280 GeV/c for π^- beam. Using this formula, the X_f distributions were calculated for a lithium target. The resulting distributions are superimposed to the E705 measurement in figure 5.6. The X_f distribution for 400 GeV/c p beam on Fe target measured by the CS collaboration (21) is also shown in figure 5.6-c. Both NA3 and CS distributions are normalized to the E705 data.

Figure 5.6-a: *X_f distributions*

The X_f distributions are shown for $\pi^{\pm}$ and p beams. The smooth curve is a fit to our data (described in the text). Also shown are the distributions measured by the experiment NA3 at 200 GeV/c for π^+ and p beams, at 150 and 280 GeV/c for π^- beam, and from the experiment CS at 400 GeV/c for p beam, the distributions from both experiment being normalized to the E705 distributions.

$$\pi^+ + N \rightarrow J/\Psi + X, \quad J/\Psi \rightarrow \mu^+\mu^-$$

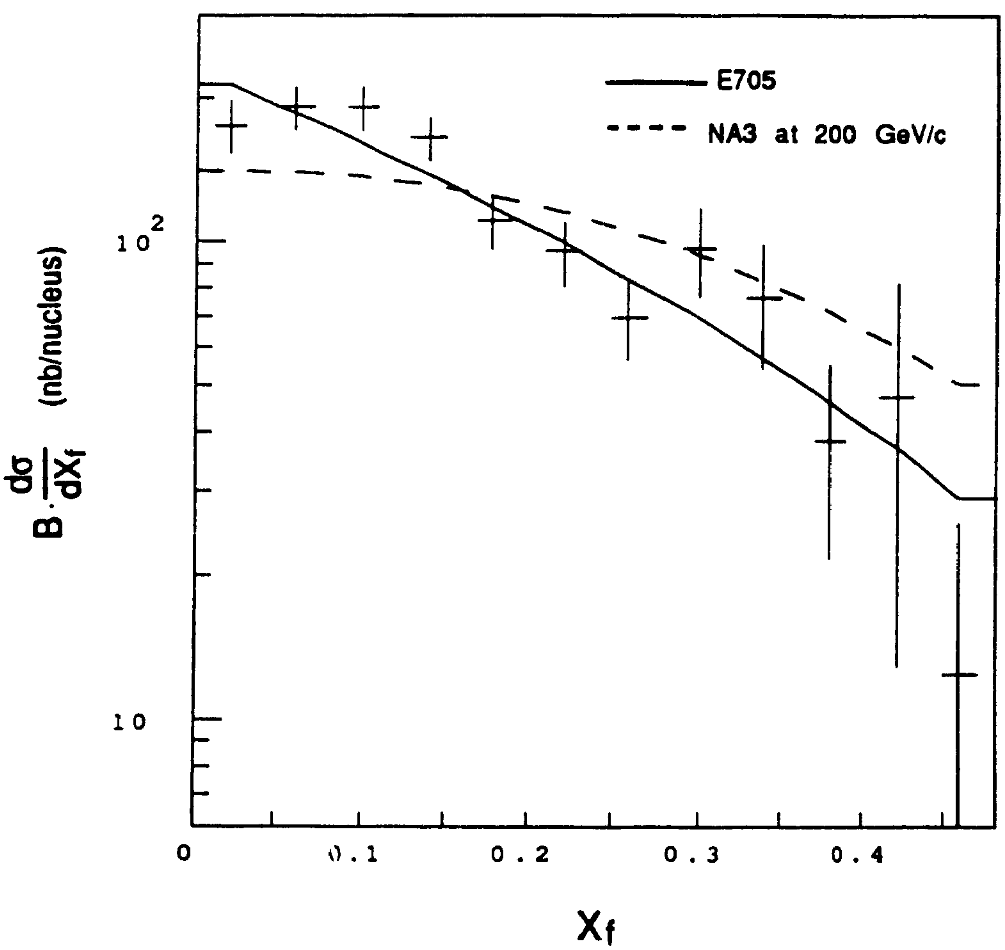

Figure 5.6-b: *X_f distributions (continued)*

$$\pi^- + N \to J/\Psi + X$$
$$\hookrightarrow \mu^+\mu^-$$

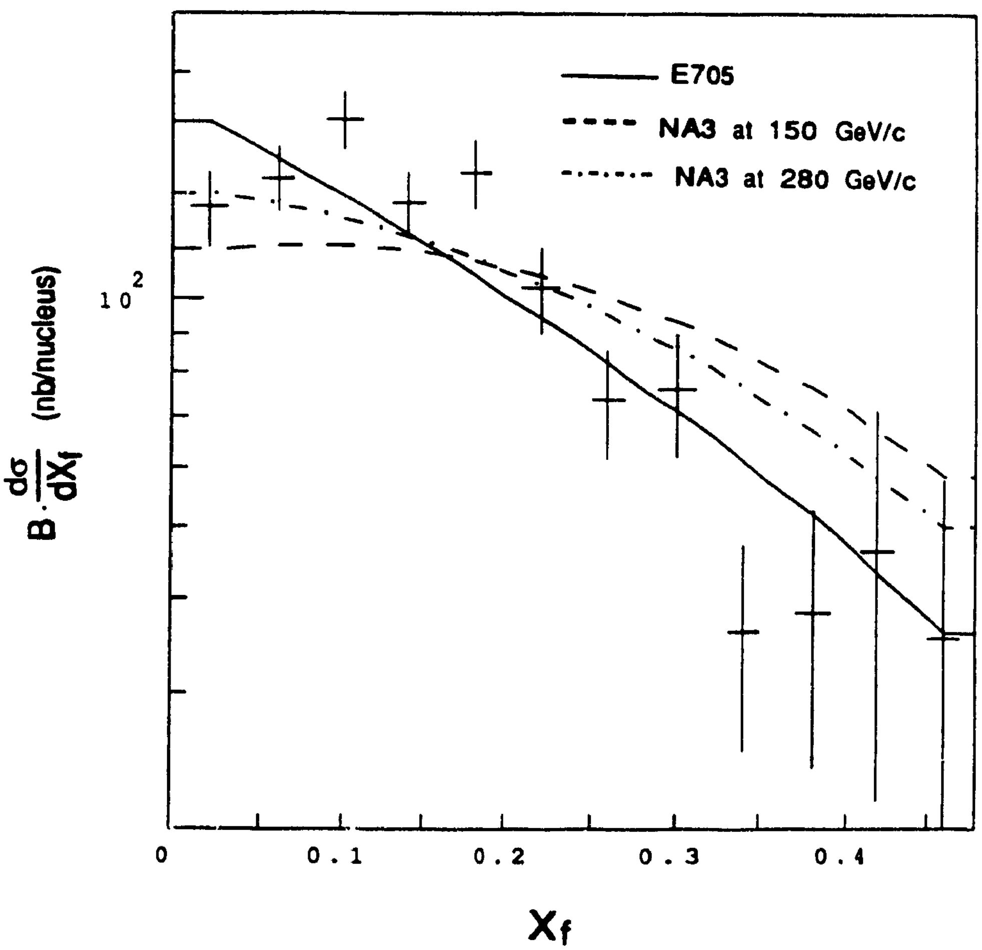

Figure 5.6-c: *X_f distributions (continued)*

$$p + N \rightarrow J/\Psi + X$$
$$\quad\quad\quad\quad\quad \hookrightarrow \mu^+\mu^-$$

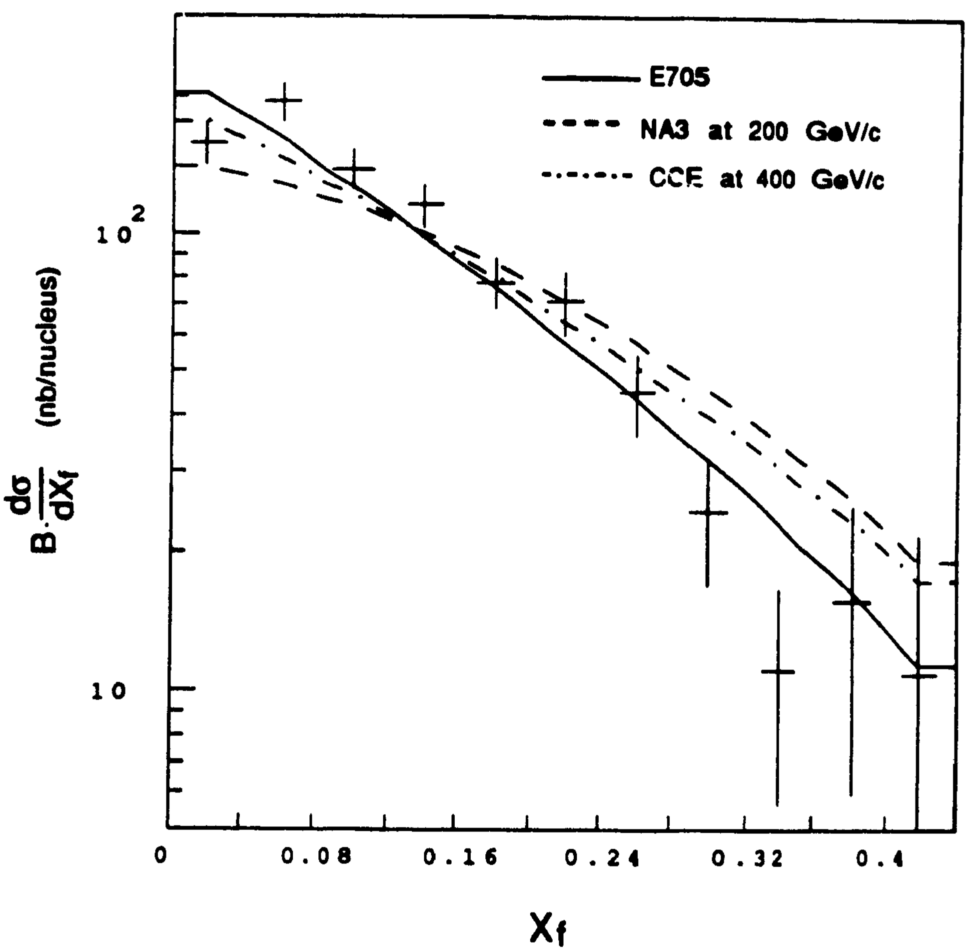

The P_t distributions are shown in figure 5.7. The distributions are fitted to a function in the form $d\sigma/dP_t \sim Pt \cdot \left(1 - \frac{P_t^2}{A^2}\right)^B$, and the parameters from the fit are shown in table 5.10. The distributions measured by the experiment NA3 using a hydrogen target, at 200 GeV/c for π^+ and p beams, and at 280 for π^- beam, were normalized to the E705 data and superimposed on the E705 distributions.

Table 5.10: *Parameters from the fit of the P_t distributions*

	A	B	χ^2/D.O.F
π^+	2.5 ± .6	-5.1 ± 1.9	6/17
π^-	1.7 ± .3	-3.7 ± .8	11/17
p	5.1 ± 2.7	-19 ± 18	17/17

The cos θ distributions are shown in figure 5.8-a to 5.8-c. By analogy with the distribution measured by experiment NA3 (14) using 280 GeV/c π^- beam, the E705 distributions were fitted to the function:

$$\frac{d\sigma}{d\cos\theta} \sim 1 + \alpha \cos^2\theta \ .$$

The values of α extracted from the fits are shown in table 5.11. Those measurements can be compared with the values (14) $\alpha = -0.20 \pm 0.06$ for hydrogen target, and $\alpha = -0.31 \pm 0.02$ for platinium, obtained by experiment NA3. A fit from NA3 cos θ distribution for hydrogen target is also shown in figure 5.8-b. The quoted errors on the NA3 α measurements are statistical only; the systematic error, due to small aceptance near $|\cos\theta| = 1$, was estimated by this experiment to be of the order of 0.1 . The E705 measurement of α for π^- beam lead to a difference of 1.9 sigma with the value measured

Figure 5.7-a: *P_t distributions*

The P_t distributions, corrected for acceptance, are shown for $\pi^{\pm}$ and p beams. The smooth curve is a fit to our data (described in the text). Also shown are the distributions measured by the experiment NA3 at 200 GeV/c for π^+ and p beams, at 280 GeV/c for π^- beam, normalized to the E705 distributions.

$$\pi^+ + N \rightarrow J/\Psi + X$$
$$J/\Psi \rightarrow \mu^+\mu^-$$

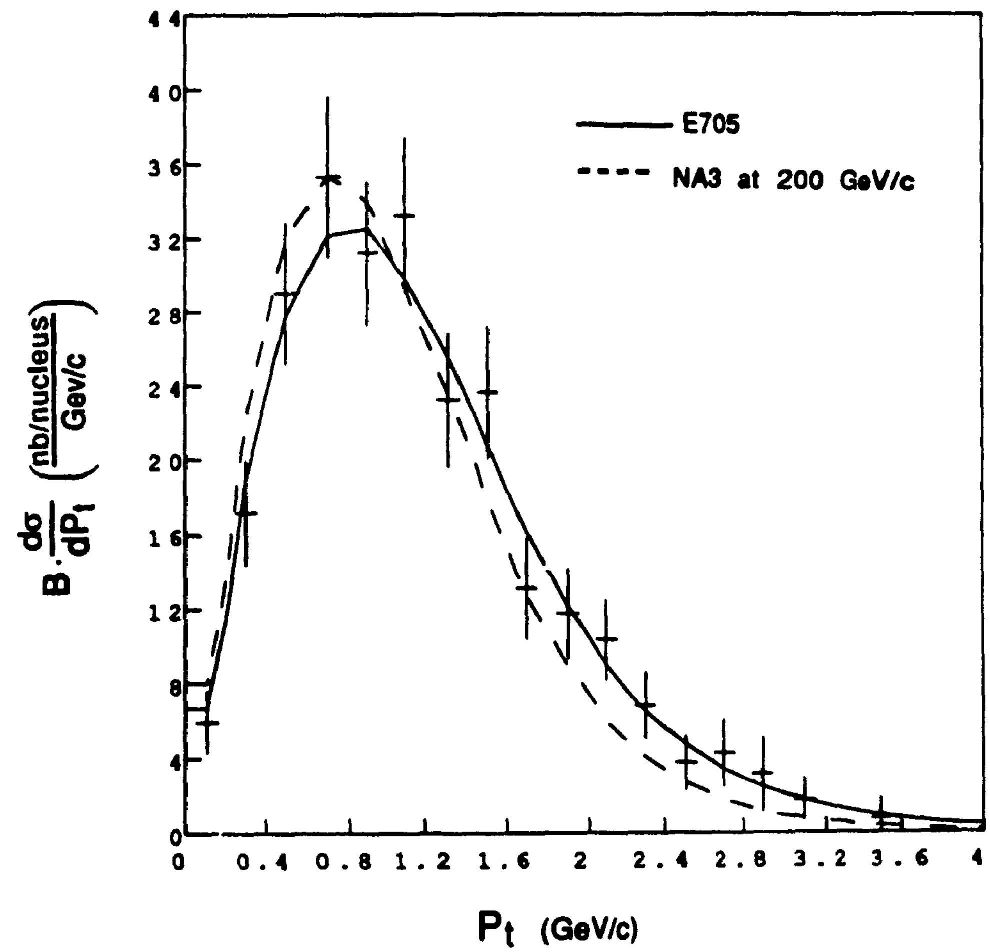

Figure 5.7-b: *P_t distributions (continued)*

$$\pi^- + N \rightarrow J/\Psi + X$$
$$\hookrightarrow \mu^+\mu^-$$

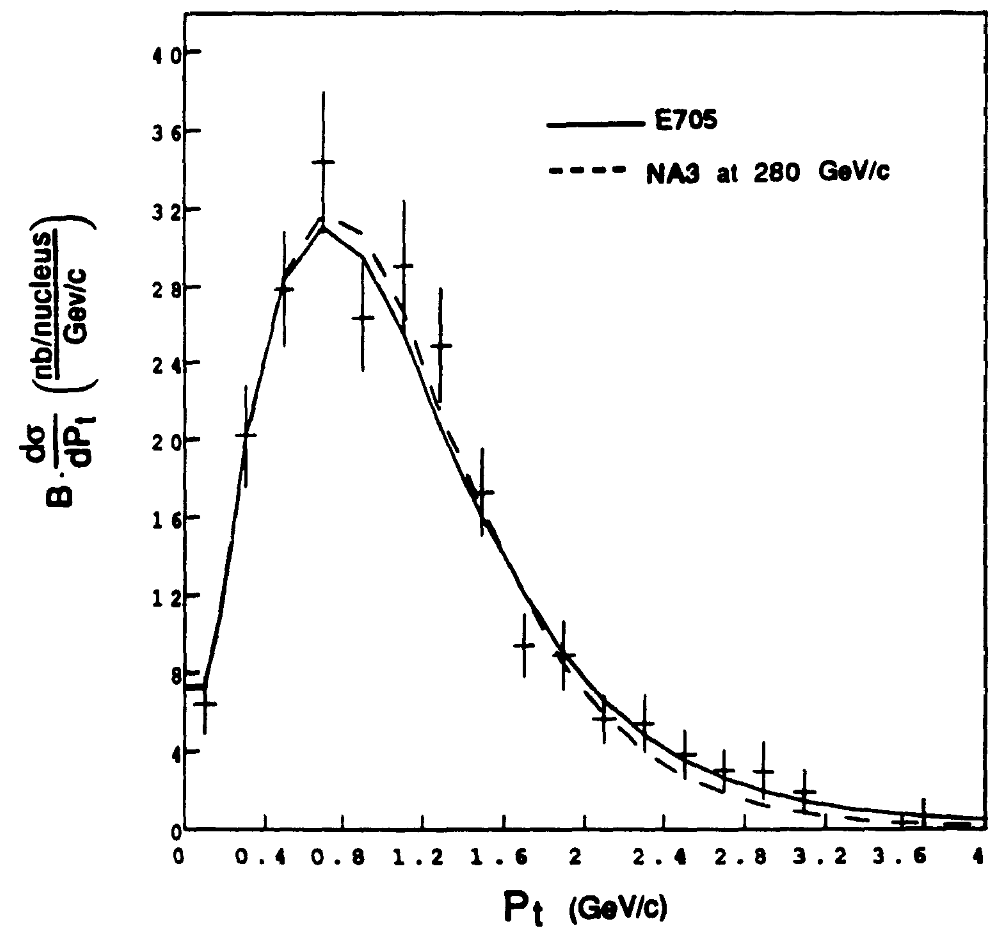

Figure 5.7-c: *P_t distributions (continued)*

$$p + N \rightarrow J/\Psi + X$$
$$\hookrightarrow \mu^+\mu^-$$

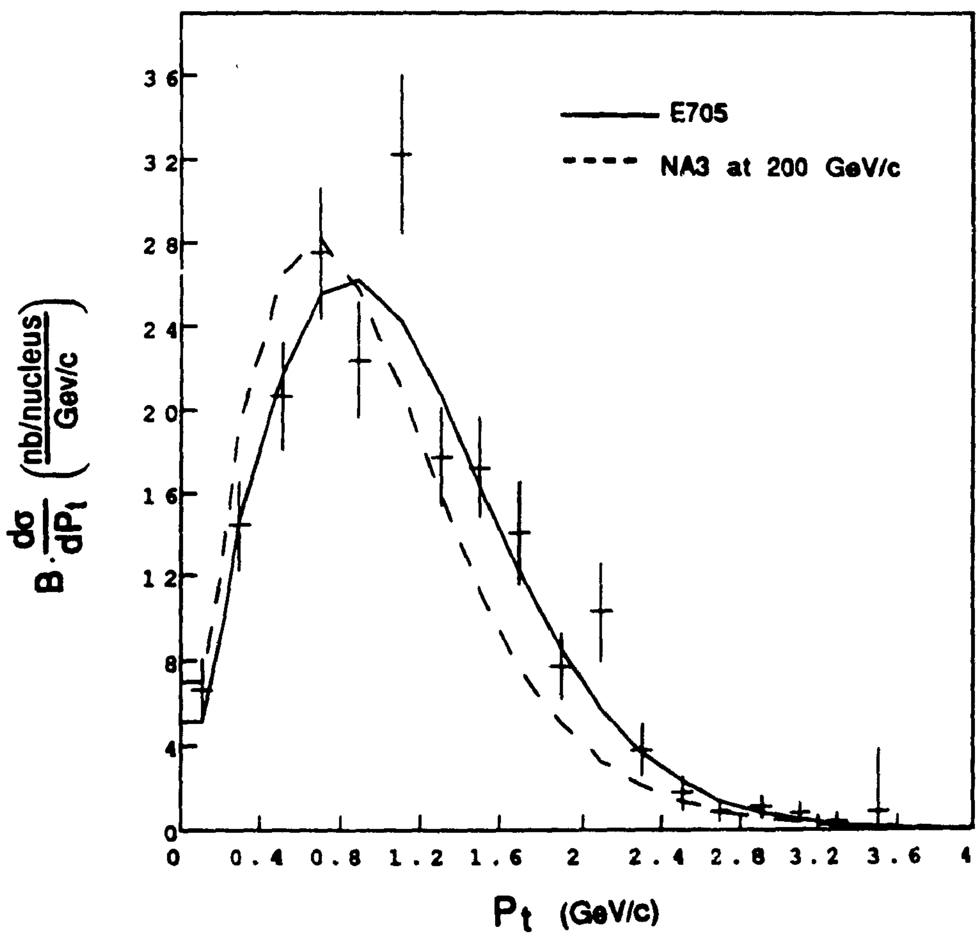

Figure 5.8-a: Cos(θ) distributions

The cos(θ) distributions, corrected for acceptance, are shown for $\pi^{\pm}$ and p beams. The smooth curve is a fit to our data (described in the text). Also shown in figure 5.8-b is the distribution measured by experiment NA3 at 280 GeV on hydrogen target, normalized to the E705 distribution.

$$\pi^+ + N \rightarrow J/\Psi + X$$
$$\hookrightarrow \mu^+\mu^-$$

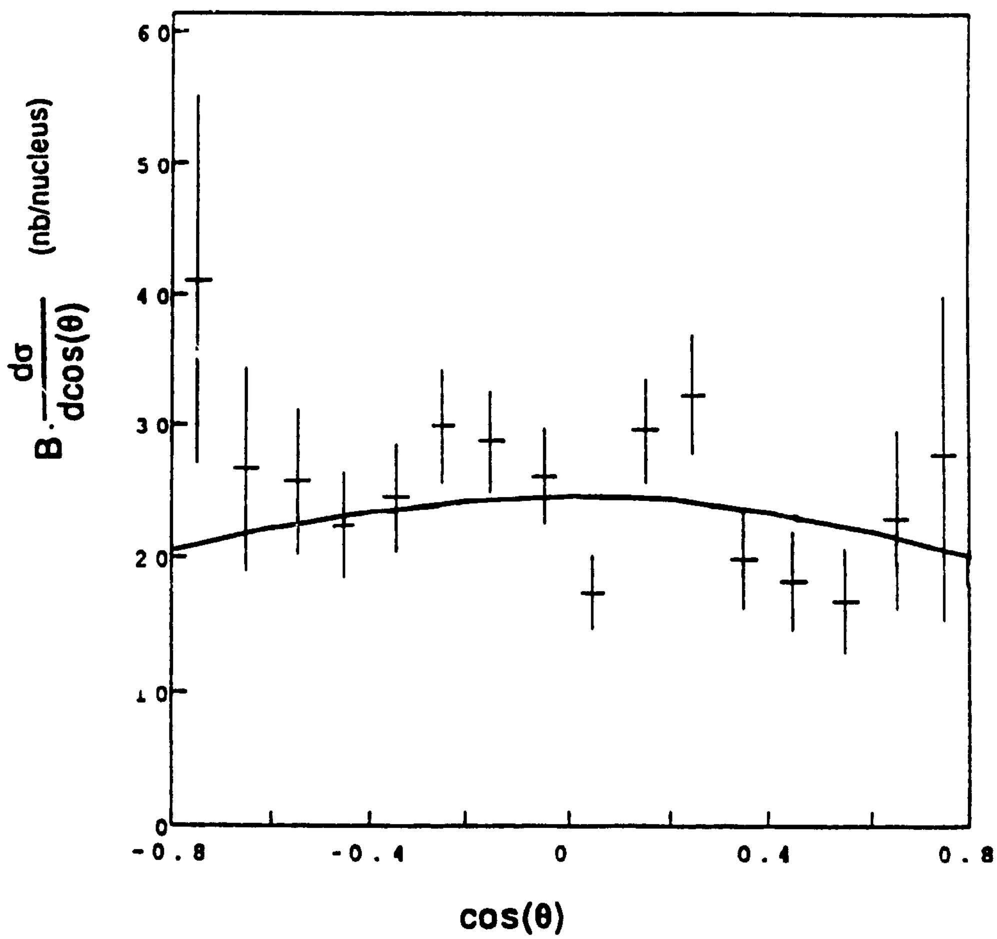

Figure 5.8-b: Cos(θ) distributions (continued)

$$\pi^- + N \rightarrow J/\Psi + X$$
$$\hookrightarrow \mu^+\mu^-$$

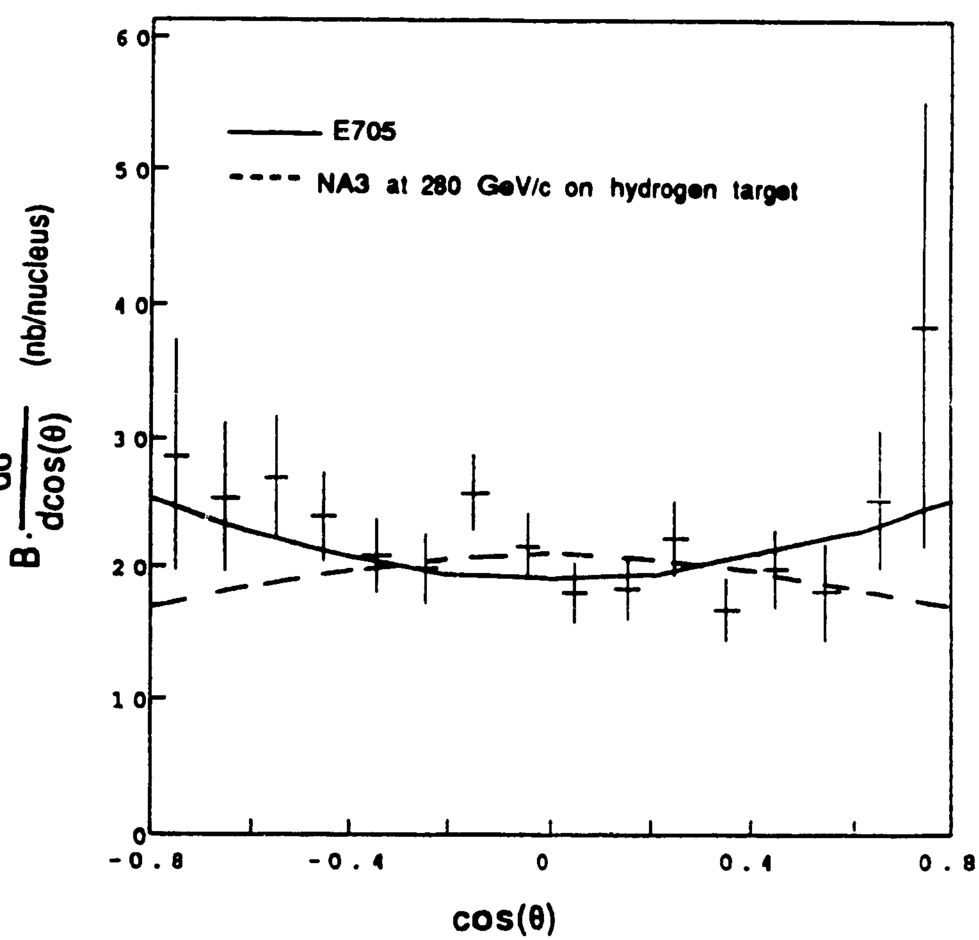

Figure 5.8-c: *Cos(θ) distributions (continued)*

$$p + N \rightarrow J/\Psi + X$$
$$\hookrightarrow \mu^+\mu^-$$

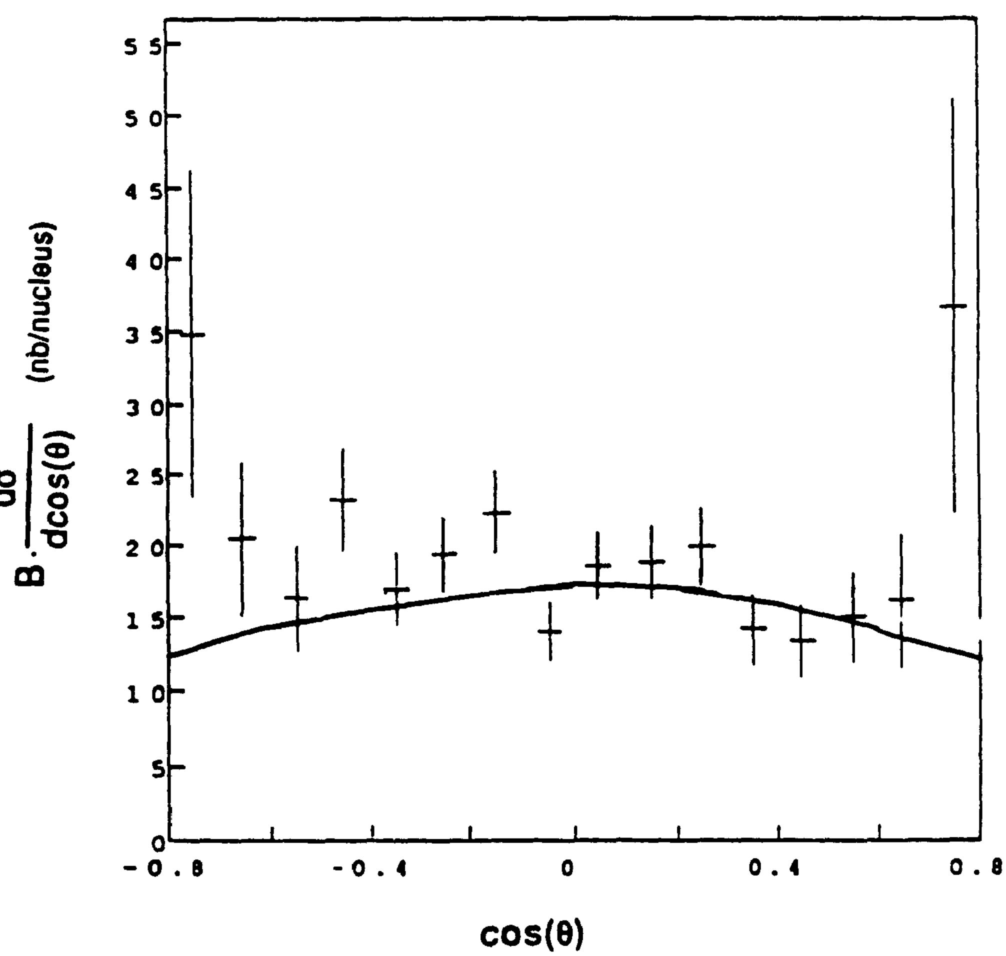

by experiment NA3 on hydrogen target, if the errors from both experiments are added in quadrature.

Table 5.11: *Parameters from the fit of the cosθ distributions*

	α	χ^2/D.O.F.
π^+	-0.24 ± 0.33	23/14
π^-	0.49 ± 0.35	19/14
p	-0.42 ± 0.35	21/14

The ϕ distributions are shown in figure 5.9-a to 5.9-c. The distributions were fitted to a constant, and the χ^2 per degree of freedom from the fits are 17/11, 15/11 and 22/11 respectively for π^+, π^- and p beams.

Figure 5.9-a: *ϕ distributions*

The ϕ distributions, corrected for acceptance, are shown for $\pi^{\pm}$ and p beams. The horizontal line is a fit to a constant function of ϕ.

$$\pi^{+} + N \rightarrow J/\Psi + X$$
$$J/\Psi \rightarrow \mu^{+}\mu^{-}$$

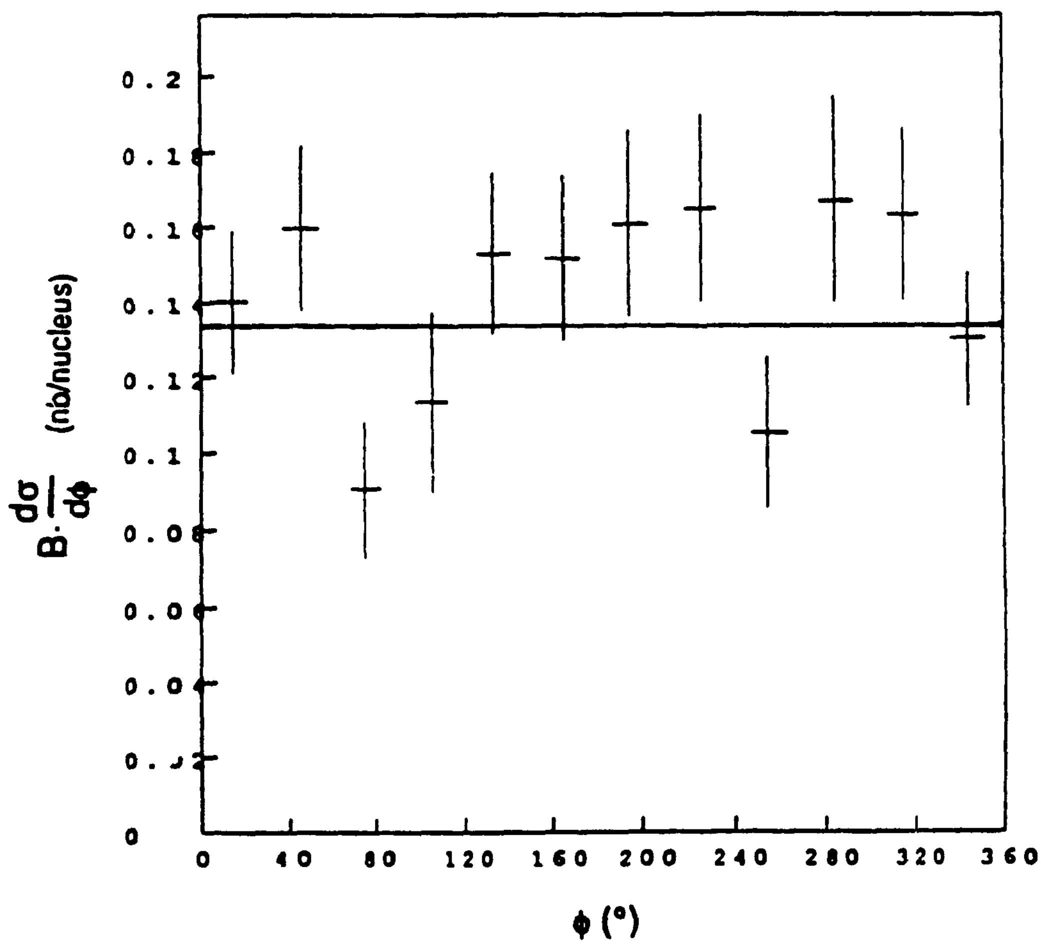

Figure 5.9-b: *ϕ distributions (continued)*

$$\pi^- + N \rightarrow J/\Psi + X$$
$$J/\Psi \hookrightarrow \mu^+\mu^-$$

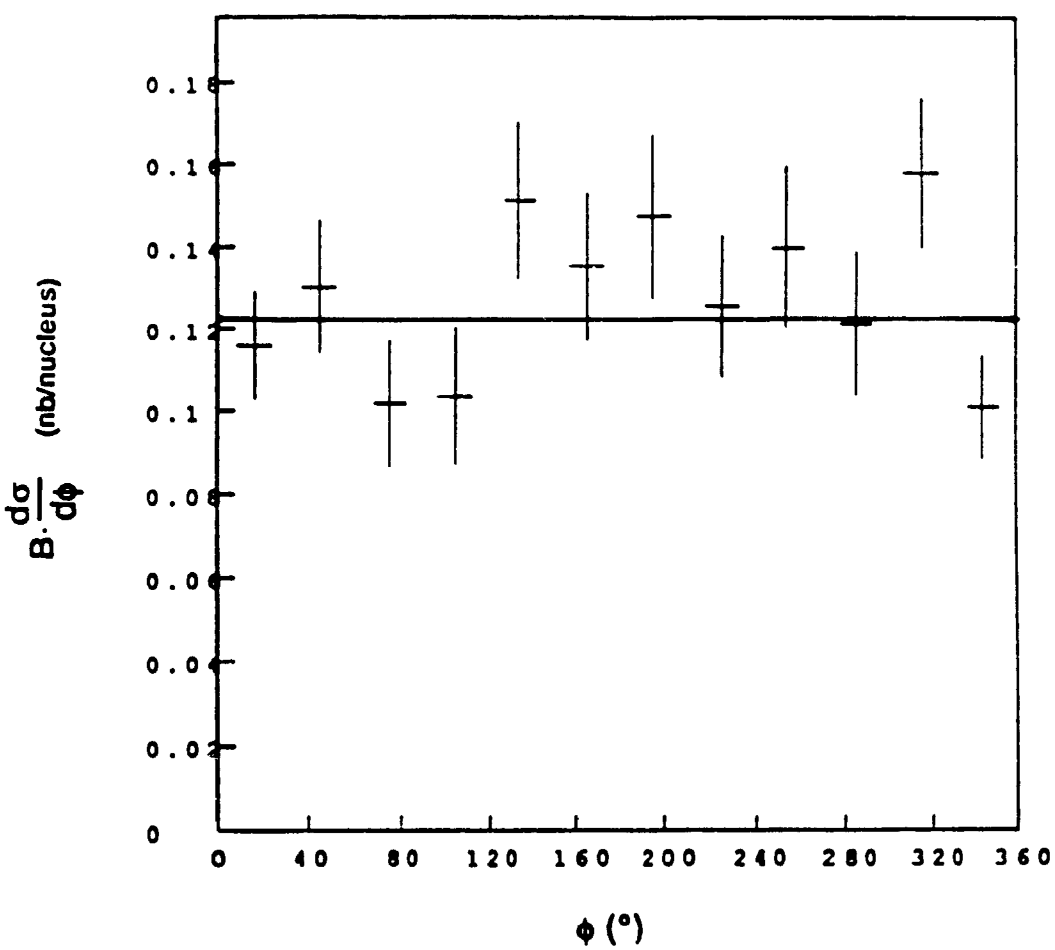

Figure 5.9-c: *φ distributions (continued)*

$$p + N \rightarrow J/\Psi + X$$
$$\quad\quad\quad\quad \hookrightarrow \mu^+\mu^-$$

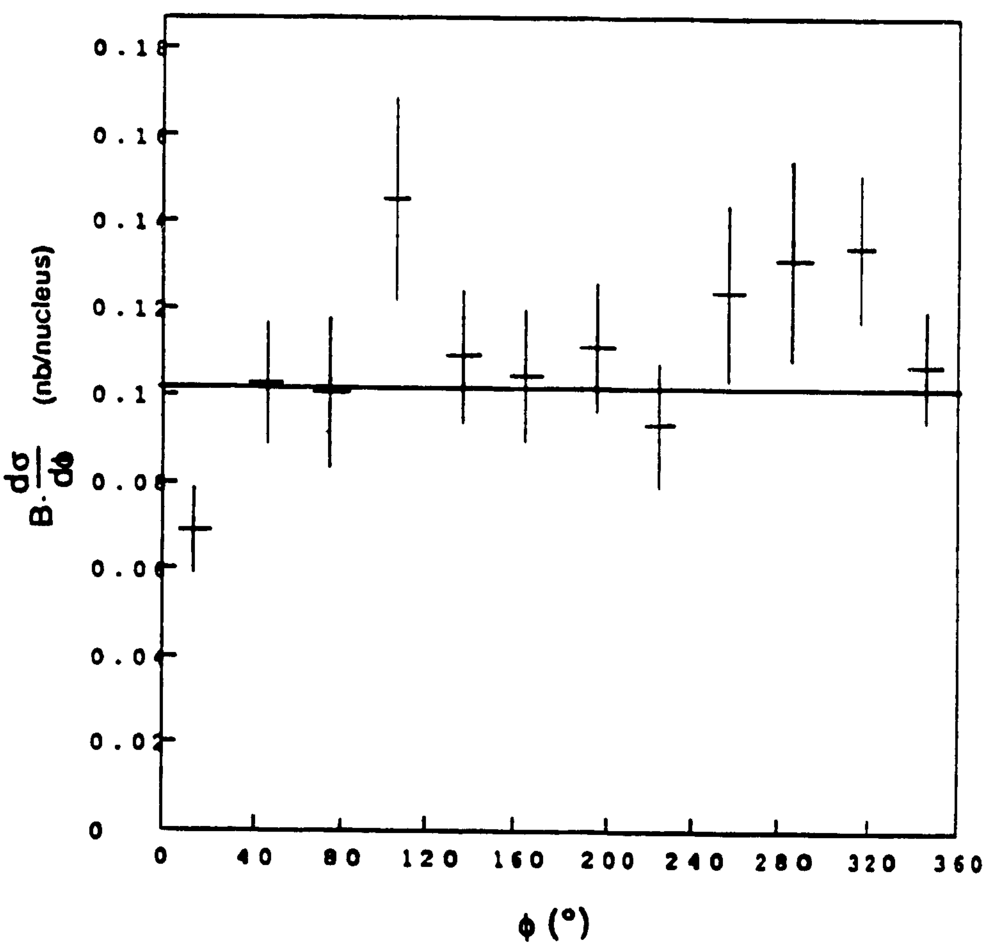

5.7 Conclusion

Performing the analysis of a high energy experiment is a multiple step process, and it is often necessary to verify the consistency of some intermediate results, for which the physics is already known to some extent. Though the main purpose of the E705 experiment is to understand the production processes for the χ states of the charmonium, the study of the J/ψ and Ψ' states was a useful tool to acquire an adequate knowledge of many factors involved in this experiment. The study of the J/Ψ and Ψ' states can also be used to perform a global study of the charmonium family below the open charm mass threshold[1].

The results on J/Ψ absolute cross section, as can be seen in figure 5.4, are, within the errors, consistent with the values measured by other experiments. In particular, the E705 measurement for proton induced J/Ψ cross section confirms the trend of the cross section to increase rapidly with the energy, the small cross section at low energy being generally explained by the fact that the quark annihilation mechanism, allowed in the case of J/Ψ produced by pions, is suppressed in the proton nucleon interactions due to the absence of valence anti-quarks in the proton. At higher energies, the rapid increase of the proton cross section, relative to the pions or anti-proton cross section, is an indication that gluons, and possibly sea quarks, play a more important role in the J/Ψ production.

The Ψ' cross section shown in figure 5.5, is also in agreement with the previous measurements. The difference between the π^- induced Ψ' cross section and the E537,

---

[1] Threshold above which the charmonium state can decay into a pair $D\bar{D}$ (D is a charmed meson made of charm quark and a lighter quark).

WA11 and CIP measurements (1.5 to 2 sigma) is too small to be significant, and is attributed to a statistical fluctuation (only 57 $\pi^- + N \rightarrow \Psi' + X$ events were recorded).

The kinematic distributions for the J/Ψ cross section were evaluated for $\pi^\pm$ and p beams, as can be seen on figures 5.6 to 5.9. The X_f distributions for all beams are narrower than the ones from previous measurements. This can be interpreted as an energy effect, which can also be seen by comparing the distributions for the NA3 distributions for π^- at 150 and 280 GeV/c (figure 5.6-b). However, the distributions from the CS experiment for 400 GeV/c protons does not show this effect when compared with our data (figure 5.6-c).

The Pt distributions, shown in figure 5.7, are wider than the distributions measured by the experiment NA3. However, the NA3 measurement for 280 GeV/c π^- is very similar to our distribution measured at 300 GeV/c. The difference between the E705 π^+ and p distributions and the distributions obtained by NA3 at 200 GeV/c is then interpreted as an increase of the average J/Ψ transverse momentum with the beam energy.

The cos θ distributions of the J/Ψ cross section are shown on figure 5.8-a to 5.8-c. A fit of the distribution from π^- beam to a function in the form $1 + \alpha \cos^2\theta$ gives a value of $\alpha = 0.49 \pm 0.35$, which is 1.9 sigma away from the NA3 measurement $\alpha = -0.20 \pm 0.6 \pm 0.1$ for 280 GeV/c π^- beam on hydrogen target. The ϕ distributions, shown in figure 5.9-a to 5.9-c, are consistent with flat distributions.

The analysis of the entire E705 J/Ψ and Ψ' data (only 10% of the data was analyzed in the present work), in addition to provide a good statistical sample to study χ hadronic production, could improve the results mentioned above. Though most of the errors on J/Ψ cross sections are due to systematics, the analysis of a larger data sample should allow a good measurement of the Ψ' to J/Ψ cross section ratios, for which most of the systematic errors can be neglected. This analysis should also lead to a better measurement of the $\cos(\theta)$ dependance for the J/Ψ production.

References

(1) Chadwick,J., Nature 129, 312 (1932)

(2) Chadwick,J., Proc.Roy.Soc. A136, 692 (1932)

(3) Gell-Mann,M., Phys.Lett. 8, 214 (1964)

(4) Zweig.G., CERN Report 8182/Th.401, CERN, Geneva, Switzerland (1964)

(5) J.J.Aubert et al. (MIT-Brookhaven), Phys.Rev.Lett. 33, 1404 (1974)

(6) J.-E.Augustin et al. (SLAC-LBL), Phys.Rev.Lett. 33, 1406 (1974)

(7) S.L.Glashow, J.Iliopoulos and L.Maiani, Phys. Rev. D2, 1285 (1970)

(8) W.Braunschweig et al. Phys.Lett. B57, 407 (1975)

(9) G.J. Feldman et al., Phys.Rev.Lett. 35, 821 (1975)

(10) E.D.Bloom Symposium on lepton and photon interactions FNAL 1979

(11) M.J. Corden et al., Phys.Lett. B96, 411 (1980)

(12) K.J. Anderson et al., Phys.Rev.Lett 42, 944 (1979)

(13) S.Katsanevas et al., Phys.Rev.Lett. 60,2121 (1988)

(14) J.Badier et al., Particles and Field 20, 101 (1983)

(15) A.A.Zholents et al., Phys.Lett. B96, 214 (1980)

(16) C.N.Yang, Phys.Rev. 77, 242 (1950)

(17) B.L.Ioffe, Phys.Rev.Lett. 39, 1589 (1977)

(18) H.Areti et al., Nucl.Inst.and.Meth. 212, 135 (1983)

(19) J.G.Branson et al., Phys.Rev.Lett. 38, 1331 (1977)

(20) M.A.Abolins et al., Phys.Lett. 82B, 145 (1979)

(21) E.J.Siskind et al., Phys.Rev D21, 628 (1980)

(22) L.Lyons, Prog. Part. Nucl. Phys. 7, 169 (1981)

(23) H.D.Snyder et al., Phys.Rev.,Lett. 36, 1415 (1976)

(24) A.G.Clark et al., Nucl.Phys. B142, 29 (1978)

(25) T.Nash et al., Fermilab-Conf-88/97 (1988)
and T.Nash et al., Fermilab-Conf-89/58 (1989)

(26) S.Conetti at al., IEEE Trans.Nuc.Sc., NS32, 1318 and 1326 (1985)